

Syracuse University

SURFACE

Physics - Dissertations

College of Arts and Sciences

8-2012

Microstrip Superconducting Quantum Interference Devices for Quantum Information Science

Michael Paul DeFeo
Syracuse University

Follow this and additional works at: https://surface.syr.edu/phy_etd



Part of the [Physics Commons](#)

Recommended Citation

DeFeo, Michael Paul, "Microstrip Superconducting Quantum Interference Devices for Quantum Information Science" (2012). *Physics - Dissertations*. 127.
https://surface.syr.edu/phy_etd/127

This Dissertation is brought to you for free and open access by the College of Arts and Sciences at SURFACE. It has been accepted for inclusion in Physics - Dissertations by an authorized administrator of SURFACE. For more information, please contact surface@syr.edu.

Abstract

Quantum-limited amplification in the microwave frequency range is of both practical and fundamental importance. The weak signals corresponding to single microwave photons require substantial amplification to resolve. When probing quantum excitations of the electromagnetic field, the substantial noise produced by standard amplifiers dominates the signal, therefore, several averages must be accumulated to achieve even a modest signal-to-noise ratio. Even worse, the back-action on the system due to amplifier noise can hasten the decay of the quantum state. In recent years, low-noise microwave-frequency amplification has been advancing rapidly and one field that would benefit greatly from this is circuit quantum electrodynamics (cQED). The development of circuit quantum electrodynamics—which implements techniques of quantum optics at microwave frequencies—has led to revolutionary progress in the field of quantum information science. cQED employs quantum bits (qubits) and superconducting microwave resonators in place of the atoms and cavities used in quantum optics permitting preparation and control of low energy photon states in macroscopic superconducting circuits at millikelvin temperatures. We have developed a microstrip superconducting quantum interference device (SQUID) amplifier (MSA) to provide the first stage of amplification for these systems. Employing sub-micron Josephson tunnel junctions for enhanced gain, these MSAs operate at microwave frequencies and are optimized to perform with near quantum-limited noise characteristics.

Our MSA is utilized as the first stage of amplification to probe the dynamics of a SQUID oscillator. The SQUID oscillator is a flux-tunable microwave resonator formed by a capacitively shunted dc SQUID. Josephson plasma oscillations are induced by pulsed microwave excitations at the resonant frequency of the oscillator. Once pulsed, decaying plasma oscillations are observed in the time domain. By measuring with pulse amplitudes approaching the critical current of the SQUID, it is possible to probe the free evolution of a highly nonlinear oscillator.

Microstrip Superconducting Quantum Interference Devices for Quantum Information Science

BY

MICHAEL P. DE FEO

B.S. Syracuse University – Syracuse, New York, 2005

DISSERTATION

Submitted in partial fulfillment of the requirements for the
degree of Doctor of Philosophy in Physics
in the Graduate School of Syracuse University

August, 2012

Copyright 2012 Michael P. DeFeo

All Rights Reserved

Acknowledgments

First, I would like to thank my advisor, Britton Plourde. I am fortunate to have worked with an advisor so knowledgeable and dedicated to the success of his graduate students. I am grateful for the late nights and weekends he spent in the lab assisting me with measurements and for the patient answers he provided to my many questions.

I would also like to thank the post-doctoral researchers and graduate students that I have had the privilege of working alongside and learning from when I first joined the group: Tom Heitmann, Kang Yu, and Chunhua Song. I would especially like to acknowledge Pradeep Bhupathi, who worked closely with me on this project, specifically for the work he did measuring the SQUID oscillator. The SQUID oscillator measurements would not have been possible without the contributions of Matthew Ware who took on the task of assembling and programming the custom electronics used for the measurement. I am also grateful to Joel Strand and Francisco Rouxinol for providing insightful answers to my questions about SQUIDs and Josephson junctions, and a quiet space to write my thesis. Additionally, I would like to thank Maxim Marchevsky for the influence he had on me as a young scientist. I am grateful to Lou Buda, Phil Arnold, Charlie Brown and Lester Schmutzler for their assistance and advice on physics-related and non-physics-related projects.

This project would not have been possible without assistance from the staff at the Cornell Nanoscale Science and Technology Facility. I thank those who often went beyond the call of duty especially Garry Bordonaro, Noah Clay, Rob Illic and Daron Westly. To those who were not involved with my project but provided support through other means—David Quint, Michele Fontanini, Luca Giomi, Eric West and Duncan Brown—thank you for commiserating with me.

Finally, I would like to thank my family for providing me the opportunity to pursue my career. I am especially grateful to my grandfather, Walter, who fostered my interest in mathematics and science from a young age. I am eternally grateful to my wife, Carolyn, for the enduring support she provided during the past several years.

Contents

1	Introduction	1
1.1	Introduction	1
1.2	Circuit quantum electrodynamics	2
1.3	Cavity quantum electrodynamics	3
1.4	Superconductivity	6
1.4.1	Superconducting qubits	7
1.4.2	Qubit readout	10
1.5	Outline	13
2	The Josephson junction and dc SQUID	14
2.1	The Josephson tunnel junction	14
2.1.1	The Josephson junction as a circuit element	17
2.1.2	Circuit model – RCSJ	18
2.1.3	Analogous systems	20
2.1.4	Josephson junctions in magnetic fields	23
2.2	The dc superconducting quantum interference device	27
2.2.1	Bias dependence and the SQUID potential	27
2.2.2	Flux-to-voltage transduction	31
2.3	dc SQUIDs as amplifiers	32
2.4	Practical SQUID amplifiers	33
2.4.1	SQUID noise	36

2.5	SQUIDs at the quantum limit	40
2.6	Applications of the SQUID	41
2.7	Limitations	43
3	Low-noise amplification	44
3.1	The high electron mobility transistor amplifier	44
3.2	Parametric amplification	46
3.2.1	Josephson parametric amplifier	46
3.2.2	Josephson parametric converter	47
3.2.3	Kinetic inductance parametric amplifier	48
3.2.4	The Josephson bifurcation amplifier	49
3.3	The superconducting low-inductance undulatory galvanometer	49
4	The microstrip SQUID amplifier	52
4.1	Stray capacitance — Bug or feature?	52
4.2	Microwave resonant circuits	55
4.2.1	Transmission lines and resonators	56
4.3	The microstrip SQUID amplifier — early measurements	59
4.3.1	Gain	61
4.3.2	Noise properties	63
4.3.3	Other configurations	64
5	Device Fabrication	68
5.1	Substrate preparation - MOS processing	68
5.2	Photolithography	70
5.3	Metal and dielectric deposition	71
5.3.1	Resistive shunts	71
5.3.2	SQUID washer and counterelectrode	72
5.3.3	Dielectric deposition	73
5.4	Electron beam lithography	74

5.4.1	Shadow evaporation	75
6	Measurements at 1.55 GHz	80
6.1	Introduction	80
6.2	MSAs with small area junctions	80
6.3	Room temperature characterization	81
6.4	Cryogenic measurement	83
6.4.1	Cryostat	83
6.4.2	Device packaging	84
6.4.3	Low-frequency measurement at cryogenic temperature	84
6.4.4	Device parameters	90
6.4.5	Gain	92
7	Measurement of MSAs near 4 GHz	96
7.1	Second generation devices	96
7.1.1	Microwave board	97
7.1.2	Input circuit	98
7.1.3	Input coil and ground plane	99
7.1.4	Measurement circuitry	100
7.2	Gain measurement	101
8	Noise	104
8.1	Introduction	104
8.2	Noise temperature	104
8.3	Noise factor, Y-factor and noise temperature	106
8.3.1	Noise factor	106
8.3.2	Y-factor	108
8.3.3	Noise temperature measurements of low-noise amplifiers	111
8.4	Noise temperature measurement techniques	114
8.4.1	Signal-to-noise ratio comparison	114

8.4.2	Modified Y-factor measurement	117
8.5	Results	120
8.5.1	Frequency dependence	121
8.5.2	Temperature dependence	121
8.5.3	Hot electrons	123
9	Application of near quantum-limited amplifiers in GHz range	127
9.1	The SQUID oscillator	127
9.2	Measurement of SQUID oscillators	131
9.2.1	Frequency domain	131
9.2.2	Transient dynamics	132
10	Future work	139
10.1	Introduction	139
10.2	Three-dimensional cooling fins	139
10.3	Higher frequencies	142
A	Fabrication recipes	145
A.1	Photolithography	145
A.1.1	Mask preparation	145
A.1.2	Wafer preparation	145
A.1.3	Exposure	146
A.2	Metalization — Shunts	147
A.3	Groundplane deposition	147
A.4	Dielectric deposition — GSI-PECVD	148
A.5	Dielectric deposition — IPE-PECVD	149
A.6	Etching	149
A.7	Input coil	150
A.8	Electron beam lithography	150
A.9	Junction deposition	151

List of Figures

2.1	The Josephson junction	15
2.2	Schematic of junction I-V characteristic	17
2.3	RCSJ schematic	19
2.4	Damped driven pendulum model	21
2.5	Tilted washboard model	23
2.6	Schematic of a junction in a magnetic field	24
2.7	Critical current of a junction in a magnetic field	26
2.8	SQUID schematic	27
2.9	SQUID magnetic field dependence	29
2.10	SQUID potential	31
2.11	SQUID V - Φ characteristic	32
2.12	SQUID amplification schematic	33
2.13	dc SQUID amplifier circuit	34
2.14	Noise temperature	37
3.1	SLUG schematic	50
4.1	SQUID with coil inside washer	53
4.2	Alternative SQUID amp. design	54
4.3	Transmission line schematic	55
4.4	MSA gain in different coupling regimes	59
4.5	Older MSA design	60

4.6	MSA schematic with transmission line input coil	61
4.7	Tunable MSA with varactor diode	66
5.1	Shadow evaporation	76
5.2	MSA chip — 1.55 GHz	78
6.1	MSA circuit board	85
6.2	MSA measurement circuit schematic	85
6.3	I-V and V- Φ measurement schematic	88
6.4	I-V and V- Φ curves	90
6.5	First generation devices	91
6.6	MSA Gain measurement schematic	93
6.7	MSA Gain measurement and schematic	94
7.1	Second generation device	97
7.2	Microwave board	98
7.3	Coplanar waveguide to microstrip transition	99
7.4	Second generation gain schematic	101
7.5	Maximum gain — second generation device	102
7.6	Power dependence of gain	103
8.1	Noise temperature	106
8.2	Y-factor schematic plot	109
8.3	Y-factor data, linear vs log-log	110
8.4	Amplifier cascade	112
8.5	Signal-to-noise ratio measurement with MSA	116
8.6	T_N as a function of frequency	116
8.7	Circuit schematic for T_N measurement	119
8.8	Electronics for T_N measurement	120
8.9	Noise temperature measurement of HEMT amplifier	122

8.10	T_N measurement with MSA in amplifier chain	122
8.11	T_N as a function of frequency	123
8.12	T_N as a function of bath temperature	124
9.1	Scanning electron micrographs of SQUID oscillator	128
9.2	Ringdown measurement schematic	131
9.3	QND measurement schematic	132
9.4	The SQUID oscillator bias flux modulation	133
9.5	Schematic of SQUID oscillator ringdown measurement	134
9.6	Raw burst signal and ringdown oscillation time trace	135
9.7	Ringdown oscillation density plot	137
9.8	Flux modulation of SQUID oscillator with MSA post-amplifier	138
10.1	3D cooling fin test structure	141
10.2	Electron temperature vs. power	142
10.3	MSA configured to accommodate 3D cooling fins	143
10.4	MSA at 9 GHz	143

List of Tables

4.1 Parameters for five MSAs of different input coil lengths 62

Chapter 1

Introduction

1.1 Introduction

The ability to probe low energy excitations of the electromagnetic field is of great importance to our fundamental understanding of nature. Reliable detection of low energy microwave frequency photons has had a broad impact on several fields of physics, ranging from astronomy [1] to quantum mechanics [2]. One great difficulty in detecting single microwave photons is the small signals associated with these photons require amplification to make them resolvable. In addition to this, the signals from these photons are often much smaller than the noise added to the signal during amplification. Therefore, even with substantial gain averaging is often necessary. All amplification processes add some amount of noise to the amplified signal. In most cases the origin of this noise is classical in nature and arises from dissipative elements of the amplifier circuit such as transistors and resistors. However, in superconducting circuits where current can flow without producing dissipation, this source of noise can be greatly reduced. Using superconducting circuits, amplifiers have been demonstrated to operate where the amplifier noise is primarily due to quantum fluctuations, however, producing an amplifier with this characteristic is an extraordinarily difficult task. Near quantum limited amplification often comes at the expense of other prop-

erties of the amplifier such as gain, bandwidth, dynamic range, or phase-sensitivity. In the past several years, there has been increasing interest in low-noise amplification in the microwave frequency range. One field that would benefit greatly from near quantum limited amplification is circuit quantum electrodynamics, which studies non-classical photons at microwave frequency.

1.2 Circuit quantum electrodynamics

Recently, techniques developed in quantum optics and cavity quantum electrodynamics (CQED) have been implemented at microwave wavelengths using superconducting integrated circuits at millikelvin temperatures [3]. This implementation of on-chip quantum electrodynamics, known as circuit quantum electrodynamics (cQED), employs the nonlinearity of the Josephson junction—a circuit element with two superconducting electrodes separated by a barrier—to reproduce the natural nonlinearity of atoms in CQED. The artificial atom produced by the junction circuit can exchange photons with an electromagnetic resonant cavity as opposed to the large-volume physical cavities typical of CQED. There are several manifestations of superconducting circuits involving one or more Josephson junctions that can behave as two-level systems with transition energies in the microwave frequency range. These superconducting circuits are known as quantum bits, or qubits. Superconducting qubits coupled to resonant cavities are a promising architecture for producing a scalable quantum computer. One of the key advantages of cQED is that the circuits are macroscopic and the coupling strength between the nonlinear element and the linear cavity modes are much stronger than the coupling strength between atoms and photons provided by nature. In addition to this, cQED systems are completely engineered so characteristic energies and coupling strengths can be modified during device fabrication. In section 1.4.1, “Superconducting qubits”, a few different types of these devices are discussed briefly.

1.3 Cavity quantum electrodynamics

Nonclassical photon states are of great interest due to their practical applications and their ability to probe fundamental physics. The study of non-classical states of light at optical frequencies is known as quantum optics. In quantum optics photons can be prepared in specific quantum states, interacted with other photons, and tracked as their state evolves with time. Quantum optics has provided a window through which the quantum nature of light can be observed. In addition to experimentally verifying several predictions of quantum mechanics, quantum optics has also provided broad and fundamental results including demonstrating entanglement [4], quantum teleportation [5], and quantum logic gates [6].

The field of CQED probes the interaction of light with matter by confining a single atom to a cavity and exciting it with nonclassical light that is resonant with the transition energy of the atom. Using this technique, individual atomic transitions have been observed as well as coherent absorption and emission of a single photon. In many cases, the transition energy between the ground and excited state is unique. Therefore, the atom can be approximated as a two-level system with an excited state $|e\rangle$ and ground state $|g\rangle$ that are connected by an electric dipole transition at frequency ω_{eg} [7]. This system is analogous to a spin 1/2 particle in a magnetic field oriented along the positive Z direction. Taking $|e\rangle \rightarrow |0\rangle$, $|g\rangle \rightarrow |1\rangle$ the following Hamiltonian can be written

$$\hat{\mathbf{H}}_a = \frac{\hbar\omega_{eg}}{2}\hat{\sigma}_z, \quad (1.1)$$

and atomic raising and lowering operators can be defined

$$\hat{\sigma}_{\pm} = \frac{1}{2}(\hat{\sigma}_x \pm i\hat{\sigma}_y) \quad (1.2)$$

where $\hbar = 1.05 \times 10^{-34}$ Js, $i = \sqrt{-1}$, $\hat{\sigma}_{x,y,z}$ are the Pauli matrices and $\hat{\sigma}_+ = |e\rangle\langle g|$, $\hat{\sigma}_- = |g\rangle\langle e|$ and $\hat{\sigma}_z = |e\rangle\langle e| - |g\rangle\langle g|$.

An atom in a cavity can be excited from its ground state by coherent absorption of a photon of frequency ω_{eg} and can return to its ground state by emitting a photon

of the same energy into a single mode of the cavity. The fields of the available modes in the cavity are quantum harmonic oscillators described by the standard quantum harmonic oscillator Hamiltonian [8]

$$\hat{\mathbf{H}}_c = \hbar\omega_c \left(\hat{\mathbf{a}}^\dagger \hat{\mathbf{a}} + \frac{1}{2} \right) \quad (1.3)$$

where $\hat{\mathbf{a}}^\dagger$ and $\hat{\mathbf{a}}$ create or annihilate a photon of frequency ω_c , respectively. Near resonance or for small detunings, the atom can exchange a photon with the cavity and this exchange is given by the following interaction Hamiltonian in the rotating wave approximation where rapidly rotating terms given by $\omega_c + \omega_{eg}$ are neglected

$$\hat{\mathbf{H}}_{ac} = \hbar g (\hat{\mathbf{a}} \hat{\sigma}_+ + \hat{\mathbf{a}}^\dagger \hat{\sigma}_-) \quad (1.4)$$

where g is related to the electric dipole transition between the ground and excited state. This Hamiltonian describes the process of the atom becoming excited by absorption of a photon from the cavity or an atom emitting a photon into the cavity and relaxing to its ground state. Combining these terms $\hat{\mathbf{H}}_{J-C} = \hat{\mathbf{H}}_a + \hat{\mathbf{H}}_c + \hat{\mathbf{H}}_{ac}$ leads to the Jaynes-Cummings Hamiltonian [9]:

$$\hat{\mathbf{H}}_{J-C} = \frac{\hbar\omega_{eg}}{2} \hat{\sigma}_z + \hbar\omega_c \left(\hat{\mathbf{a}}^\dagger \hat{\mathbf{a}} + \frac{1}{2} \right) + \hbar g (\hat{\mathbf{a}} \hat{\sigma}_+ + \hat{\mathbf{a}}^\dagger \hat{\sigma}_-). \quad (1.5)$$

With the atom in its ground state and no initial excitation in the cavity, an atom slightly detuned from the cavity can exchange a virtual photon back and forth with the cavity. This process of coherent exchange is known as a vacuum Rabi oscillation, and the frequency at which the exchange takes place is given by the vacuum Rabi frequency $\Omega = \sqrt{(\omega_{eg} - \omega_c)^2 + (2g)^2}$. Even in the limit where the atom is far detuned from the cavity frequency ($|\omega_{eg} - \omega_c| \gg 0$), there is still a state-dependent dispersive interaction between the atom and the cavity such that measurements of the cavity transmission can probe the state of the atom or vice-versa. An arbitrary superposition of the two basis states of the system can be produced if the atom-cavity coupling is turned on for some period of time not equal to $1/\Omega$. A two-level system coupled to a

cavity is the basis for many realizations of quantum bits (qubits), which rely on the superposition of quantum states [10].

Although quantum optics and CQED have laid the foundation for our understanding of qubits and quantum information science, there are very significant technical hurdles that would be difficult to surmount in order to implement quantum computation in these architectures including scalability, overall complexity, and characteristic coupling strengths and energy scales. Engineered systems pose many advantages over CQED as an architecture to study quantum information. Superconducting qubits, for instance, have a much smaller mode volume than a resonant cavity therefore they are more scalable. Also, the characteristic coupling strength between the qubit and cavity can be modified when the circuit is fabricated. Presently, there are several other architectures under investigation as potential artificial atoms, including: trapped ions [11], gasses of neutral atoms [12], nitrogen vacancy centers in diamond [13], charges in semiconductors [14], nuclear spins [15], superconducting systems [16] and hybrid systems [17]. In the past several years each of these systems contributed to our understanding of quantum information science and fundamental physics, however they all have their own unique disadvantages. We are investigating superconducting qubits, where the quantum mechanical degree of freedom is the macroscopic ground state of the superconducting wavefunction. One of the great advantages of using superconducting qubits is their inherently small dissipation. Also, superconducting qubits have a greatly reduced mode volume compared to three dimensional atomic systems, which makes it more practical to reach the strong coupling regime where the interaction between two systems is faster than the energy dissipation in either of the two systems.

1.4 Superconductivity

The condensation of gaseous He to a liquid by Heike Kamerlingh Onnes in 1908 was a hallmark event that brought to light new physical regimes that were previously inaccessible [18]. It was only about three years after this that Kamerlingh Onnes first observed that when mercury was cooled below 4.1 K it exhibited zero electrical resistance [19], one of the characteristics of superconductivity. In the following years, many other elements were observed to exhibit the same behavior, but it was not until 1933 that Walther Meissner and Robert Ochsenfeld observed that superconducting materials completely screen out small amounts of magnetic flux from their interior when in the superconducting state [20]. Although a perfect conductor will exhibit this behavior, Meissner also observed that a superconducting material in the presence of a magnetic field will expel the field from its interior when cooled through its superconducting transition temperature, which is not a property a material with perfect conductivity would exhibit. This discovery was the first experimental evidence that the superconducting state involved more than just perfect conductivity [20].

The first widely accepted phenomenological theory to describe the perfect conductivity and perfect diamagnetism of the superconducting state was published by F. and H. London in 1935 [21]. Their theory also introduced a characteristic length scale λ over which magnetic fields exponentially decay upon penetrating into the surface of a superconducting material. The next big breakthrough in understanding the superconducting state was the theory of Ginzburg and Landau published in 1950 [22]. Two of the great successes of this theory were in describing the phase transition from the normal resistive state of a metal to the superconducting state, and the coherence length ξ which described the scale over which the superconducting order parameter may vary.

In 1957, the first microscopic theory of superconductivity was proposed by Bardeen, Cooper and Schrieffer (BCS) [23]. One key concept of the theory is that in a superconducting material a weak attractive interaction exists between electrons that is

mediated through electron-phonon interactions. When cooled into a superconducting state, the energy of the system is reduced by Δ below the Fermi energy by pairing of electrons, where Δ is the pair binding energy and a material parameter known as the superconducting gap. For a pair of electrons this binding energy, 2Δ , is far less than the thermal energy $k_B T$ at room temperature. However, when the temperature of a superconducting material is reduced below the critical temperature of the material, T_c , a thermodynamic phase transition takes place and it is energetically favorable for electrons to form Cooper pairs. For a weak-coupling superconductor this transition occurs at $T_c \approx 2\Delta/(3.5k_B)$. The Cooper pairs form a ground state that is described by a macroscopic quantum wavefunction with a well-defined phase that is constant throughout the material in the absence of any currents. The current in superconductors, the supercurrent, is carried by Cooper pairs of charge $2e$ where e is the charge of the electron. The supercurrent flows free of resistance at dc in the presence of a current bias.

In 1962 Brian D. Josephson was the first to theorize that it is possible for pairs of electrons, Cooper pairs [23], to tunnel from one superconductor to another closely spaced superconductor without dissipation when driven with a current bias [24]. A year later, this phenomenon, known as the Josephson effect, was first observed by Anderson and Rowell [25]. Two superconductors separated by a thin non-superconducting barrier form a structure known as the Josephson tunnel junction and these circuits have since played an integral role in low temperature physics, as well as several other fields.

1.4.1 Superconducting qubits

One of the simplest quantum integrated circuits is the LC oscillator, where all metallic traces and circuit elements are fabricated from superconducting materials. This quantum LC oscillator can either consist of lumped element inductances (L) and capacitances (C), or the inductances and capacitances can be distributed as they are in

a transmission line resonator. The Hamiltonian for this circuit can be written in terms of the flux in the inductor Φ , which plays the role of the position coordinate, and the charge on the capacitor Q , which plays the role of the conjugate momentum. These operators obey the commutation relation $[\Phi, Q] = i\hbar$. When cooled to sufficiently low temperatures, the Hamiltonian of the circuit can be written as $H = \Phi^2/2L + Q^2/2C$ or in a more familiar form $H = \hbar\omega_0(n + 1/2)$ where n is the number operator and $\omega_0 = 1/\sqrt{LC}$ [26]. The quantum LC oscillator is not a good choice for an artificial atom as the energy levels are equally spaced. The harmonicity of energy levels makes it difficult to address individual transitions. However, this harmonicity can be lifted by incorporating a nonlinear element, the Josephson junction, into the circuit. Nonetheless, the quantum LC oscillator has some utility in cQED, either lumped-element or distributed element LC circuits serve as the cavity with which qubits can exchange photons.

For the purpose of discussing superconducting qubits, the Josephson junction can be described as a nonlinear inductance in parallel with the geometric capacitance of the junction forming an anharmonic oscillator. The oscillator can be characterized by two energy scales, the Josephson energy E_J , which is related to the energy stored in the inductance of the circuit and the Coulomb charging energy E_C , corresponding to one Cooper pair on the circuit capacitance. There are several different types of superconducting qubits, which are characterized by their ratio E_J/E_C .

The Cooper pair box, also known as the charge qubit, was first described theoretically by Büttiker [27] and realized by the research group in Saclay in 1997 [28]. The basic charge qubit consists of a small superconducting island separated from a large superconducting reservoir by two junctions. A voltage applied to a gate electrode that is in close proximity to the island changes the charging energy for Cooper pairs on the island. The number of Cooper pairs on the island is a discrete variable and the basis states of the Cooper pair box are neighboring number states $|n\rangle, |n + 1\rangle$. The number of Cooper pairs on the island of the device can be coherently controlled

by modulating the voltage on the gate electrode [16, 29]. Cooper pair box qubits operate in the regime $E_J \ll E_C$.

The flux qubit [30], in the simplest case, consists of a single junction interrupting a superconducting loop. For the flux qubit the quantum mechanical degree of freedom is the flux through the superconducting loop. The two basis states of the system are flux pointing up $|\uparrow\rangle$ (corresponding to counterclockwise circulating currents) and flux pointing down $|\downarrow\rangle$ (corresponding to clockwise circulating currents). The two states are at the potential minima of a double well potential that is symmetric when the applied magnetic flux in the qubit loop is $\Phi_0/2$. In this symmetric state, the two stationary states of the system become the symmetric and antisymmetric combinations of the basis states $|\uparrow\rangle$ and $|\downarrow\rangle$, separated by an energy difference Δ related to the rate at which the system can tunnel between the $|\uparrow\rangle$ and $|\downarrow\rangle$ flux states [16]. Flux qubits are typically designed such that $E_J \gg E_C$.

The phase qubit consists of a junction in a superconducting loop, biased with an external flux such that the local potential is approximately cubic [31]. The energy level spacing becomes progressively smaller as the quantum number n increases. As the number state increases, the probability that the state will tunnel out of the potential also increases, which will cause a change in the flux state of the qubit. Devices are typically designed such that tunneling probability of the ground state is small compared to the first excited state. Phase qubits are designed to operate with $E_J \gg E_C$.

All of the qubits discussed above are macroscopic circuits, thus they couple to many lossy degrees of freedom that cause decoherence of the quantum state. In addition to this, each type of qubit can be more susceptible to a particular source of noise. For instance, the charge qubit is particularly sensitive to low-frequency noise from charge motion due to defects in the substrate and interfaces. This manifests itself as random shifts in the effective gate bias of the superconducting island. The effects of this noise can be mitigated by operating the qubit at the charge degeneracy

point where the energy level difference becomes insensitive to the gate bias to first order [26, 32].

Recently, a new design related to the charge-based qubit was realized with $E_J > E_C$. The charging energy E_C of the transmission line shunted plasma oscillation qubit (transmon) is reduced by shunting the qubit with a large capacitance relative to the junction capacitance [33]. In this regime, the transmon is much less sensitive to charge noise, however its anharmonicity is also reduced. It was realized that the sensitivity to charge noise reduces exponentially in E_J/E_C while the anharmonicity only decreases algebraically with a slow power law in E_J/E_C . Therefore, by operating the transmon at a much larger E_J/E_C than the Cooper pair box, the sensitivity to charge noise is greatly reduced while only reducing the anharmonicity a modest amount. By reducing the sensitivity to charge noise as well as surface loss, transmon qubits have demonstrated coherence times close to 0.1 ms [34], [35].

1.4.2 Qubit readout

Circuit QED studies the interaction between qubits and linear cavities at microwave frequencies. The qubit can be prepared into its excited state with microwave radiation that is resonant with the transition between the ground and excited state. The qubit can then be brought into resonance with a cavity of fixed resonant frequency and the photon can be swapped from the qubit into the cavity by controlling the qubit-cavity interaction time, producing an $n = 1$ Fock state in the cavity. If the interaction between the qubit and cavity is maintained for an arbitrarily long period of time, the photon is exchanged several times between the qubit and cavity for a high quality qubit and high quality cavity before the photon decays. If the qubit and cavity are coupled for a period of time less than the time it takes to perform a full swap operation, an arbitrary coherent superposition of the photon and qubit state is produced. Using this technique, several highly non-classical states have been prepared, manipulated, and measured, including: Fock states up to $n = 6$ [2] and arbitrary superpositions

of number states [36]. In addition to this quantum gate operations [37] have also been demonstrated in this architecture, which is an important step for implementing quantum algorithms.

One of the important issues in the field of superconducting quantum information science is how to best detect the weak signal from a single microwave photon. In the cQED scheme, the resonant cavity is capacitively coupled to a microwave line. The small voltage corresponding to the microwave photon is carried through a coaxial cable to a cryogenic microwave amplifier, and it is again amplified at room temperature. The most common form of cryogenic microwave amplification relies on transistors which use a 2D electron gas to maintain conductivity at cryogenic temperatures. These high electron mobility transistor amplifiers (HEMTs) are thermally sunked at ~ 4 K in the measurement cryostat and the noise temperature of these amplifiers are typically 3-4 K. For technical reasons it is not possible to decrease the noise produced by the amplifier by cooling it further. The noise properties of these amplifiers are exceptional when compared with other transistor based amplifiers. However, when amplifying the signal from a single 10 GHz photon, the amplifier will add an additional 8 photons of noise on to the measured signal. Therefore, the result of several measurements must be averaged to resolve the signal, making a single-shot measurement impossible. One consequence of this is a substantial increase in measurement time. In addition to this practical issue, measurement of a quantum system with a noisy amplifier induces back-action on the qubit system causing a loss of coherence.

An example of the utility of a near quantum limited amplifier was recently demonstrated by R. Vijay *et al.* [38]. A quantum limited amplifier was used to read out the state of a cavity by monitoring the phase of a probe signal transmitted through the cavity. The coupling between the qubit and the cavity cause a qubit-state dependent phase shift of the transmitted signal. A very small amplitude cavity probe tone (< 1 photon) was used to perform a continuous weak measurement of the state of the system. The cavity probe photons were then sent to a quantum limited amplifier

that enabled real time monitoring of the state of the cavity as the system underwent driven Rabi oscillations. Since the state of the cavity could be monitored in real time, when the Rabi oscillations were observed to decay, a feedback loop was employed to modify the drive allowing Rabi oscillations to persist indefinitely. Quantum feedback cannot be implemented with a standard cryogenic amplifier due to the long integration time necessary to achieve a signal to noise ratio greater than unity. If one tried to reproduce this measurement with a HEMT amplifier that contributes roughly 20 times more noise to the measured signal, the signal would have to be averaged 400 times to achieve the same signal-to-noise ratio as the quantum limited amplifier without any averaging. In addition to this very practical reduction in measurement time, the more fundamental implications of this result are staggering. Using this technique allows the decoherence of a quantum state to be actively suppressed and is a large step toward a scalable architecture for quantum computing.

As a result of the fervent interest in quantum information science and superconducting qubits in the past few years, low-noise cryogenic amplification has become a subject of great interest. There are several realizations of low-noise cryogenic amplifiers currently under investigation. In the ideal case, the amplifier would contribute no noise to the measurement, however, according to quantum mechanics this is not possible. The best that any linear amplifier that amplifies both signal quadratures equally (phase-preserving) can do is contribute half of a photon of noise at the measurement frequency [39]. This is known as the standard quantum limit. The focus of this thesis will be on a low-noise cryogenic amplifier based on a dc superconducting quantum interference device (SQUID). The amplifier is both linear and phase-preserving and uses a microwave resonant cavity to couple signals to the SQUID. This device is known as a microstrip SQUID amplifier (MSA) and results from the past decade suggest that these amplifiers can operate with substantial gain near the quantum limit at operating frequencies of hundreds of MHz. Extending the operating frequency of these devices to several GHz while preserving low-noise characteristics and high gain

is the goal of our research.

1.5 Outline

In chapter 2 of this thesis, we will discuss in detail the Josephson junction, an essential component of the dc SQUID. We will then introduce the dc SQUID and present the technique used to operate a SQUID as an amplifier. The chapter will conclude with a discussion of the noise properties of dc SQUID amplifiers in the thermal limit and also in the quantum regime. Chapter 3 will be a survey of current research in low temperature microwave amplifiers, as well as emerging technologies that can achieve near quantum-limited amplification. Chapter 4 introduces the MSA, beginning with a discussion of various microwave resonant circuits and how they can be used to couple a resonant microwave signal to a dc SQUID. This chapter also provides a survey of results from MSAs over the past several years. Chapter 5 will cover the techniques used to fabricate our MSAs. In chapter 6 we will present measurements of low frequency characteristics as well as gain measurements at microwave frequencies for our first generation of MSAs. In chapter 7, results will be presented for a more recent generation of our MSAs that operate at higher frequency. Chapter 8 will begin with a discussion of amplifier noise, and the concept of noise temperature. In the later half of the chapter, results of noise temperature measurements of our MSAs will be presented and discussed. In chapter 9, we present a potential application of one of our MSAs to perform a single-shot measurement of a flux qubit. Chapter 10 will conclude by presenting an outlook for the future of our MSAs.

Chapter 2

The Josephson junction and dc SQUID

2.1 The Josephson tunnel junction

In 1962 Brian D. Josephson was the first to theorize that it is possible for pairs of electrons, Cooper pairs [23], to tunnel from one superconductor to another closely spaced superconductor without dissipation when driven with a suitable current bias [24]. A year later this phenomenon, known as the Josephson effect, was first observed by Anderson and Rowell [25]. Two superconductors separated by a thin non-superconducting barrier is known as the Josephson tunnel junction (Fig. 2.1) and Josephson tunnel junctions have since played an integral role in low temperature physics as well as in several other fields.

Superconducting charge carriers, Cooper pairs of charge $2e$ [40] where e is the electron charge, can tunnel from one superconducting electrode to the other through a weak link while maintaining phase coherence. With zero current driven through the junction, the phases of the superconducting wavefunction in each of the two electrodes are locked, even through the weak link. If a small current is driven through the barrier, Cooper pairs carry charge from one electrode to the other with no voltage

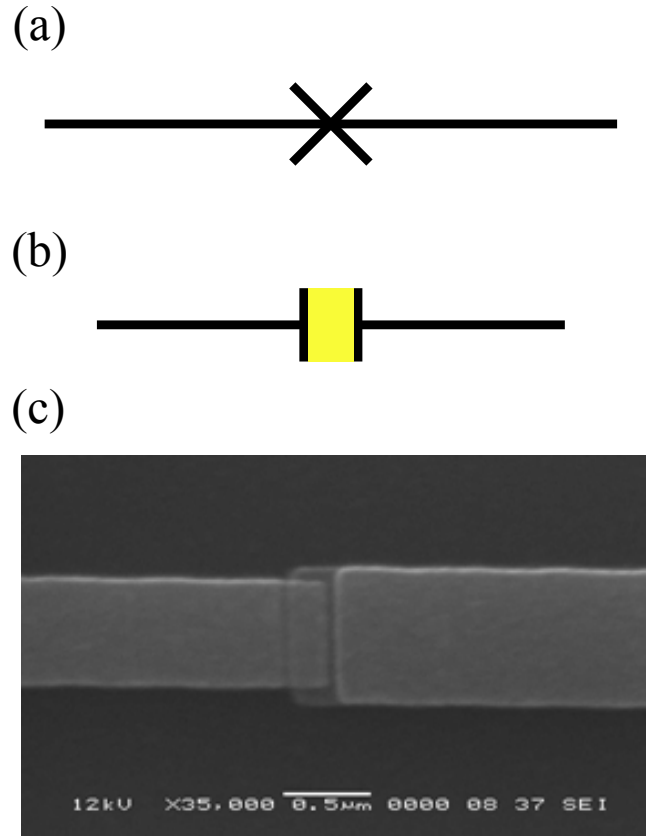


Figure 2.1: (a) Schematic representation of a Josephson tunnel junction circuit element. (b) Schematic of a junction where black wires are superconductors and the yellow area is a non-superconducting material. (c) Scanning electron micrograph of a shadow evaporated Al – AlO_x – Al Josephson junction similar to those used in our devices.

difference developing across the junction, however the difference in the phases of the superconducting wavefunctions $\delta = \phi_1 - \phi_2$ varies according to the first Josephson relation:

$$I = I_0 \sin \delta \quad (2.1)$$

where I_0 is known as the critical current [41]. When the current exceeds I_0 , a voltage V develops across the junction and the phase difference δ becomes time dependent and evolves according to the second Josephson relation:

$$\frac{\partial \delta}{\partial t} = \frac{2eV}{\hbar} = \frac{2\pi V}{\Phi_0} \quad (2.2)$$

where $\Phi_0 = h/2e = 2.07 \times 10^{-15}$ Wb is the magnetic flux quantum. If the current

is further increased to a sufficiently large value, the voltage across the junction will become linear with current and the slope of this line is equal to the inverse of the normal state resistance of the junction, R_N . In this regime Cooper pairs can no longer cross the barrier while maintaining phase coherence and are broken into a pair of quasiparticles [42]. This normal state resistance corresponds to the junction resistance when superconductivity is suppressed either by exceeding the critical temperature of the superconductor, or in the presence of magnetic fields high enough to suppress superconductivity. As the current is reduced the voltage will not return to zero at the critical current of the junction, but at some current less than the critical current. The current-voltage characteristic for a single junction is schematically represented in Fig. 2.2 for the case of two superconductors of identical superconducting gap [43]. The measured critical current of a junction, I_c , is somewhat less than the thermodynamic critical current I_0 . In the absence of fluctuations the critical current takes the value of the thermodynamic critical current, $I_c = I_0$. However, in practice a voltage will develop across the junction at a current of $I_c < I_0$ due to thermal or quantum fluctuations or the presence of external noise. If the critical current of the junction is suppressed to zero, for example by a magnetic field, the current-voltage characteristic will follow the blue path in Fig. 2.2 until the voltage across the junction reaches the gap voltage, then it will continue following the red path. The blue path is known as the quasiparticle branch of the current-voltage characteristic where the current is carried by quasiparticles. In general, the quasiparticle current is not a linear function of V [43], but the details of the quasiparticle conductance are beyond the scope of this thesis.

All Josephson junctions involve some sort of weak link between two superconductors that allows the electron pair wavefunction of the two superconductors to overlap slightly. The most common barrier through which the wavefunctions overlap is a metal oxide. However, junction barriers have been formed from normal metal [44] and semiconductor links [45], grain boundaries [46], narrow constrictions [47],

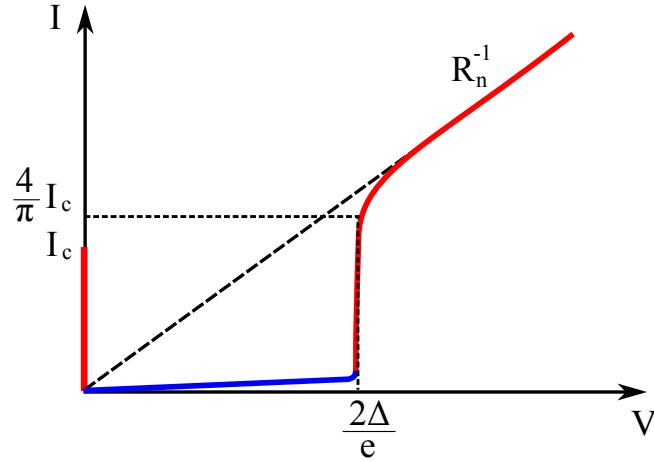


Figure 2.2: Schematic representation of the current-voltage characteristic of a Josephson junction. The quasiparticle branch is represented by the blue curve.

and damaged regions [48]. In this work the Josephson junction will be treated as a superconducting circuit element, which requires a model for its electrical behavior.

2.1.1 The Josephson junction as a circuit element

In this section we will describe the electrical properties of the Josephson junction and develop a circuit model to illustrate the behavior of a junction under the influence of a dc current. From elementary electromagnetism inductance L is defined as $v = L\dot{I}$ where v is the voltage induced in a circuit by the rate of change of the current through the circuit. By employing the Josephson relations, Eqs. (2.1, 2.2), and using the definition of inductance, we can write

$$\frac{\hbar}{2e}\dot{\delta} = LI_0\dot{\delta}\cos\delta. \quad (2.3)$$

Therefore, we can define the Josephson inductance L_J as

$$L_J \equiv \frac{\Phi_0}{2\pi I_0 \cos(\delta)}. \quad (2.4)$$

From this result, we see that the Josephson junction behaves as an inductive element and the value of this inductance depends on the phase difference across the junction.

Our junctions, which are formed by two superconducting aluminum electrodes separated by a aluminum oxide barrier are superconductor-insulator-superconductor (SIS) junctions, an example of which is shown in Fig. 2.1(c). The geometry of a typical SIS junction is that of a parallel-plate capacitor, and there is indeed a small capacitance C associated with junctions of this geometry. Thus, in addition to an inductance, our junctions also have a native capacitance. The combination of the Josephson inductance and the junction capacitance results in a resonant circuit with a plasma frequency given by

$$\omega_p = \frac{1}{\sqrt{L_J C}} = \sqrt{\frac{2eI_0}{\hbar C}} \quad (2.5)$$

when no dc current is driven through the junction such that $\delta = 0$. When the critical current of the junction is exceeded and a voltage V develops across the junction, δ evolves at the Josephson frequency ω_J given by

$$\omega_J = \frac{2e}{\hbar} V. \quad (2.6)$$

In the absence of dissipation, the resonance of a junction is naturally underdamped, thus making the junction hysteretic in its current-voltage dependence. As the current is increased beyond the critical current of the junction, a voltage develops across the junction. As the current is reduced, the junction does not switch back to the zero-voltage state until the current is reduced to some value below the critical current. It is common to add a resistance in parallel with the junction to overdamp the junction, which makes the current-voltage dependence single-valued.

2.1.2 Circuit model – RCSJ

Taking into account the Josephson inductance, the junction capacitance C due to the junction geometry, and the shunt resistance R , the following schematic (Fig. 2.3) applies for a resistively and capacitively shunted Josephson junction (RCSJ) driven with a dc current [49]. We can write a differential equation for the current through

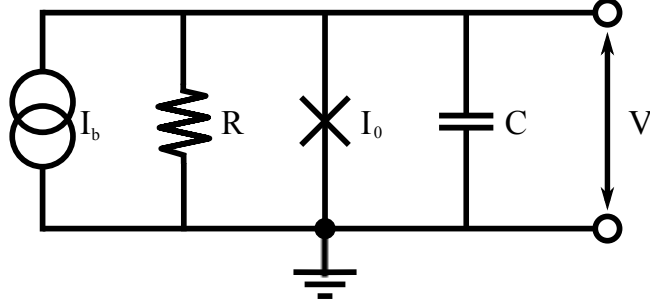


Figure 2.3: Schematic representation of the resistively and capacitively shunted Josephson junction with additional circuitry to current bias the junction and monitor the voltage across the circuit.

each of these elements as a function of the phase difference across the junction δ

$$I_b = C \frac{dV}{dt} + \frac{V}{R} + I_0 \sin \delta. \quad (2.7)$$

Invoking the first Josephson relation, Eq. (2.2), we can write this purely in terms of the phase difference across the junction, δ .

$$I_b = \frac{\hbar C}{2e} \ddot{\delta} + \frac{\Phi_0}{R} \dot{\delta} + I_0 \sin \delta \quad (2.8)$$

By replacing time t with a dimensionless time variable θ [43]

$$\theta = \frac{2e}{\hbar} I_0 R t \quad (2.9)$$

we can rewrite equation 2.8 as

$$\frac{I_b}{I_0} = \beta_c \ddot{\delta} + \dot{\delta} + \sin \delta \quad (2.10)$$

where

$$\beta_c \equiv \frac{2\pi I_0 R^2 C}{\Phi_0} \quad (2.11)$$

is known as the Stewart-McCumber parameter [50],[51]. The Stewart-McCumber parameter characterizes the degree of damping for the junction and can be used to quantify the single-valuedness of the current-voltage characteristic. $\beta_c = 1$ is the crossover point from underdamped to overdamped: for $\beta_c < 1$ the current-voltage

characteristic of the junction is nonhysteretic, for $\beta_c > 1$ the current-voltage characteristic is multivalued. To better understand the dynamics of this system useful analogies can be drawn to more intuitive mechanical systems.

2.1.3 Analogous systems

The equation of motion of a resistively shunted Josephson junction is that of a damped oscillator, hence there are a couple of useful analogies that can be drawn between the RCSJ model and other physical systems. These analogies provide us with intuition when thinking about the dynamics of the RCSJ circuit. These are *the damped driven pendulum* and *the particle on a washboard potential*.

The damped driven pendulum

Let us consider a system composed of a metallic disk containing a mass m at a distance l from the center of the disk as depicted in Fig. 2.4, with a moment of inertia, \mathfrak{M} [43]. The system is driven and damped by locally applied magnetic fields that induce eddy currents in the disk. The equation of motion for this system in terms of pendulum displacement angle ϕ is given by

$$\tau_a = \mathfrak{M}\ddot{\phi} + \frac{1}{D}\dot{\phi} + mgl \sin \phi, \quad (2.12)$$

where D is the viscous damping coefficient and τ_a is the torque applied to the system. Comparing this equation of motion with that of the RCSJ [Eq. (2.10)] we can equate the moment of inertia \mathfrak{M} with the junction capacitance C , the coefficient of viscous damping $1/D$ with shunt resistance R and the critical gravitational torque mgl with the critical current of the junction I_0 . The role of the phase difference across the junction δ is analogous to the angular displacement of the pendulum ϕ . Applying an external torque τ_a to this system is equivalent to driving the junction with a bias current I_b [43].

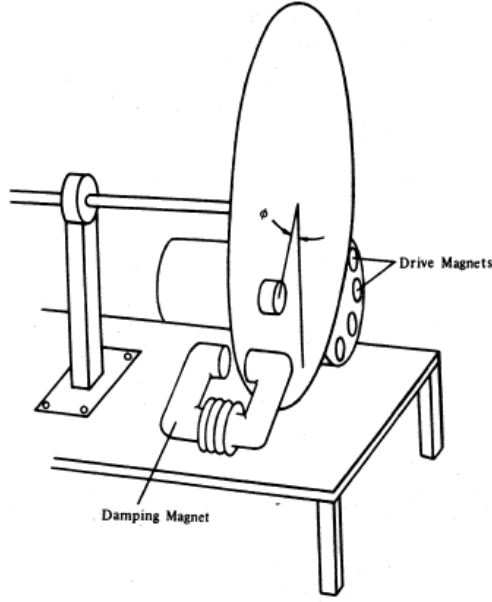


Figure 2.4: Reproduction of T. Vanduzer’s masterpiece schematic of a damped driven pendulum with dynamics analogous to a RCSJ [43]. (from T. Vanduzer and C. W. Turner, 1998, p.202)

As a torque is applied to the pendulum, the angular displacement of the pendulum ϕ increases until the applied torque is balanced by the gravitational restoring torque. At this point the pendulum remains at a fixed ϕ — just as the phase difference across the junction δ is fixed for a given bias current $I_b < I_0$. There is a value of applied torque τ_{ac} that will cause the pendulum to exceed angular position $\phi = 90^\circ$, at which point the gravitational restoring torque decreases in magnitude from its maximum value and the pendulum goes into rotation at average angular velocity $\langle \dot{\phi} \rangle$. This critical torque is analogous to the critical current I_0 of the junction. An important observation is that the mass is not concentrically distributed on the disk, thus the angular velocity of the disk will depend on whether the gravitational restoring torque is adding to the applied torque, or working against it — hence the oscillations are very non-sinusoidal $\dot{\phi} \neq \langle \dot{\phi} \rangle$. This scenario is analogous to increasing the dc current through the junction which increases the phase difference across the junction δ . When the critical current of the junction is exceeded the phase difference

becomes time dependent and the phase evolves dynamically, corresponding to the junction switching into the voltage state. The average voltage, proportional to $\langle \dot{\delta} \rangle$, differs from the instantaneous voltage which is proportional to $\dot{\delta}$ [43].

Once the applied torque exceeds τ_{ac} the pendulum is undergoing rotation. As the torque is reduced slightly below τ_{ac} the pendulum continues to rotate despite the fact the applied torque is less than the torque required to initiate rotation. This mechanical hysteresis is analogous to the hysteresis in the current-voltage characteristic of an underdamped RCSJ, and this hysteresis can be quantified by a parameter \mathfrak{B}_c

$$\mathfrak{B}_c = mglD^2\mathfrak{M}. \quad (2.13)$$

For values of $\mathfrak{B}_c > 1$, where the system is underdamped, the angular frequency of the pendulum will be hysteretic in the applied torque. Hysteresis can be eliminated by overdamping the system, corresponding to $\mathfrak{B}_c < 1$. System damping, hence \mathfrak{B}_c can be changed by increasing or decreasing the damping coefficient $1/D$, as β_c can be changed by increasing or decreasing the resistance shunting the junction R [43].

Ball in a washboard potential

Another useful analogy that captures the dynamics of a RCSJ is a ball on a washboard potential [41]. The position of the ball represents the phase across the junction, and the ball — known as the phase particle — is confined to the junction potential $U = -(\Phi_0/2\pi)(I_b\delta + I_0 \cos \delta)$. The mass of the phase particle is analogous to the capacitance of the junction. The slope of the washboard potential can be tilted by driving a current through the junction. As the tilt of the washboard increases, the ball will change position to minimize its potential energy, but will remain in the same potential well. This is analogous to the current dependence of the phase across the junction. As the tilt of the washboard further increases, there will be a point at which the slope at every point on the washboard is negative and the ball will escape the local potential and roll freely down the washboard. This state is analogous to driving

a current through the junction beyond the critical current such that the phase across the junction evolves with time. This is known as the running state and in this state a dc voltage is developed across the junction proportional to the time average of the phase [41].

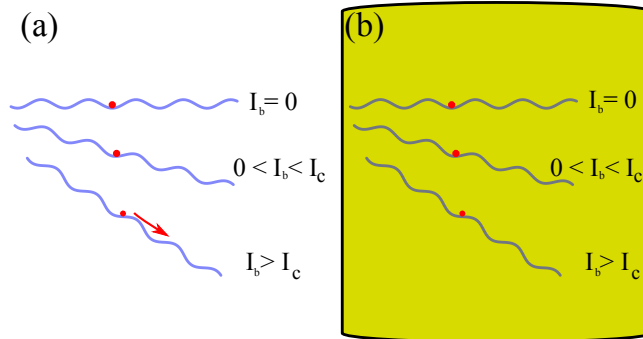


Figure 2.5: (a) Particle in a washboard potential for different values of bias current I . For values of tilt that correspond to $I_b > I_c$ the particle cascades down the potential if underdamped. (b) Damping can be added to this system by submersing it in a viscous liquid. If the tilt exceeds the current corresponding to I_0 then is subsequently reduced, the particle remains in a local minimum.

With the ball in the running state, if the tilt of the potential is reduced such that there are now areas where the slope is locally positive, the ball will continue to roll due to its inertia, analogous to the junction capacitance. This is analogous to the hysteresis in the current-voltage characteristic of the junction. Damping can be added to this situation by immersing the washboard in a viscous fluid. For sufficiently large damping, the ball will become trapped in a potential as soon as the slope of the potential becomes locally positive. The equations of motion for this system can also be recast in a form similar to those of a RCSJ with a damping parameter analogous to the parameter β_c [41].

2.1.4 Josephson junctions in magnetic fields

We saw above that the current through a junction is related to the phase difference across the junction [Eq. (2.1)]. It is assumed that the phase difference across the

junction is identical at every point in the junction area, however this is only true in the absence of a magnetic field. If a field is applied in the plane of the junction, along the y – axis, the phase difference across the junction becomes a function of space along the z – axis (Fig. 2.6). The phase difference across a junction is a gauge invariant quantity, so for convenience we choose the London gauge, that requires the gradient of the phase of the superconducting wave function to vanish inside of the electrodes ($\nabla\phi = 0$) [43]. In general, the phase difference across a junction δ is given

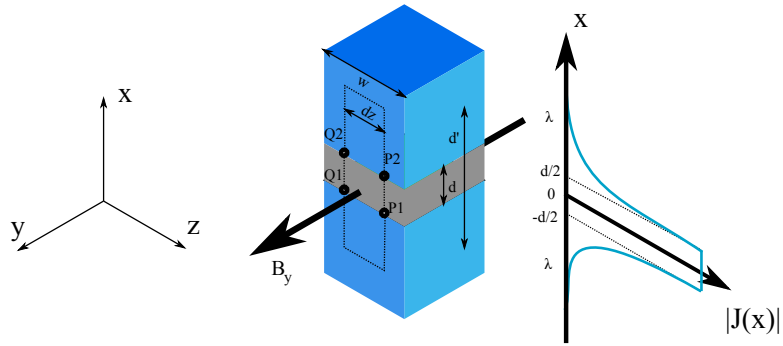


Figure 2.6: A schematic of a rectangular junction of width w and thickness d in the presence of a magnetic field along the y -axis. The magnetic thickness of the junction is $d' = d + 2\lambda$. A schematic of the current density along the x -axis is included to clarify the discussion.

by

$$\delta = \phi_2 - \phi_1 + \frac{2e}{\hbar} \int_1^2 \mathbf{A}(\mathbf{r}, \mathbf{t}) \cdot d\mathbf{l} \quad (2.14)$$

where \mathbf{A} is the vector potential and the path of integration is defined by two points on either side of the junction, for instance points $Q1$ and $Q2$ or points $P1$ and $P2$ in figure 2.6. Choosing two pairs of points across the junction, laterally separated, the phase varies between these two points by

$$\delta(P) - \delta(Q) = \frac{2e}{\hbar} \left[\int_{P1}^{P2} \mathbf{A}(\mathbf{P}, \mathbf{t}) \cdot d\mathbf{l} - \int_{Q1}^{Q2} \mathbf{A}(\mathbf{Q}, \mathbf{t}) \cdot d\mathbf{l} \right]. \quad (2.15)$$

The integral of the vector potential around the contour in Fig. 2.6 yields the flux threading the contour, Φ_y . The path of integration between points $Q1, P1$ and $P2, Q2$

are taken to be deep in the superconductor where the current density is zero [43]. Therefore, Φ_y is equal to the bracketed portion of the right hand side of Eq. (2.15) [43]

$$\delta(P) - \delta(Q) = \frac{2e}{\hbar} \Phi_y. \quad (2.16)$$

The total flux enclosed through the junction depends on the junction geometry and the penetration depth of the superconductor λ . For a junction barrier of thickness d , the magnetic thickness of the junction is $d' = d + 2\lambda$ assuming both superconductors are the same material. A differential equation can be written to describe the variation of the phase across the junction along the z - axis [43]. For an infinitesimally small distance dz between points Q and P, the magnetic flux is $B_y dzd'$. Therefore

$$\frac{\partial \delta}{\partial z} = \frac{2ed'}{\hbar} B_y. \quad (2.17)$$

Integrating this equation gives the following expression

$$\delta(z) = \frac{2ed'}{\hbar} B_y z + \delta(0) \quad (2.18)$$

where $\delta(0)$ is a constant of integration [43].

Since the critical current of a junction depends on the difference of phase across the junction barrier, and if this phase difference is now a function of a spatial coordinate, the current density $J(z)$ and critical current density $J_c(z)$ must be introduced. The current-phase relation, Eq. (2.1) is rewritten in terms of current density as

$$J(z) = J_c(z) \sin[\delta(z)]. \quad (2.19)$$

Using the expression for $\delta(z)$ Eq. (2.18), the expression above for $J(z)$ and integrating over z , an expression for the critical current of the junction as a function of magnetic field is obtained

$$I_c(B) = I_c(0) \left| \frac{\sin(ed'LB/\hbar)}{(ed'LB/\hbar)} \right| \quad (2.20)$$

where L is the extent of the junction in the y direction and $I_c(0) = J_c(z)wL$ is the critical current density times the junction area. Recognizing that $d'LB$ is the total

flux enclosed in the junction Φ and that $e/\hbar = \pi/\Phi_0$, Eq. (2.20) is rewritten as

$$I_c(\Phi) = I_c(0) \left| \frac{\sin(\pi\Phi/\Phi_0)}{\pi\Phi/\Phi_0} \right|, \quad (2.21)$$

where $I_c(0)$ is the maximum critical current in the absence of a magnetic field [43]. The phase relationship for a Josephson junction in a magnetic field is analogous to the diffraction of light through an aperture. In both cases a Fraunhofer diffraction pattern is produced (Fig. 2.7). When n integer flux quanta are applied through the junction, $\Phi = n\Phi_0$, the phase relationship results in equal amounts of positive and negative critical current densities in the junction resulting in a net zero critical current. In this case, the measured critical current of the junction vanishes. This

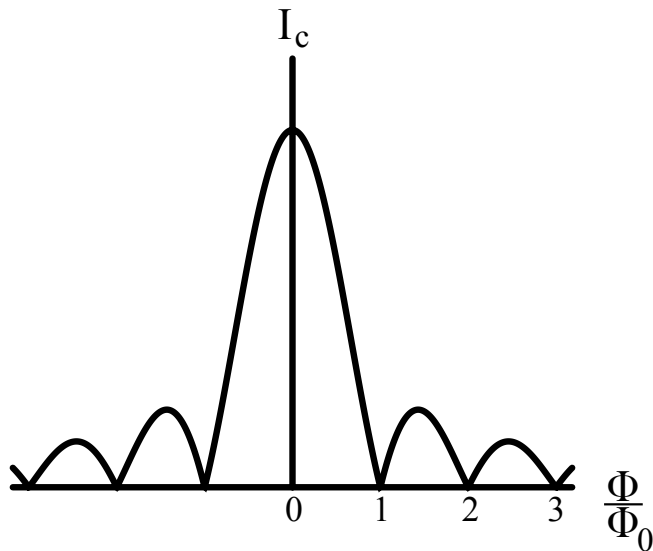


Figure 2.7: A schematic of the dependence of the measured critical current I_c as a function of flux threading the junction.

interference behavior is analogous to the far field diffraction of plane waves of light from a narrow slit. We will see, in later sections, that this analogy carries over to the case of a SQUID where two Josephson junctions are connected in parallel with superconducting traces. The measured critical current of the SQUID in the presence of applied flux will exhibit a similar interference pattern as the interference of light from two narrow slits [43].

2.2 The dc superconducting quantum interference device

The dc superconducting quantum interference device (Fig. 2.8) consists of two tunnel junctions connected in parallel by superconducting traces. The behavior of dc SQUIDS under the influence of a bias current and in the presence of flux will be discussed, as well as how this device can be used to transduce a flux to a voltage.

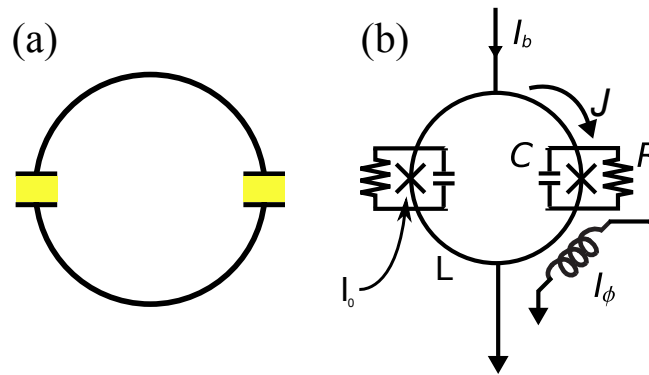


Figure 2.8: (a) An isolated dc SQUID loop. (b) Circuit schematic of a RCSJ SQUID with bias current line and flux bias coil. The bias current I_b divides symmetrically around the SQUID loop, and circulating currents J are induced by an externally applied magnetic flux produced by driving I_ϕ through an inductance.

2.2.1 Bias dependence and the SQUID potential

The unshunted dc SQUID with a flux bias of $n\Phi_0$ and small β_L behaves very much like a single tunnel junction when a dc current is applied. Assuming identical junctions, an applied bias current will divide symmetrically such that each junction experiences the same bias current. In this scenario, the dc SQUID has a critical current which is equal to twice the critical current of a single junction. When the critical current of the SQUID is exceeded, a voltage develops across the SQUID equal to $2\Delta/e$. For large values of bias current at voltages beyond the gap voltage, the voltage across the SQUID will depend linearly on the current applied. The slope of this I-V characteris-

tic is proportional to the inverse of the normal state resistance of the SQUID, which is the parallel combination of the normal state junction resistances. As the current is decreased, the SQUID does not return to the zero-voltage state until the applied current is far below the critical current. This hysteresis is a result of the junctions being underdamped and the analogies used to describe the behavior of a single junction can be generalized to apply to the dc SQUID in the absence of a magnetic field.

This hysteresis in the current-voltage characteristic can be eliminated by the same mechanism as with a single junction, by shunting each of the two junctions with a resistance. A shunt resistance value that causes the junction to be overdamped will eliminate the hysteretic current-voltage dependence of the SQUID, as depicted in Fig. 2.8(b).

Let us consider a SQUID of geometric inductance L with an applied magnetic flux of Φ_{ex} with no applied bias current. A circulating current J is induced in the SQUID loop due to screening, which will either combine with, or oppose Φ_{ex} . If Φ_{ex} is increased from zero, the direction of the screening currents will produce flux which will partially oppose the external flux $\Phi = LJ$. As Φ_{ex} is further increased the magnitude of the screening current increases until it approaches the critical current of one of the junctions. The screening current will then change direction. The ability for a SQUID to shield an applied flux is limited by the product of the SQUID inductance L and the maximum zero voltage current of a junction I_0 . The SQUID screening parameter, β_L , is defined as the ratio of the maximum screening flux to $\Phi_0/2$

$$\beta_L = \frac{2LI_0}{\Phi_0}. \quad (2.22)$$

Due to these screening currents, the critical current of the SQUID will vary with flux bias. For $\Phi_{ex} = 0$ the bias current I_b will divide symmetrically around the SQUID loop so each junction sees the same bias current. For a non zero flux bias a screening current will be induced in the SQUID which will either flow clockwise or counterclockwise. In the presence of a bias current and a screening current one junction will have J and I_b in the same direction, and in the other junction the currents will

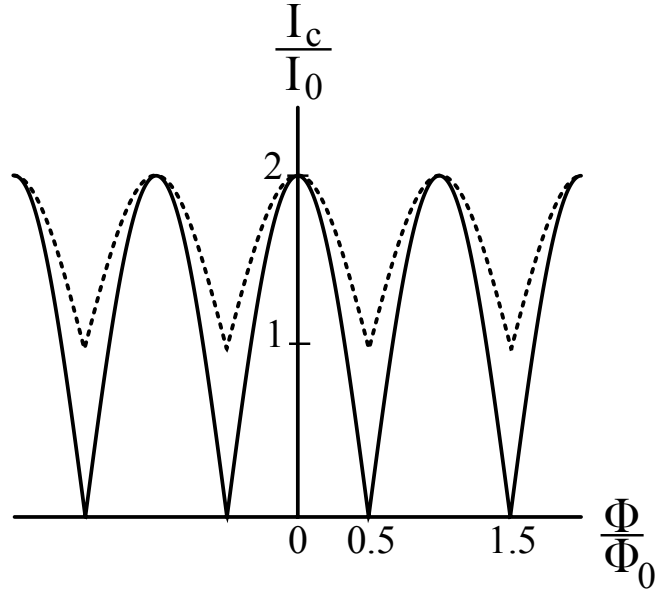


Figure 2.9: Schematic of the flux dependence of the measured critical current of a SQUID in a magnetic field. Solid line is for a SQUID of negligible screening parameter β_L , dashed line is for a SQUID with $\beta_L \approx 1$.

oppose each other. Therefore, one junction will reach its critical current I_0 sooner than it would have in the absence of an applied flux. For values of β_L much less than 1, the critical current of the SQUID can be modulated from its maximum value of $2I_0$ to zero. For a SQUID with $\beta_L \approx 1$, the critical current of the SQUID can be modulated from its maximum value $2I_0$ down to $\sim I_0$ (Fig. 2.9).

A useful tool for understanding the dynamics of a SQUID is the phase particle model [52], previously described for the case of a single junction. For a SQUID where the phase difference across each of the two junctions may be different, we must extend this analogy into 2 dimensions. The dynamics of the phase particle is described by a set of coupled equations [49]:

$$J/I_0 = (\delta_1 - \delta_2 - 2\pi\Phi_{ex}/\Phi_0)/\pi\beta_L \quad (2.23)$$

$$V = (\dot{\delta}_1 + \dot{\delta}_2)\Phi_0/4\pi \quad (2.24)$$

$$\beta_c \frac{\ddot{\delta}_1}{I_0} \left(\frac{\Phi_0}{2\pi R} \right)^2 + \dot{\delta}_1 \left(\frac{\Phi_0}{2\pi R} \right) = \frac{I_b}{2} - J - I_0 \sin \delta_1 \quad (2.25)$$

$$\beta_e \frac{\ddot{\delta}_2}{I_0} \left(\frac{\Phi_0}{2\pi R} \right)^2 + \dot{\delta}_2 \left(\frac{\Phi_0}{2\pi R} \right) = \frac{I_b}{2} + J - I_0 \sin \delta_2. \quad (2.26)$$

From the equations of motion we can extract the potential $U_{SQUID}(\delta_1, \delta_2)$ that the phase particle experiences [52]

$$\frac{U_{SQUID}}{2E_J} = \frac{1}{\pi\beta_L} \left(\frac{\delta_1 - \delta_2}{2} - \pi \frac{\Phi_{ex}}{\Phi_0} \right)^2 - \cos \left(\frac{\delta_1 - \delta_2}{2} \right) \cos \left(\frac{\delta_1 + \delta_2}{2} \right) - \frac{I_b}{2I_0} \left(\frac{\delta_1 + \delta_2}{2} \right). \quad (2.27)$$

The first term in Eq. (2.27) is the inductive energy of the SQUID and accounts for the global parabolic shape of the potential energy landscape due to the inductive nature of the SQUID. Therefore, this term is not present in the expression for the potential energy of a single junction. The second term arises from the phase constraints across the junctions going around the SQUID loop. For a single junction this term would only involve one cosine, producing a washboard potential. For a SQUID this term produces a ‘mogul field’-like potential. The final term is related to the tilt of the potential, similar to the tilt in the washboard potential for a single junction. A convenient choice of coordinates are the sum of the phases $x = (\delta_1 + \delta_2)/2$ and the difference of phase $y = (\delta_1 - \delta_2)/2$ as the potential can be tilted along the x -axis with an applied bias current I_b , or the position of the cosine potential can be translated across the parabolic sheet with an applied bias flux Φ_{ex} . The global curvature of the potential along the y -axis is related to the screening parameter $1/\beta_L$ and in the case of $\beta_L \ll 1$ we approach the one dimensional dynamics of a single junction due to the steep curvature of the potential walls. Recast in terms of these new variables, the SQUID potential becomes [52]

$$\frac{U_{SQUID}}{2E_J} = \frac{1}{\pi\beta_L} \left(y - \pi \frac{\Phi_{ex}}{\Phi_0} \right)^2 - \cos x \cos y - \frac{I_b}{2I_0} x. \quad (2.28)$$

The SQUID potential is plotted in Fig. 2.10 for several values of I_b , Φ_{ex} and β_L . The concept of the SQUID potential will be especially important for the discussion of our experiments on lumped-element SQUID oscillators, which will be addressed in chapter 9.

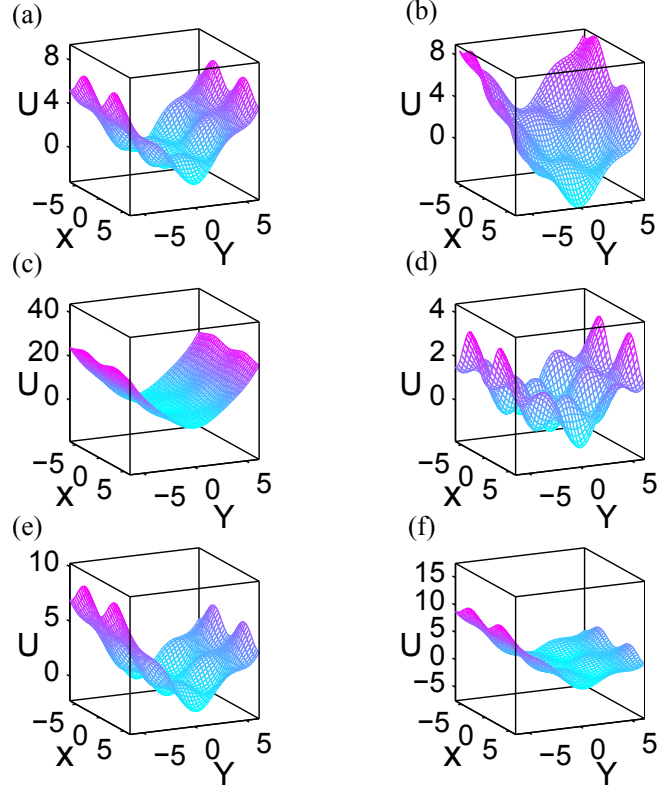


Figure 2.10: (a) SQUID potential plotted for several values of I_b , Φ_{ex} and β_L in the x and y basis. (a) $I_b = 0, \Phi_{ex} = 0, \beta_L = 2$. (b) $I_b = I_0/2, \Phi_{ex} = 0, \beta_L = 2$. (c) $I_b = 0, \Phi_{ex} = 0, \beta_L = .5$. (d) $I_b = 0, \Phi_{ex} = 0, \beta_L = 5$. (e) $I_b = 0, \Phi_{ex} = \Phi_0/4, \beta_L = 2$. (f) $I_b = 0, \Phi_{ex} = \Phi_0/2, \beta_L = 2$.

2.2.2 Flux-to-voltage transduction

For the following discussion we assume the junctions of the SQUID are resistively shunted, such that $\beta_c < 1$. For a SQUID that is current biased slightly above its critical current in the presence of zero external flux ($\Phi_{ex} = 0$), a small voltage will be developed across the SQUID [43]. As the external flux is increased from zero, the current-voltage characteristic will deform due to suppressing of the critical current of the SQUID and the voltage across the SQUID will increase. As the external flux is further increased, the voltage across the SQUID will continue to increase until the flux threading the SQUID reaches a value of $\Phi_{ex} = \Phi_0/2$ and the critical current of the SQUID is at its minimum. Increasing the flux further will cause

the critical current of the SQUID to increase as the circulating currents have now changed direction and are decreasing in magnitude, and the voltage across the SQUID decreases until it reaches its minimum at an external flux of $\Phi_{ex} = \Phi_0$ [41]. This voltage-flux characteristic is thus periodic in external flux with a period of Φ_0 and a typical response is schematically illustrated in Fig. 2.11.

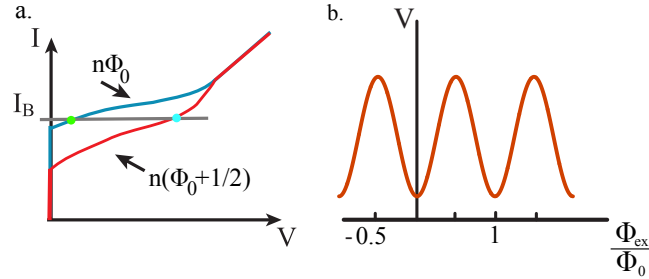


Figure 2.11: (a) Current-voltage characteristic for a SQUID with an applied flux of $\Phi_{ex} = n\Phi_0$ (blue) and $\Phi_{ex} = (n + 1/2)\Phi_0$ (red). (b) $V-\Phi$ characteristic for a SQUID current biased above the critical current (grey line in (a)).

2.3 dc SQUIDS as amplifiers

SQUIDS are the most sensitive detectors for magnetic flux and their applications span disciplines from gravitational wave detection [53] to medical imaging [54], [55]. In this section and for the rest of this thesis, with the exception of chapter 9, we will consider one particular application of SQUIDS, that is to detect a small flux signal coupled to the SQUID through an input circuit [56]. Understanding the behavior of a SQUID in the presence of an external flux and a bias current is essential for operating a dc SQUID as an amplifier. To operate a dc SQUID such that the flux threading the SQUID loop is transduced to a voltage across the SQUID requires control of both the current bias and the flux bias as well as an appropriate choice of SQUID parameters, including I_0 , β_c , β_L , R and L . In the previous section, the voltage-flux characteristic of a SQUID current biased slightly above the critical current was illustrated. The flux-to-voltage transduction, or SQUID transfer function, is periodic

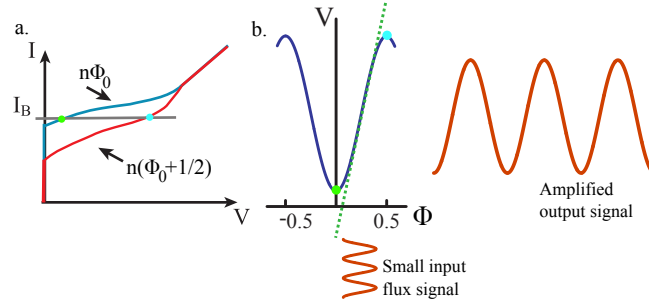


Figure 2.12: Schematic of the amplification process. (a) The current-voltage characteristic for an RCSJ SQUID current biased above the critical current. (b) Amplification process in the flux-voltage characteristic picture. A small ($\Phi < \Phi_0$) flux signal modulates the critical current of the SQUID between its minimum and maximum value. When current biased above the critical current (grey line), this produces an amplified voltage signal across the SQUID.

in Φ_0 and offset from $V = 0$. In practice the shape of the flux-to-voltage transfer function varies with SQUID geometry. For certain flux bias conditions, Φ_{ex} around $(n + 1/4)\Phi_0$, the transfer function of the SQUID can be nearly linear and a small oscillatory flux signal, in addition to our static flux bias Φ_{ex} , will result in oscillations in the voltage across the SQUID. When operated at this approximately linear point of the SQUID transfer function, the dc SQUID will transduce a small flux signal to a measurable voltage across the SQUID loop in essence amplifying the flux signal with a gain proportional to the slope of the $V - \Phi$ curve, or the transfer function, $\partial V / \partial \Phi$. The small-signal amplification process is schematically depicted in Fig. 2.12. If the signal amplitude becomes comparable to Φ_0 , the output will be considerably nonlinear, and if the amplitude exceeds $\sim \Phi_0$, the output will not even be monotonic. For amplifying larger signals, a flux-locked feedback loop is typically employed to maintain the linearity of the V_Φ curve for large input flux signals [49].

2.4 Practical SQUID amplifiers

There are many realizations of SQUID amplifiers. In this section we will focus on a discussion of thin film SQUIDs where the SQUID loop is planarized to a SQUID

washer, and the washer is strongly coupled to a thin film input coil separated from the SQUID washer by a dielectric layer. Throughout this sections the terms ‘SQUID loop’ and ‘SQUID washer’ are used interchangeable and they both refer to a planar geometry. The input circuit consists of a signal source V_i which will be amplified, a load resistor R_i , and an inductor L_i that will couple the current flowing through the input circuit to the SQUID loop through mutual inductance $M_i = \alpha(LL_i)^{1/2}$ where α is the coupling coefficient (Fig. 2.13). Input circuits can be tuned to couple flux to the SQUID resonantly for signals tuned to the input circuit characteristic frequency by adding a capacitor C_i in series with L_i [56]. The SQUID has loop inductance L and is

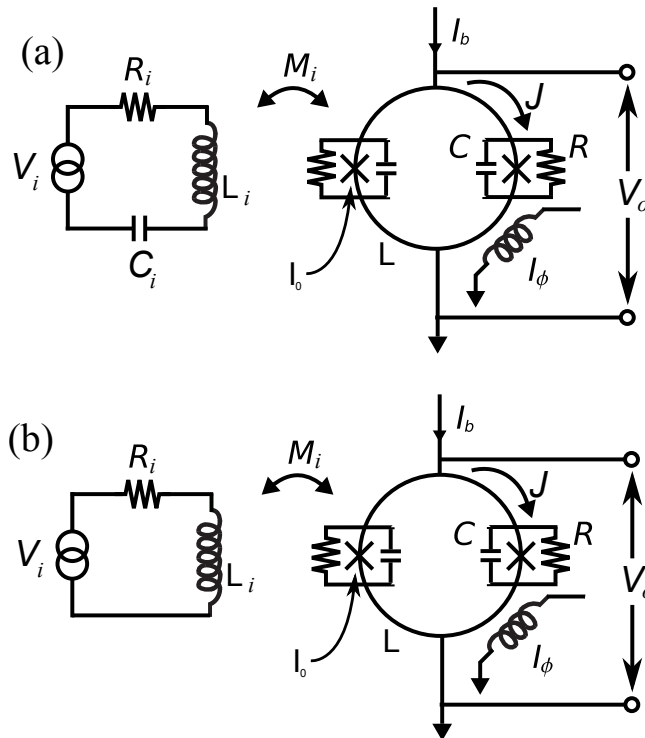


Figure 2.13: (a) A dc SQUID amplifier inductively coupled to a tuned input circuit. (b) A dc SQUID amplifier inductively coupled to an un-tuned input circuit. (reproduction of a figure from [56])

biased with a current I_b and a flux I_ϕ . Each tunnel junction has a critical current I_0 , self capacitance C and shunt resistance R which keeps the junctions nonhysteretic. There is a voltage developed across the SQUID V_o and circulating current J induced

in the SQUID loop. The proximity of the input coil to the SQUID reduces the inductance of the SQUID L to $L_r = (1 - \alpha_e^2)L$ where $\alpha_e^2 = \alpha^2/(1 + L_T/L_i)$ and L_T is the sum of the total inductance of the input circuit including stray inductances [57], [58]. For a tuned amplifier, the total input circuit impedance is given by

$$Z_T = R_i + i\omega L_T + \frac{1}{i\omega C_i}. \quad (2.29)$$

The SQUID parameters $\beta_L \approx 1$, $\beta_c \approx 1$, and the bias conditions I_b, I_ϕ are chosen such that the flux-to-voltage transfer function is given by $V_\Phi = |(\frac{\partial V}{\partial \Phi})| \approx R/L$. The input signal voltage results in a current V_i/Z_T flowing through L_i . This results in an output voltage $V_o = \frac{V_i}{Z_T} M_i V_\Phi$. The voltage gain of the amplifier is given by the ratio of the output voltage to the input voltage [56]

$$G_v = \left| \frac{V_o}{V_i} \right| = \frac{M_i V_\Phi}{Z_T} \quad (2.30)$$

and the power gain is given by

$$G \approx \left| \frac{V_o}{V_i} \right|^2 \frac{R_i}{R_D} = \frac{M_i^2 V_\Phi^2 R_i}{R_D |Z_T|^2} \quad (2.31)$$

where R_D is the dynamic output resistance of the SQUID [56].

dc SQUID amplifiers coupled to a tuned input circuit have been studied analytically, numerically and experimentally. Due to the complicated dynamics of the SQUID and the coupling between the SQUID and external circuitry, accurate modeling of a dc SQUID amplifier has proven to be a difficult task. For instance, the strong inductive coupling to an input circuit reduces the inductance of the SQUID, which makes the amplifier performance difficult to predict for a given input circuit and SQUID. Also, stray capacitance between turns of the input coil and the distributed capacitance between the input coil and the SQUID washer have a large impact on the impedance of the SQUID and input circuit [58]. There is no straightforward model for a dc SQUID strongly coupled to an input circuit that takes these effects into account. However, the case of an isolated SQUID and a SQUID weakly coupled to input circuitry has been modeled successfully. One great success of these models is in

understanding the noise properties of an isolated dc SQUID. Key results are outlined in the next section.

2.4.1 SQUID noise

There are several sources of noise in a dc SQUID, including shot noise in the junctions [59], thermal rounding of the I-V curve near $V = 0$ [60], low frequency critical current fluctuations [61], and Johnson-Nyquist noise produced by the shunt resistors [62]. Even in the presence of optimal filtering of electrical leads and magnetic shielding, low frequency flux noise and critical current fluctuations with a $1/f$ -like power spectrum persist and have been under investigation for several decades [63, 64]. For our applications, involving amplification of microwave signals, these sources of low frequency noise can be neglected. In the frequency range relevant to our research, the SQUID noise is dominated by Johnson-Nyquist noise from the shunts.

A useful metric for quantifying the noise properties of any amplifier is the noise temperature T_N . A brief discussion of noise temperature is to follow, however this topic will be discussed in more detail in later chapters. Noise temperature is used to quantify the noise added to a signal during amplification compared to the Johnson-Nyquist noise produced by a resistor at temperature T_N . A concise description of noise temperature is given in [65], and I will follow that approach here. Consider a system composed of an amplifier of gain G with a resistor R at temperature T connected to its input [Fig. 2.14 (a)], we will refer to this as ‘system A’. The noise power measured at the output of the amplifier has two contributions — the Johnson-Nyquist noise of the resistor amplified by G , and the noise of the amplifier itself. As the temperature T of the resistor R is varied, the Johnson-Nyquist noise produced by the resistor will change according to $v_n = \sqrt{4k_B T R \Delta f}$ where k_B is Boltzmann’s constant and Δf is the measurement bandwidth. As we reduce the temperature of the resistor, the total noise at the output of the amplifier will become smaller and at zero temperature only the amplifier noise will contribute to the total system noise. Now consider an

identical copy of this system, ‘system B’, but the amplifier is replaced with an ideal noiseless amplifier with gain G that contributes no noise to the measurement [Fig. 2.14 (b)]. The amplifier’s noise temperature T_N is defined as the temperature of the resistor in system B such that the noise power for system B is equal to system A with the resistor at zero temperature.

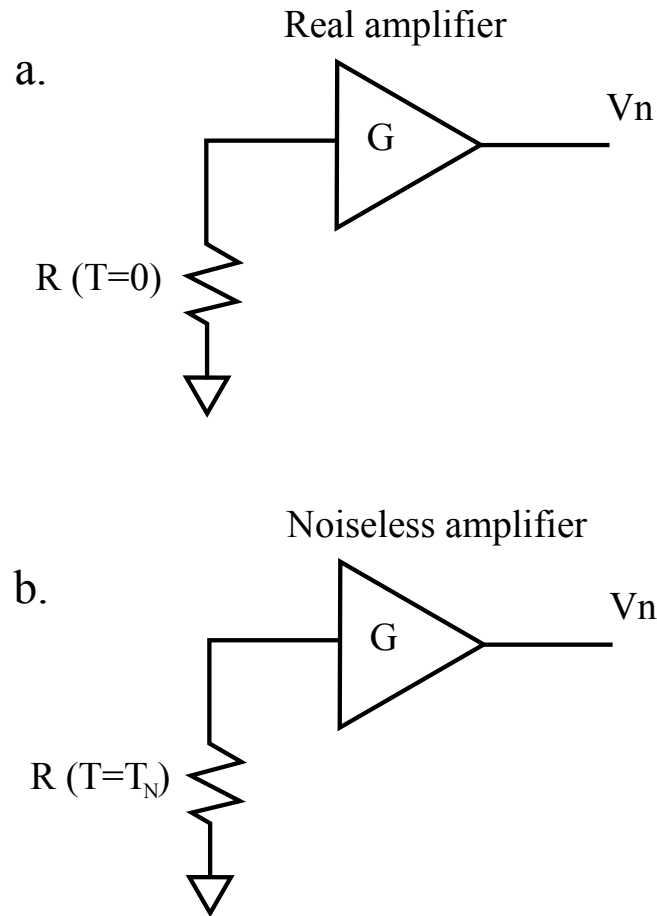


Figure 2.14: Schematic to describe the noise temperature of an amplifier. (a) Amplifier with an impedance at its input that can be cooled to $T = 0$ K. (b) An ideal copy of the amplifier in part (a) which is noiseless.

Claudia Tesche and John Clarke studied the voltage noise in a bare dc SQUID numerically, assuming that each of the two shunt resistors produced uncorrelated white noise of voltage spectral density $S_V^N = 4k_B T R$ [62, 66]. Using the dimensionless time variable θ , the random voltages $v_{1,2}(\theta)$ were approximated by trains of voltage

pulses of duration $\Delta\theta$ and random amplitude v_k . In dimensionless units, the equations of motion for the circulating current, j , the voltage across the SQUID, v , and the phases across the two junction δ_1, δ_2 are given by the equations of motion presented earlier, Eqs. (2.23, 2.24, 2.25, 2.26), with additional voltage noise terms v_{N1} and v_{N2} added to Eqs. (2.25, 2.26), respectively. $v(\theta)$ was obtained by integrating the equations of motion and from this, the noise spectral density S_V was calculated. The addition of voltage noise when integrating the equations of motion resulted in a series of noise-broadened peaks at the Josephson frequency and its harmonics. Well below the Josephson frequency, where the SQUID would be operated as an amplifier, the spectral density was determined to be white. For a SQUID with $\beta_L = 1$ and biased such that $V_\Phi \approx R/L$, the voltage spectral density was calculated to be $S_V(f) = 16k_BTR$ referred to the input of the circuit [62]. Due to the nonlinearity of the SQUID this spectral density is 8 times greater than what one would expect for the Johnson-Nyquist noise produced by the SQUID's shunt resistance $R/2$, in the absence of the rest of the SQUID circuit. The circulating current noise, $i(\theta)$, was also obtained using this technique and the power spectral density for the circulating current noise was found to be $S_J = 11k_BTR/R$ [66]. In addition, the nonlinearity of the SQUID results in a correlation between the voltage and circulating current noise given by $S_{VJ} = 12k_BTR$ [66].

In general, resistive elements in amplifiers give rise to two types of noise, voltage noise e_n in series with the input, and an input noise current i_n [65]. The input current noise across the source impedance also gives rise to a voltage noise. The root-mean-square (RMS) noise referred to the input of the amplifier is $e_a = (e_n^2 + (Z_s i_n)^2)^{1/2}$, where Z_s is the source impedance. For a low source impedance, the voltage noise dominates and for a large source impedance, the current noise dominates. This model for understanding amplifier noise requires consideration of the input circuit of the amplifier as evidenced by the presence of the source impedance term Z_s in the expression above. The SQUID noise spectral densities presented in the preceding

paragraph were obtained for a bare SQUID, absent of any input circuit. However, to operate a SQUID as a practical amplifier, an input circuit is essential. Hilbert and Clarke [56] combined these SQUID noise results and the theory for a SQUID amplifier with a tuned input circuit to understand the effect of noise on a SQUID amplifier and to estimate its noise characteristics.

For the tuned amplifier in Fig. 2.13(a) an expression for the voltage measured across the SQUID can be constructed, taking into account both the voltage noise $V_N^r(\omega)$ derived from S_V and the current noise $J_N^r(\omega)$ from S_J , where the superscript r denotes the ‘reduced SQUID’. In the reduced SQUID model the reduction of the inductance of the SQUID by the presence of the input circuit is taken into account. The voltage at the output of the SQUID has two components: the amplified signal from the input circuit, and the noise $V_N(\omega)$ [56]

$$V_o(\omega) = \frac{M_i V_i V_\Phi^r}{Z_T^*(\omega)} + V_N(\omega) \quad (2.32)$$

where $V_N(\omega)$ is the voltage noise across the SQUID

$$V_N(\omega) = V_N^r(\omega) + \alpha_e^2 L V_\Phi^2 (R_i + 1/i\omega C_i) J_N^r(\omega) / Z_T^*(\omega) \quad (2.33)$$

where Z_T^* is the total loaded impedance of the input circuit [56]. The amplifier is now assumed to operate at its resonant frequency $f_0 = \omega_0/2\pi$, determined by the resonant frequency of the input circuit. On resonance, the imaginary terms of Z_T^* tune to zero.

The expression for the voltage noise at the output of the SQUID becomes:

$$V_N(\omega_0) = V_N^r + \frac{\alpha_e^2 L (R_i + 1/i\omega_0 C_i) J_N^r(\omega_0) V_\Phi^r}{R_i + \Delta R_i} \quad (2.34)$$

where ΔR_i takes into account the dynamic inductance and resistance of the input circuit reduced by the presence of the SQUID [56]. For an input circuit of high quality factor Q such that $R_i \ll 1/\omega C_i$ it is assumed that the SQUID parameters take on their unloaded values, [56] thus

$$V_N(\omega_0) \approx V_N^0(\omega_0) - i\omega_0 M_i^2 V_\Phi J_N(\omega) / (R_i + \Delta R_i) \quad (2.35)$$

where V_N^0 is the voltage noise across the bare, unloaded SQUID [56]. For an unloaded SQUID with $\beta_L \approx 1$ and biased such that $V_\Phi \approx R/L$ the noise temperature is

$$T_N(\omega_0) \approx \sqrt{(\gamma_V \gamma_J)} \frac{\omega_0 T}{V_\Phi} \quad (2.36)$$

where $\gamma_V = 8$ and $\gamma_J = 5.5$ are the weighted noise spectral densities determined from numerical simulations as discussed earlier in this chapter. This expression also assumes the SQUID is well noise-matched to the source impedance. This condition is satisfied when the ratio of the voltage noise to the current noise—the noise impedance—is approximately equal to the source impedance, Z_s . Although this model is for a lumped-element tuned input circuit whereas the input circuit for our amplifiers are distributed element, the expression for $T_N(\omega_0)$ provides an estimate of the dependence of T_N on T , ω_0 and V_Φ .

2.5 SQUIDS at the quantum limit

The above discussion assumes that the SQUID noise is dominated by classical Johnson-Nyquist noise from the shunt resistors. Koch, Van Harlingen and Clarke [67] performed a rigorous calculation of the noise produced in the shunt resistors at $T = 0$, where zero-point fluctuations in the resistors must be taken into account, and found that these quantum fluctuations dominate the SQUID noise. The analysis was performed for a bare SQUID by integrating the equations of motion in the presence of noise. The equations of motion for the system are again given by Eqs. (2.23, 2.24, 2.25 and 2.26), however current noise terms I_{n1} and I_{n2} are added to Eqs. (2.25, 2.26), respectively. The currents $I_{N1,2}$ are the equilibrium noise currents generated in the shunt resistors, each with spectral density $(2h\nu/R) \coth(h\nu/2k_B T)$ where ν is the signal frequency. In the high temperature limit $k_B T \gg h\nu$, the classical expression $4k_B T/R$ is recovered. It was found that the total effective noise spectral density

referred to the input of the SQUID is given by [67]

$$S_V(\nu) = \frac{4\pi\nu R_i}{V_\Phi} (S_V S_J - S_{VJ}^2)^{1/2}. \quad (2.37)$$

An expression for the noise temperature in the quantum regime is composed by adding the SQUID noise in the input circuit $\sim h\nu/2$ to the zero-point fluctuations of the input resistor, $h\nu/2$ [67]. The sum of these two contributions is then set equal to the thermal noise power of the resistor at an effective temperature T_N given by $h\nu/[\exp(h\nu/k_B T_N) - 1]$. The following expression is obtained for the minimum noise temperature allowed by quantum mechanics for any linear amplifier [67]

$$T_N^Q \approx \frac{h\nu}{k_B \ln 2}. \quad (2.38)$$

An important note on convention must be made here. In a paper written by Carlton Caves in 1982 on the quantum limits on noise in linear amplifiers [39], Caves arrives at

$$T_N^Q \approx \frac{h\nu}{k_B \ln 3} \quad (2.39)$$

for the minimum noise temperature allowed by quantum mechanics of any linear amplifier, which appears to be in contradiction with Eq. (2.38). The discrepancy arises from a matter of convention, namely, whether or not to include the half photon of zero-point noise in the expression for the added noise when determining the noise temperature. If it is added to the amplifier noise explicitly one arrives at Eq. (2.38), if it is included in the expression for the amplifier added noise, one arrives at Eq. (2.39). The expression derived by Caves, Eq. (2.39), is the generally accepted expression for the noise temperature of any linear amplifier.

2.6 Applications of the SQUID

In addition to being extremely low noise amplifiers of weak electrical signals, SQUIDS can also be operated as magnetometers and are the most sensitive detectors of magnetic flux. SQUIDS have demonstrated measurements of magnetic fields as small as

5×10^{-18} T, approximately 13 orders of magnitude smaller than Earth's magnetic field [53]. Due to their sensitivity, SQUIDs have numerous applications outside of low temperature physics. In biology SQUIDs are used to non-invasively map brain activity [54], and also to record the weak magnetic fields of the stomach [55]. SQUIDs are also used to track magnetic markers in orally applied drugs as they pass through the intestinal tract [68]. In a clinical setting, SQUIDs are used for magnetic field imaging (MFI) [69] and low-field magnetic resonance imaging (MRI) [70], which is less expensive than typical MRI systems and more compact. Geological studies also use SQUIDs for oil prospecting, mineral exploration, earthquake prediction, and geothermal energy surveying [71]. These applications are becoming more common as SQUID technology continues to develop. The most typical use of SQUIDs is in commercially available magnetic property measurement systems, which are used for nondestructive analysis of the magnetic properties of samples [72]. Turn-key magnetic property management systems can be purchased from several manufacturers and can measure samples at temperatures beyond room temperature. Scanning SQUID microscopes have also been used to detect defects in room temperature samples by monitoring local changes in the electrical properties of the sample [73]. This technique has been used to characterize tantalum inclusions in 30×30 cm niobium sheets used to make superconducting resonators for particle accelerators [74]. Using this technique, tantalum inclusions with volumes as small as 10^{-12} m³ have been detected. For accelerator projects such as TESLA about 400,000 niobium sheets have been tested using this technique [74]. Scanning SQUID microscopy has also been used to study the characteristics of samples at low temperature, such as the distribution of vortices in superconducting films [75].

2.7 Limitations

The fundamental limit on the frequency at which a SQUID amplifier can operate is set by the plasma frequency of the tunnel junctions, which is usually in excess of 100 GHz. There are, however, other mechanisms that limit the frequency of operation of these devices to the radio-frequency band unless the input coil is modified to operate at higher frequency. SQUIDs operated as amplifiers in the way described above have been demonstrated to be good amplifiers for frequencies up to a few hundred MHz [76]. At frequencies beyond the radio-frequency range, stray capacitance between the input coil and SQUID washer dominates the input circuit, shunting high frequency signals through this capacitance directly to the SQUID washer. At higher frequencies, less of the input signal is coupled to the SQUID loop as a flux, and this manifests itself as a reduction in the gain of the device. In order to overcome this limitation, SQUID amplifiers must be redesigned and operated in a different way. A technique to overcome this reduction in gain is to use a resonant transmission-line input circuit. The primary focus of this thesis is the implementation of SQUID amplifiers in the GHz frequency range with substantial gain, and that operate with low noise.

Chapter 3

Low-noise amplification

Due to recent advances in quantum information science, interest in low-noise cryogenic amplification is going through a period of revival. Exotic quantum states of photons in the microwave frequency range can now be produced and the issue of how to amplify the small signals from these photons is of great importance. Ideally, when amplifying the signal from single quanta it is desirable for the amplifier to contribute only the noise due to quantum fluctuations, half of a photon at the measurement frequency. An amplifier contributing only this amount of noise is said to operate at the standard quantum limit. There are several groups working on developing amplifiers that operate at, or near the standard quantum limit. In this chapter, we will highlight some of these different approaches to low-noise amplification.

3.1 The high electron mobility transistor amplifier

Transistor-based amplifiers that rely on silicon as a semiconductor are ubiquitous. They are found everywhere from physics labs to mobile phones. For amplifying small signals, such as those characteristic of quantum information science, room temperature transistor amplifiers are not a practical choice, as the noise they contribute during the process of amplification often exceeds the intrinsic system noise by several

orders of magnitude. The noise temperature of a semiconducting transistor amplifier (typically several hundred to several thousand K) can be reduced by lowering the temperature of the amplifier. But at low temperatures, conventional semiconductors suffer from reduced conductivity, rendering them useless for low-temperature applications. The high electron mobility transistor, however, does not suffer from this problem as it relies on a two-dimensional electron gas for conductivity, which has high electron mobility at cryogenic temperatures. Transistor based amplifiers that rely on two-dimensional electron gases are known as high electron mobility transistor amplifiers, or HEMT amplifiers [77, 78]. HEMT amplifiers are widely used in low temperature physics for amplifying microwave signals at cryogenic temperatures. For amplifying the signals from cavities coupled to superconducting qubits, HEMT amplifiers are commonly used, however the large amount of noise they add to the signal makes them a less-than-ideal choice.

For most applications in quantum information science, HEMT amplifiers are thermalized at a temperature of about 4 K. In the frequency range of interest (several GHz), the noise temperature of these devices is also about 4 K. A modest reduction in noise temperature could be achieved by cooling the amplifier further, however, this is not typically an option. The power dissipated by a HEMT amplifier, roughly 10^3 s of milliwatts, is many times larger than the cooling power of a dilution refrigerator ($\sim 100 \mu\text{W}$ at 100 mK). Therefore, the only practical way to cool a HEMT amplifier is by putting it in contact with a helium bath at approximately 4 K. Although a noise temperature of 4 K is a large improvement from the several hundred Kelvin of room-temperature transistor amplifiers, 4 K corresponds to roughly eight 10 GHz photons added to the signal. This results in a rather small signal-to-noise ratio, requiring long average times to resolve the signal from a single photon. Aside from their high noise temperature, the HEMT amplifiers common to low temperature physics have very attractive properties: gains of greater than 30 dB, bandwidths of several GHz and the amplifier remains linear for a broad range of input signal powers. For this

reason HEMTs are almost always used as a second stage of amplification where the first stage is one of the devices to be discussed in the sections below.

3.2 Parametric amplification

Parametric amplification is a process common to optical systems where a laser of frequency ω_p pumps a nonlinear crystal which results in degenerate downconversion of pump photons to a pair of photons at the signal frequency $\omega_s = \omega_p/2$ for weak input signals. Parametric amplifiers can also be operated in a different manner, resulting in non-degenerate parametric amplification. In this case a single pump photon is downconverted to two photons of different frequency such that $\omega_p = \omega_s + \omega_i$ where ω_i is known as the idler frequency mode. Parametric amplification has been realized at GHz frequencies with superconducting circuits where the nonlinearity being pumped is typically the nonlinear inductance of the Josephson junction. Since the Josephson junction is non-dissipative in its superconducting state, in the ideal case the amplifier should only add a half photon of noise at the measurement frequency, as is required by quantum mechanics. However, in the degenerate case the number of photons of added noise can be less than the standard quantum limit in one signal quadrature.

3.2.1 Josephson parametric amplifier

In the degenerate mode of operation described above, a single pump photon is downconverted to a pair of photons at ω_s providing amplification of the weak signal at frequency ω_s . When operated in this way, the parametric amplifier can produce squeezed photon states, where the noise due to the quantum uncertainty between conjugate variables, say photon number n and phase ϕ ($[n, \phi] = i/2$), can be distributed unevenly between the photons while preserving the uncertainty relation between the variables $\Delta n \Delta \phi \geq 1/4$. For instance, the quantum noise in n can be reduced below its equal-uncertainty value of $1/2$ while enhancing the noise in the phase quadrature

ϕ . When amplifying a signal in the non-degenerate mode, the noise added by the parametric amplifier can be less than the standard quantum limit in one quadrature, while the noise in the conjugate quadrature is enhanced.

One realization of a Josephson parametric amplifier (JPA) consists of a string of 480 SQUIDs constituting the center conductor of a coplanar waveguide resonator. A strong pump tone was sent into a weakly coupled port of the device, while the weak signal was amplified upon reflection of the output port. The device demonstrated a gain of up to 26 dB and an added noise of about one quarter of a photon at the measurement frequency [79] when operated as a degenerate parametric amplifier. Although the bandwidth of the amplifier was only ~ 1 MHz, the operating frequency of the amplifier could be tuned by modulating the flux in the SQUID loops. The phase velocity for signal propagation in the array of SQUIDs could be modulated by applying a flux bias enabling the device to be tuned between 4 and 8 GHz. The device demonstrated squeezing of the vacuum noise by 10 dB in one quadrature [80].

This JPA has impressive gain and noise properties, however, the bandwidth at this high gain is not optimal for measuring the state of a superconducting qubit. Also, the gain of the device compresses by 1 dB at relatively small powers, limiting its use to amplification of very weak signals. The power-handling capability is set by the characteristic energy scale of the nonlinearity that is being pumped. For this device, and many devices like it, the energy scale is the Josephson energy E_J of the junctions and is set by the junction critical current I_0 [81].

3.2.2 Josephson parametric converter

Another realization of parametric amplification employing the nonlinearity of the Josephson junction is the Josephson parametric converter (JPC). The JPC is composed of an array of four Josephson junctions coupled to resonant cavities. The amplifier is operated in the non-degenerate mode where a single pump photon is downconverted to a signal photon and an idler photon. Amplification of a weak sig-

nal was observed while operating this device as a three-wave mixer [82]. The amplifier demonstrated near-quantum-limited amplification, boosting a weak signal by a gain of 23 dB while adding between 1.3 and 2.1 photons of noise to the signal. Like the JPA, this device also suffers from a narrow bandwidth ~ 3 MHz. However, it can be tuned over a small frequency range of about 400 MHz with an applied flux. The 1 dB compression point also depends on the applied flux and was determined to be between 3 and 95 photons.

3.2.3 Kinetic inductance parametric amplifier

Recently, parametric amplification was demonstrated by pumping the nonlinear inductance of a thin superconducting film [81]. Since the nonlinearity being pumped was provided by the kinetic inductance of the superconducting film, no junctions were necessary. This amplifier demonstrated gain in excess of 10 dB in a bandwidth of about 4 GHz centered about 11.5 GHz. The noise added by the amplifier was measured to be 3.4 photons at a signal frequency of 9.4 GHz. This amplifier does not suffer from the same power-handling issues as other parametric amplifier since the energy scale of the nonlinearity that is being pumped, a function of the critical current of a superconducting film, is several times larger than the characteristic energy scale set by the critical current of a Josephson junction. In addition, the bandwidth of the amplifier makes it a practical choice for general amplification of microwave signals. Due to the geometry of this device, it is difficult to fabricate. The gain of the device is proportional to the length of the superconducting trace and to achieve suitable gain, the length of the amplifier must approach 1 m. The difficulty comes in implementing a structure of nearly 1 m in length on a chip that can fit into a cryostat, therefore the lateral dimension of the trace must be small, 35 nm, which pushes the limits of standard lithography. The results presented in [81] are not yet published.

3.2.4 The Josephson bifurcation amplifier

Another amplifier that relies on pumping of the Josephson nonlinearity is the Josephson bifurcation amplifier (JBA) [83], although the implementation is rather different from the JPA and JPC. The JBA consists of a capacitively shunted junction. The plasma frequency $\omega_p(I_0, I_{rf})$ the junction is a function of critical current I_0 and an rf current drive, I_{rf} . When the amplitude of the rf bias is sufficiently large, the change in plasma frequency of the junction for a small modulation in I_0 is large. At high drive powers, the system resonance will bifurcate, producing two stable points of operation which differ in phase. If operated slightly below the bifurcation threshold, a small change in I_0 will result in a large change in the phase of the plasma oscillations, which can be detected with suitable microwave interferometric techniques. The device is typically operated by coupling the input signal as a current to the junction. For a fixed rf drive of sufficient amplitude near the plasma frequency of the junction, the input signal modulates the critical current of the junction, which results in a change in the phase and frequency of the plasma oscillations. The JBA can also be used to perform switching measurements, where it is biased very near its bifurcation point and a small change in the critical current will cause the JBA to switch into its bifurcative state.

3.3 The superconducting low-inductance undulatory galvanometer

A device that is closely related to a SQUID amplifier, but whose signal is coupled to the device as a current instead of a flux, is known as the superconducting low-inductance undulatory galvanometer (SLUG) [84]. The theory of operation of a SLUG is very similar to that of a SQUID, although their geometries are quite different. The SLUG consists of two tunnel junctions in parallel connected by superconducting

traces. Unlike the SQUID, the loop formed in a SLUG is not planar, but formed by two narrow superconducting traces patterned on top of one another with a thin dielectric barrier in between. Contact is made between the traces by the two tunnel junctions, thus the SLUG forms a superconducting loop interrupted by two junctions similar to a SQUID but perpendicular to the plane of the substrate (Fig. 3.1). The

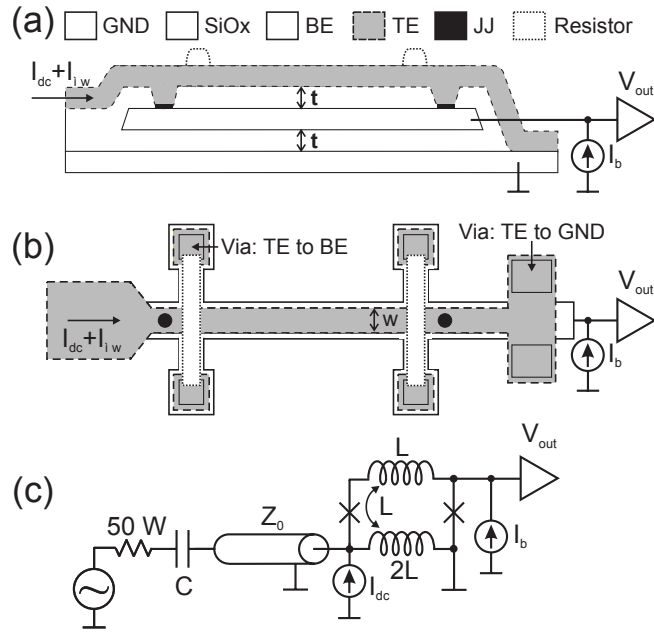


Figure 3.1: (a) Schematic of the SLUG amplifier viewed from the side. Junctions appear solid black. (b) Top view of a SLUG amplifier. (c) Circuit schematic of the SLUG amplifier [85]. Reprinted with permission from D. Hover, Y.-F. Chen, G.J. Ribeill, S. Zhu, and Robert McDermott, *Applied Physics Letters* **100**, 063503 (2012). Copyright 2012, American Institute of Physics.

SLUG also requires two bias parameters to operate, one bias current to bring the device above its critical current, and another bias current to induce a phase difference, analogous to the flux bias of a SQUID. Similar to the SQUID, the SLUG requires resistive shunts to keep the transfer function single-valued and the Johnson-Nyquist noise from these shunts dominates the noise temperature of the device. When the SLUG is biased above the critical current, a change in the phase difference will be transduced to a voltage across the device. The mechanism by which gain is produced in a SLUG is the same as for a SQUID. The SLUG is current biased above its critical

current, and a phase bias sets the operating point to the steepest portion of the V_Φ curve. Signals coupled in as a current are transduced to a voltage across the device.

A SLUG can be used as a microwave amplifier by incorporating it into a microwave resonant circuit. If the SLUG is situated near a standing-wave current antinode of a resonator, resonant current coupled to the SLUG will be amplified. Due to this, SLUGs can be operated at any harmonic which has a current antinode that couples to the device. SLUGS have been studied numerically [84] and experimentally [85]. Experimentally, gains as high as 25 dB have been reported at a frequency of 3 GHz when the device was operated at its first resonant mode. When operated at its second resonant mode, a gain of about 15 dB was observed at nearly 9 GHz. Similar to a SQUID amplifier, the primary source of noise in a SLUG is also Johnson-Nyquist noise produced in the shunt resistors which are required to keep the current-voltage characteristic single valued. Although measured noise temperature data has not yet been reported, the noise properties of SLUGS were studied numerically. The study concluded that these devices are expected to achieve noise performance approaching the standard quantum limit, provided the shunt resistors get sufficiently cold [84].

Chapter 4

The microstrip SQUID amplifier

As discussed earlier, SQUID amplifiers with strongly coupled input circuits suffer from stray capacitance between the input circuit and the SQUID washer as well as between turns of the input coil itself. The operating frequency of conventional dc SQUID amplifiers is limited by this stray capacitance as high frequency signals are shunted directly to ground through the capacitance. In 1998 Michael Mück [86] found that by leaving one end of the input coil unterminated, the stray capacitance in combination with the inductance of the input coil above the ground plane forms a resonant circuit. The resonance frequency of the circuit is set by the coil length. This resonant geometry—with a current carrying line separated from a ground plane by a thin dielectric layer—is known as a microstrip transmission line. This chapter will introduce the concept of the microstrip SQUID amplifier and provide a survey of results over the past decade.

4.1 Stray capacitance — Bug or feature?

Several groups have tried to subvert the problem of stray capacitance between the input coil and SQUID washer by redesigning the input coil and SQUID geometry. In an attempt to reduce the contribution of parasitic capacitance, Tarasov *et al.* [87, 88]

and Propopenko *et al.* [89] fabricated the input coil inside of the SQUID washer (Fig. 4.1). This design resulted in a reduced parasitic capacitance and substantially increased operating frequency. One of their devices demonstrated a gain of 12 dB at a frequency of 4 GHz with a bandwidth of 400 MHz [89]. Although this technique reduced the stray capacitance, devices of this geometry have severely restricted design parameters such as SQUID inductance and input coil geometry. In addition to this, the mutual inductance is much lower compared to the conventional design where the input coil is patterned on top of the washer. In another approach to remove the contribution of the parasitic capacitance entirely, Hibbs *et al.* proposed the input coil be eliminated, and rf signals coupled directly to the SQUID through the bias current line [90]. More recently, another design proposed by Spietz and Aumentado

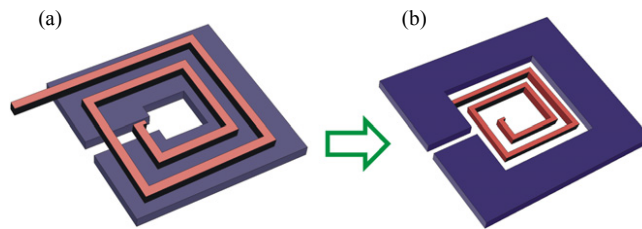


Figure 4.1: (a) Schematic representation of a SQUID amplifier with an input coil patterned on top of a dielectric layer above the SQUID washer. Amplifiers of this geometry suffer from stray capacitance between the input coil and SQUID washer. (b) Schematic of the SQUID geometry used by Tarasov *et al.* [87, 88] and Propopenko *et al.* [89]. The input coil is patterned inside of the SQUID washer to reduce the stray capacitance [91]. (from Mück and McDermott, 2010, p.093001-3)

[92] involved using a small area SQUID in an octupole gradiometer configuration. To counteract the reduced mutual inductance due to the SQUID geometry, an input matching network incorporating a quarter-wave transmission line resonator was used to enhance the current flowing through the input coil, as well as match the SQUID impedance to 50Ω (Fig. 4.2). The amplifier in this configuration was measured and a gain-bandwidth product great than 27 GHz was observed in a frequency range of 4-8 GHz. It is not possible to cite a single value of gain in this case, as the gain varied

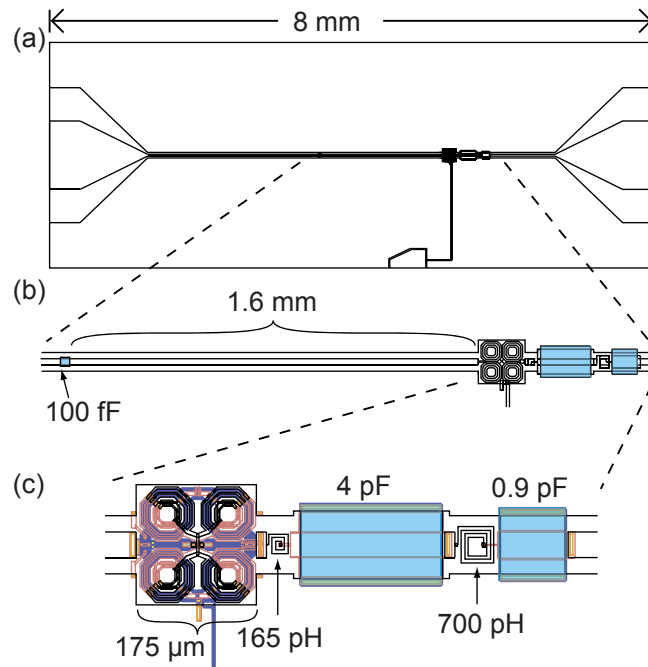


Figure 4.2: Schematic of the amplifier chip at three levels of magnification. (a) Schematic of the amplifier at the chip level. The horizontal structure is a coplanar waveguide resonator. (b) Zoomed in view of the SQUID circuit and 100 fF capacitor that couples the amplifier to the resonant circuit. (c) Further zoomed in schematic of the SQUID and the resonant circuit that transforms the output impedance of the SQUID [92]. Reprinted with permission from L. Spietz, K. Irwin and J. Aumentado, *Applied Physics Letters* **95**, 092505 (2009). Copyright 2009, American Institute of Physics.

by several dB over the broad resonance of the amplifier, therefore gain-bandwidth product is used to characterize the amplifiers performance.

Finally, around 1998 Michael Mück and John Clarke realized that if one end of the SQUID input coil was left unterminated and the SQUID washer was grounded, the input coil and SQUID washer formed a microwave geometry known as a microstrip transmission line resonator. In this geometry the signal is coupled to the SQUID through a $\lambda/2$ microstrip resonator formed by a superconducting spiral input coil patterned on the dielectric layer above the SQUID washer. The resonant frequency of the amplifier is related to the length of the input coil. Devices operated in this way, microstrip SQUID amplifiers (MSA), have shown great promise as low-noise cryogenic

amplifiers of small amplitude microwave signals. Microstrip SQUID amplifier will be discussed in more detail in the sections to follow, and a survey of experimental results of these devices will be presented.

4.2 Microwave resonant circuits

When the physical dimensions of a circuit are small compared to the wavelength of interest, the laws of standard circuit theory apply and Kirchoff's laws can be invoked to determine currents and voltages in a circuit — this is known as the ‘lumped element’ regime. When the circuit dimensions are large compared to the wavelength of the signal, the ‘optical’ regime, electromagnetic fields propagate and can be manipulated with mirrors, polarizers and lenses. However, when the dimension of circuit elements becomes comparable to the wavelength of interest we enter what is known as the ‘distributed’ regime, where a current-carrying circuit element can store energy in electric and magnetic fields simultaneously [93]. In the distributed regime the inductance of wires, combined with their capacitance to a well defined ground in close proximity, form transmission lines through which electromagnetic signals can propagate. A transmission line, such as a coaxial cable can be approximated by a series of inductors with a parallel capacitance to ground (Fig. 4.3) [93]. In the distributed

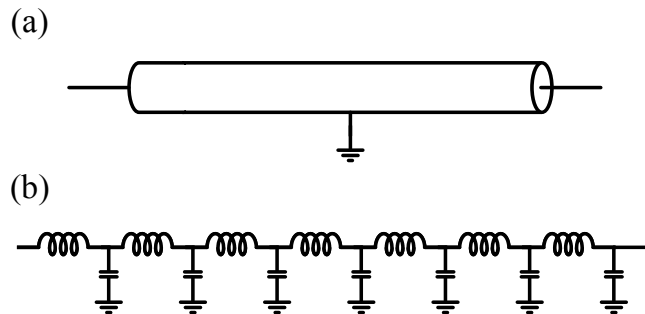


Figure 4.3: (a) Schematic of a coaxial transmission line with the outer conductor grounded. (b) Lumped element approximation of a transmission line

regime, propagating electromagnetic signals in conductors can also exhibit wave-like

behavior, for instance signals can be reflected off of an abrupt change in impedance. Transmission lines with particular boundary conditions form microwave resonant circuits, where the current of signals on resonance is enhanced by the quality factor Q of the resonator. There are several different planar geometries which behave as transmission lines, in the following section the microstrip transmission line, and the coplanar wave guide geometries will be discussed [93].

4.2.1 Transmission lines and resonators

The microstrip transmission line is composed of a conducting strip of width w separated from a ground plane by a dielectric layer of thickness h . A superconducting transmission line of infinite length has an inductance per unit length and capacitance per unit length given by

$$L_0 = \frac{\mu_0 h}{w} \left(1 + \frac{2\lambda}{h} \right) \quad (4.1)$$

$$C_0 = \frac{\epsilon \epsilon_0 w}{h} \quad (4.2)$$

where $\mu_0 \equiv 4\pi \times 10^{-7}$ H/m, $\epsilon_0 \equiv 8.85 \times 10^{-12}$ F/m, λ is the penetration depth of the superconductor and ϵ is the relative permittivity constant of the dielectric material [43]. The microstrip line, with characteristic impedance $Z_0 = \sqrt{L_0/C_0}$, provides broadband transmission of electromagnetic waves with a propagation velocity

$$\bar{c} = \frac{1}{\sqrt{L_0 C_0}}. \quad (4.3)$$

A resonant structure can be formed by imposing zero-voltage or zero-current boundary conditions at either end of the microstrip line by either shorting the microstrip to ground, or leaving the microstrip unterminated. Leaving both ends unterminated ($Z_L \gg Z_0$) forms a half wave ($\lambda/2$) resonator, where at either end of the resonator nodes in the current density (and antinodes in the voltage) accommodate a half-wavelength standing wave resonance. In contrast to imposing $Z_L \gg Z_0$ boundary

conditions at both ends of the resonator, when one end is grounded ($Z_L \ll Z_0$) and the other is left unterminated ($Z_L \gg Z_0$) a quarter wave ($\lambda/4$) resonator is formed [94]. In a quarter wave resonator, the grounded end of the resonator has a voltage node (and a current antinode), and the unterminated end has a current node (and a voltage antinode), accommodating a $1/4$ wavelength standing wave resonance. We are most interested in the case of leaving both ends unterminated forming a $\lambda/2$ resonator as this will serve as the input coil for our microstrip SQUID amplifiers. The resonant frequency of a half-wave microstrip resonator scales as the resonators length

$$f_{\lambda/2} = \frac{1}{4\pi l \sqrt{L_0 C_0}} \quad (4.4)$$

Another microwave transmission line that is commonly employed in microwave superconducting thin-film devices is the coplanar waveguide (CPW). The coplanar waveguide is composed of a conducting strip with ground plane on either side of the strip on top of a common dielectric. The impedance is related to the width of the centerline and the distance between the center line and the ground plane, therefore CPWs are often used as impedance transformers. Signals are carried to and from our microstrip SQUID amplifier on chip using coplanar waveguides. The CPW tapers from several mm in width to about $100 \mu\text{m}$ while maintaining constant impedance. The CPW-to-microstrip line transition occurs at a coupling capacitor, therefore this transition must be designed with great care to preserve the impedance of the input circuit. An impedance mismatch at this point would cause reflection of signals incident on the SQUID input circuit resulting in a reduction of gain. In addition to defining the length of the input coil, the coupling capacitor also impacts the quality factor Q of the input coil resonance. The quality factor of a loaded resonant circuit can be expressed as

$$\frac{1}{Q} = \frac{1}{Q_c} + \frac{1}{Q_i} \quad (4.5)$$

where Q_c is the coupling quality factor and Q_i is the intrinsic quality factor of the resonator [95]. The Q_i for our input coil circuit is most likely limited by dissipation

from the shunts in the SQUID being reflected back into the input circuit. Another contribution to Q_i comes from loss in the dielectric layer. In the case of our amplifiers, this dielectric is PECVD deposited SiO_2 which is very lossy compared to single crystal dielectrics that high- Q resonators are typically fabricated on. For any amplifier with a tuned input circuit, the quality factor of the input circuit is intimately related to the overall performance of the amplifier, as it is related to both the gain and bandwidth. An input circuit with a high- Q will produce a narrow resonance with a large peak height in gain, where as a low- Q circuit will produce a broader resonance with a small gain peak height. In terms of amplifier performance, a high- Q circuit will result in substantial gain over a very narrow bandwidth and a low- Q input circuit will have less gain but over a broader band. In theory, for a particular amplifier, the product of gain and bandwidth is constant due to conservation of energy. However in practice this is often not the case due to feedback effects from stray capacitance and inductance or other mechanisms of loss.

Often, high- Q circuits are desirable due to greater stability and their propensity to reject unwanted frequencies. For high- Q applications, resonant circuits are fabricated on single crystal dielectric substrates such as sapphire or intrinsic silicon which provide a high intrinsic quality factor. Using a high loss dielectric like PECVD SiO_2 is suitable for our application because a wide bandwidth is desired. PECVD SiO_2 is also straightforward to deposit, pattern and etch. Integrating a high quality dielectric into our devices, in place of the SiO_2 , would require re-engineering the fabrication procedure to accommodate the conditions required for high quality dielectric deposition. For our devices there is no benefit to using a low-loss dielectric. According to Eqn. (4.5), the measured quality factor of a circuit depends not only on the intrinsic quality factor Q_i but also the coupling quality factor Q_c . This determines how strongly coupled the resonator is to external circuitry and is set by the value of the coupling capacitor. By changing the value of the coupling capacitor, the measured quality factor of the circuit, Q , can be reduced from its maximum value of $Q = Q_i$. Kinion

and Clarke studied the dependence of amplifier performance on coupling. They found that maximum gain was achieved when the resonant circuit was critically coupled to 50Ω (Fig. 4.4) [96].

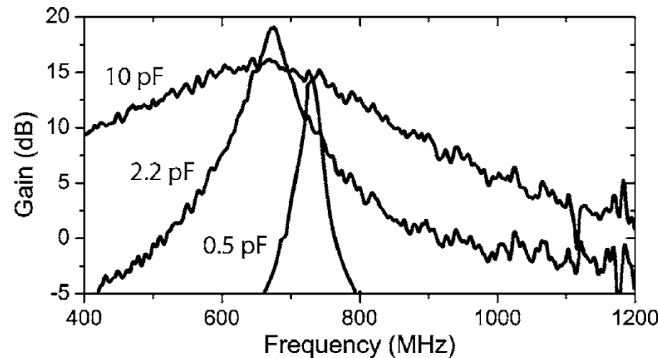


Figure 4.4: Gain vs. frequency for three different values of coupling capacitance: 0.5 pF, 2.2 pF and 10 pF. These three values of coupling capacitance correspond to regimes where the input coil is undercoupled (0.5 pF), approximately critically coupled (2.2 pF), and overcoupled (10 pF), respectively [96]. Reprinted with permission from D. Kinion and J. Clarke, *Applied Physics Letters* **92**, 172503 (2008). Copyright 2008, American Institute of Physics.

4.3 The microstrip SQUID amplifier — early measurements

Results from various groups are presented below. Although the specific design of each of the devices discussed varies between research groups, most of the MSAs below have a few things in common. The components of the SQUID, including the junctions, employ niobium as the superconducting material. Niobium is a convenient choice, due to its high superconducting transition temperature and its large superconducting gap parameter. The transition temperature for niobium is ideally 9.3 K, therefore niobium devices can be measured far below their transition temperature using only a helium bath at 4.2 K. The superconducting gap parameter sets a limit on the maximum critical current density for a junction. For a material with a large gap parameter, a

junction with a suitable critical current can be fabricated photolithographically with an area of $\sim 1 \mu\text{m}^2$. On the other hand, the junction capacitance associated with this area limits the value of the shunt resistance used to keep the SQUID single-valued, which limits the gain of the devices. In order to enhance the gain, a hole is used in the SQUID washer to boost the mutual inductance between the input coil and SQUID washer (Fig. 4.5).

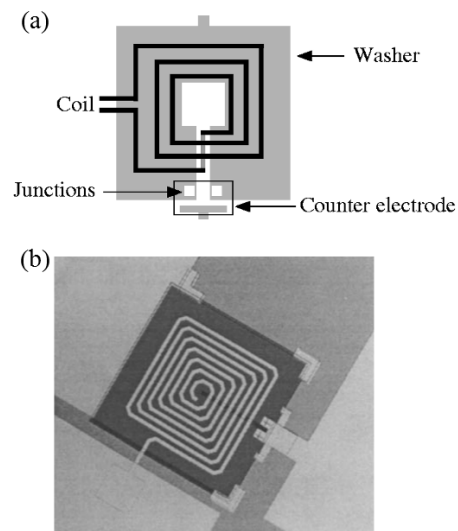


Figure 4.5: (a) Schematic of an older style MSA with a hole in the SQUID washer to enhance the mutual inductance. (b) Optical micrograph of an older style MSA [97]. Reprinted with permission from M. Mück, C. Welzel, and J. Clarke, *Applied Physics Letters* **82**, 3266 (2003). Copyright 2003, American Institute of Physics.

4.3.1 Gain

As discussed earlier in chapter 2, dc SQUID amplifiers are well-understood circuits which transduce a flux signal threading the SQUID washer to a voltage across the SQUID. The signal is typically a current driven between two ends of an input coil inductively coupled to the SQUID washer. Although these devices are good amplifiers up to ~ 100 MHz, beyond this frequency range stray capacitance between the input coil and SQUID washer provides a low impedance path to ground, shunting high frequency signals and limiting the operating frequency. The integration of the microstrip resonant circuit to the SQUID amplifier results in a SQUID amplifier with an operating frequency set by the length of the input coil known as a microstrip SQUID amplifier (MSA). The coupling between resonant input coil transmission line and the SQUID washer is illustrated in Fig. 4.6.

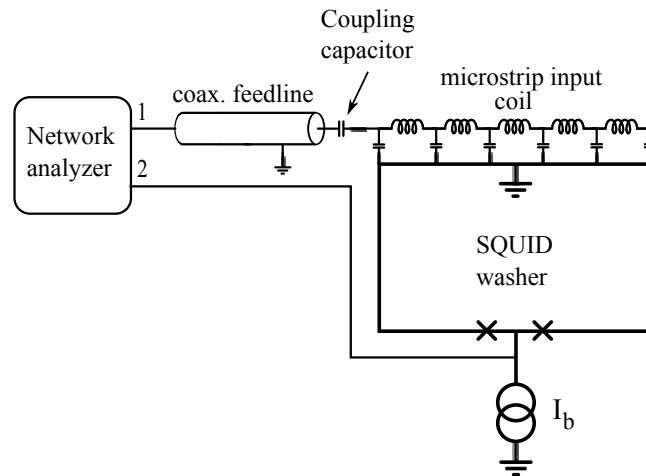


Figure 4.6: Schematic of the coupling between the input resonant microstrip circuit to the SQUID washer. The network analyzer illustrates where the voltage is measured when performing a transmission measurement of S_{21} .

Although there is not a detailed model for the gain of an MSA, an approximate expression for the gain can be constructed. The gain of a MSA is proportional to the power gain of a conventional, low-frequency SQUID amplifier $G \propto M_i^2 V_\Phi^2$, however the current in the microstrip input coil is enhanced by the quality factor Q of the

SQUID		l	w	f_0	G	Δf	T_N
No.	n	(mm)	(μm)	(GHz)	(dB)	(GHz)	(K)
1	13	7.6	5	2.2	12 ± 1	0.50	1.3 ± 0.8
2	11	5.5	5	3.2	11 ± 1	0.55	1.5 ± 1.0
3	7	4.5	10	4	10 ± 1	0.30	1.8 ± 1.5
4	4	3.5	20	5	9 ± 1	0.32	...
5	3	2.3	20	7.4	6 ± 1	0.85	...

Table 4.1: Parameters for five MSAs of different input coil lengths [97]. (from Mück *et al.*, 2003, p.3267)

input circuit resonance when the circuit is driven at its resonance frequency

$$G \propto M_i^2 V_{\Phi}^2 Q^2. \quad (4.6)$$

The first measurements of MSAs demonstrated gains of approximately 18 dB and operating frequencies in the range of 200-600 MHz [86]. Several devices of different input coil lengths were fabricated and measured. One would expect a reduction in gain at higher frequencies since shorter input coils have a smaller mutual inductance M_i , however reduction in the gain was not observed. The authors note that the reduction in gain was mitigated by the increased quality factor Q of the higher frequency input circuits.

In a later study, MSAs that operated at higher frequencies were fabricated and measured [97]. A series of 5 MSAs (Table 4.1) with operating frequencies between 2.2 GHz and 7.4 GHz were measured. A substantial reduction in gain was observed as the frequency of operation was increased (12 dB at 2.2 GHz and only 6 dB at 7.4 GHz). In light of this result it is clear that the microstrip SQUID amplifier must be redesigned in order to overcome this loss of gain.

Because the gain of an MSA is proportional to $M_i^2 V_{\Phi}^2$, a clear route to preserving

the gain of an MSA with the reduced M_i that results from shorter-higher-frequency input coils is to enhance V_Φ . A technique to enhance V_Φ is by decreasing the area of the junction, which will result in a smaller junction capacitance. With a smaller capacitance, larger shunt resistors can be used, which will enhance V_Φ while still keeping the SQUID current-voltage characteristic single valued.

4.3.2 Noise properties

In previous chapters a discussion of the noise properties of a SQUID amplifier was presented. The primary contribution to the noise of a SQUID amplifier is Johnson-Nyquist noise produced by the resistive shunts. As discussed in chapter 2, noise from the shunts results in a voltage noise S_V a current noise S_J and a correlated voltage-current noise S_{VJ} . It can be shown that the optimum noise temperature of a SQUID amplifier is given by [56]

$$T_N^{opt} \propto \alpha T \omega_0 / V_\Phi \quad (4.7)$$

where ω_0 is the signal frequency, T is the bath temperature and $\alpha \approx 7$ for a weakly coupled SQUID.

Several groups have reported noise temperature data for SQUID amplifiers. Hilbert and Clarke reported a noise temperature of about 4 K for a SQUID operating at 100 MHz with a gain of about $G = 19$ dB [56] when operated in a liquid helium bath at $T = 4.2$ K. When the bath temperature was reduced to 1 K, the noise temperature was measured to be $T_N = 1$ K. Takami *et al.* reported a noise temperature of $T_N = 0.7$ K for a SQUID amplifier operating at 150 MHz with a gain of $G = 20$ dB in a helium bath at $T = 4.2$ K [98]. Prokopenko *et al.* measured a noise temperature of $T_N = 4$ K for a SQUID amplifier operating at 3.6 GHz with a gain of 20 dB [89], and in a later work reported a noise temperature of 2 K for a SQUID amplifier operating at 4 GHz with a gain of 12 dB [99]. Both of these measurements were performed in a helium bath at 4.2 K. A more detailed discussion of techniques to measure noise temperature of low-noise amplifiers is presented in chapter 8.

Noise temperature measurements of early MSAs, with the standard square washer hole geometry and employing large area Nb trilayer junctions, have been reported by many groups. In the microstrip SQUID amplifier configuration, Mück *et al.* measured noise temperatures of about 0.8 K at 80 MHz and 1.6 K at 3 GHz with gains of 25 dB [86] and 11 dB [97] for a bath temperature of 4.2 K. Andrè *et al.* [100] reported $T_N = 0.1$ K at 90 MHz for an MSA with gain of 20 dB and a $T_N = 0.12$ at 440 MHz with a gain of about 16 dB. Both of these measurements were performed at a bath temperature of 0.4 K. Mück *et al.* measured at $T_N = 0.05$ K at 500 MHz at a bath temperature of 20 mK [101]. More recently Kinion observed a $T_N = 0.05$ K at a higher frequency, 650 MHz and a bath temperature of .045 K [102]. The 1/2 photon that corresponds to the quantum limit at 500 MHz contributes 12 mK to the noise temperature, which was within the error bars of the above measurements — therefore the noise due to zero-point fluctuations was taken into account in the analysis.

4.3.3 Other configurations

Other modifications have been made to SQUID amplifiers in order to increase their gain and bandwidth. A common method to enhance gain is to cascade two or more SQUID amplifiers. In this case the power gain is proportional to the sum of the individual power gains of each of the amplifiers. This technique was demonstrated with SQUID amplifiers at 4 GHz by Prokopenko *et al.* [99]. A net gain for the system of two, nominally identical SQUID amplifiers was measured to be about 18 dB, where the amplification of a single stage was measured to be only 10 dB. In practice, cascading MSAs is not easy. Directional isolation or filtering is required between the two device to prevent the Josephson oscillations of the second MSA from interfering with the first. Also, great care must be taken to match the impedance of the output of the first MSA to the input impedance of the second MSA. SQUID amplifiers tend to suffer from poorly matched input and output impedances. This occurs primarily due to the presence of the SQUID modifying the dynamic impedance

of the input circuit. Capacitive feedback of the output signal of a SQUID amplifier has been used to modify the gain and impedance of the device [56]. Mück *et al.* measured the effect of capacitive feedback on the input impedance of MSAs [103] and found that negative feedback improved the input impedance of the amplifier, making it a better match to the $50\ \Omega$ environment. Although the net gain of the amplifier is reduced due to negative feedback, this technique provides a more robust way for matching impedances when cascading several MSAs.

For our measurements of MSAs—which will be presented in chapter 6—the MSA was operated with the SQUID washer grounded and the counter electrode (where the voltage is measured) left floating. However, there are some circumstances where it is advantageous to ground the counter electrode and measure the signal voltage at the SQUID washer. When the counter electrode is grounded, the SQUID washer is at the output potential. The output signal is feedback to the input coil through the native capacitive coupling between the coil and washer. The sign of the feedback can be changed *in situ* by biasing the SQUID such that the sign of V_Φ is either the same as the input signal (positive feedback), or different (negative feedback). As discussed in the previous paragraph there are some advantages to operating an MSA with capacitive feedback including improved impedance matching. Mück and Clarke presented a model for the behavior of the MSA with and without feedback [104] that was in good agreement with measured results. In the same paper, Mück and Clarke propose a technique to induce inductive feedback while grounding the washer. The current flowing through an inductor connecting the SQUID washer to ground—such as a wirebond—will develop a voltage across it, and hence on the washer. This voltage, which is proportional to the output signal, will feedback to the input coil through the native capacitance between the input coil and washer. In addition to increasing the operating frequency of the MSA from 250 MHz to 300 MHz, the gain of the device was also increased by 3 dB for optimum positive inductive feedback. A comparable reduction in the operating frequency and gain was observed under

the same conditions but when the sign of the feedback was negative. Finally, in an analysis of the stability of MSAs under different bias conditions, Kinion and Clarke found that MSAs are conditionally stable amplifiers [105]. The stability of an MSA can be improved by introducing negative feedback, which comes at the expense of gain.

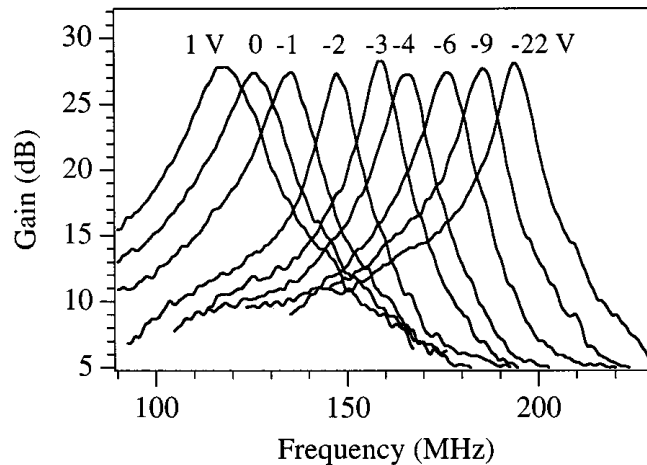


Figure 4.7: Gain vs. frequency for a microstrip SQUID amplifier for several different voltages across a varactor diode at unterminated end of input coil [106]. Reprinted with permission from M. Mück, M.-O. André, J. Clarke, J. Gail, and C. Heiden, *Applied Physics Letters* **75**, 3545 (1999). Copyright 1999, American Institute of Physics.

High bandwidth is beneficial for any amplifier, however this can be difficult to achieve with an amplifier that relies on a resonant input circuit. A fixed resonance frequency and narrow bandwidth limits the versatility of the amplifier, restricting the range in frequency of its input signals. The ability to tune the resonance frequency of an amplifier can make up for low bandwidth. The operating frequency of microstrip SQUID amplifiers can be tuned *in situ* by placing a varactor diode at the unterminated end of the input coil. A varactor diode is a specially constructed diode that functions as a tunable capacitance when a voltage is applied to one of its terminals. Varactor diode chips can be purchased off the shelf and integrated into an MSA by carrying the unterminated end of the coil off the MSA chip with wirebonds and terminating it at the input of the diode. Modifying the capacitance of the mi-

crostrip resonator changes the electrical length of the standing wave mode, therefore the resonant frequency can be tuned to some degree. This technique was realized by Mück *et al.* [106]. Gain versus frequency for the MSA is shown in Fig. 4.7 for several different voltages across the varactor diode. Despite the success of this technique at low frequencies, stray capacitance and inductance would make this technique difficult to implement at GHz frequencies. In the same reference, the two techniques of cascading and tuning were combined. When the two MSA were tuned to the same frequency the cascaded system yielded a gain of 33 dB. However, the SQUIDs could be slightly detuned which resulted in a lower gain, 23 dB, but substantially increased the bandwidth of the cascaded system.

Chapter 5

Device Fabrication

In this chapter we describe the techniques used to fabricate our devices. Fabrication is performed at the Cornell Nanoscale Science and Technology Facility (CNF), and at our own facilities in Syracuse University. The CNF is a subsidized user fabrication facility that provides access to a variety of tools used for nanofabrication. The fabrication procedure of the MSAs and the SQUID oscillators is identical although the patterns are different. The devices consist of a stack of metals (resistive and superconducting) and a dielectric layer to prevent conduction between metallic layers and to provide capacitance where necessary. Metals are deposited with electron beam evaporation, and dielectrics are deposited with plasma enhanced chemical vapor deposition. All metallic layers, except for the Josephson junctions are patterned photolithographically, and lifted-off, whereas dielectric layers are etched. As a final step the Josephson junctions are patterned with electron beam lithography and formed by double-angle evaporation.

5.1 Substrate preparation - MOS processing

For microstrip SQUID amplifiers and SQUID oscillators, 100 mm doped silicon wafers are used as a substrate. These devices do not rely on conduction through the substrate

so the degree to which a wafer is doped and the type of doping is not important. The resistivity of the wafers typically used is between 10 and 25 Ω cm. Prior to depositing any material on the silicon wafers the surface is first oxidized. The oxide layer prevents charge from being carried through the substrate, providing electrical isolation between features in contact with the substrate. Prior to oxidation, which takes place in a metal-oxide-semiconductor (MOS) processing furnace, the wafers must be cleaned to prevent contamination of the furnace. The procedure used, known as MOS cleaning or RCA (Radio Corporation of America) cleaning, removes trace amounts of organics, oxides and metals present on the surface of the wafer that may contaminate the MOS furnace [107]. The RCA cleaning procedure requires the wafers to be treated in a bath of $\text{H}_2\text{O} - \text{NH}_4\text{OH} - \text{H}_2\text{O}_2$ (5:1:1 by volume) heated to a temperature of 75° C for 10 minutes, followed by a rinse in deionized water until the resistivity of the water reaches 13 M Ω cm. The wafers are then treated for 10 minutes in a bath of $\text{H}_2\text{O} - \text{HCL} - \text{H}_2\text{O}_2$ (6:1:1 by volume) at a temperature of 75° C for 10 minutes followed again by a 10 minute rinse in deionized water until the resistivity of the water exceeds 13 M Ω cm. Wafers are now ready for metal-oxide-semiconductor (MOS) furnace processing. If wafers are not processed within 8 hours of cleaning, they must be cleaned again. Bath chemistry should be refreshed every 4 hours by adding 1 part H_2O_2 .

Wafers are oxidized one cassette at a time (25 wafers) in a MOS oxide furnace at a temperature of 1000° C in the presence of H_2O for 9 minutes, then annealed at the same temperature for 20 minutes. During furnace processing the first 90 nm of the silicon surface becomes oxidized, making the wafers suitable substrates for our superconducting circuits.

5.2 Photolithography

Photolithography is a technique used to pattern integrated circuits. To perform photolithography a photosensitive polymer solution, photoresist, is spun onto the wafer to form a uniform film. The film is hardened by baking the wafer on a hot plate, driving off the solvent in the resist. A photomask of the desired pattern is put between a UV light source and the wafer so light can pass through the photomask, transferring the pattern to the photoresist on the wafer. When the photoresist is exposed to UV light, the photosensitive chemical becomes slightly acidic and can be removed by soaking the wafer in a basic solution. This process is known as development and after developing a wafer the exposed photoresist is removed and unexposed photoresist remains on the wafer.

Several steps in our fabrication procedure involve photolithography. The procedure will be described only once in this section. Photolithography is performed on an ASML 300c deep-ultraviolet stepper at the CNF. This tool was state of the art in the 1990's and it offers less than 250 nm resolution, limited by the wavelength of the light source (248 nm), and an impressive 2 nm overlay of aligned layers. A two-layer stack of photoresist is used. The first layer (DSK-312) is a thin coating that prevents the UV light from reflecting off the substrate surface and double-exposing the resist. This chemical and many like it are known as anti-reflective coating (ARC). DSK is spun at 3000 RPM and subsequently baked at 185° C for 90 s. Prior to baking, resist is removed from the backside of the wafer with acetone and a swab. DSK-312 is not photosensitive, but dissolves in basic photoresist developer (AZ 726 MIF). Photoresist (UV210-0.6) is spun on top of the DSK at 3000 RPM and is baked at 135° C for 60s. The wafers are now ready to be exposed on the ASML stepper. Wafers are exposed at 20 mJ/cm² of deep-ultraviolet light with the focal plane 0.2 μm into the top surface of the resist. The exposed wafer is then baked for 90 s at 135° C and subsequently developed for 120 s in a basic developer, typically 726 MIF. This technique is used to pattern all metallic and dielectric layers of the device except for the tunnel junctions,

which are patterned using electron beam lithography.

5.3 Metal and dielectric deposition

5.3.1 Resistive shunts

There are two techniques for producing a patterned metallic layer on a wafer. One approach is to deposit metal uniformly across the bare wafer, then perform negative-tone photolithography, such that the desired pattern remains in photoresist on the wafer. The wafer is then etched in a wet chemistry or with reactive-ion etching. Reactive-ion etching relies on the production of a chemically reactive species by ionizing an inert gas in an rf field. The chemistry reacts with the metal film, producing a volatile byproduct which diffuses into the plasma [107]. Once the etch is complete the remaining photoresist is removed and the metal that was protected by photoresist remains on the wafer. Reactive ion etching is commonly used to etch away the metallic layers. One disadvantage to this technique is that often the etch chemistry will also etch the substrate once the metal has been removed, resulting in an over-etched pattern. Also, the photoresist etches quickly in most etch chemistries, so care must be taken to ensure that the protective layer of photoresist is not etched away.

The other technique is known as liftoff processing. To perform liftoff, a bare wafer is patterned with positive photolithography, such that the area to be metallized is developed away and the photoresist remains wherever metal is not desired. Metal is then deposited on the wafer. After deposition of metal, the wafer is soaked in a solvent that dissolves the photoresist. The metal that was deposited on top of the photoresist lifts off of the wafer, leaving the desired pattern behind. The choice of technique depends on the application. For our devices lift-off processing is favored for metallization. Etching is more commonly used for patterning dielectric layers due to the difficulty in lifting off a thin dielectric film.

The conducting layers of our devices consist of three different metals, titanium

and palladium for resistive shunts, and aluminum for superconducting components. Resistive shunts require a 2-metal stack of titanium and palladium. A thin layer of titanium (~ 2 nm) is used only to promote adhesion of the palladium film that will serve as the resistive metal. Without the thin titanium layer the palladium would not adhere well to the substrate due to different growth kinetics of the films. The evaporation of titanium and palladium are performed at the CNF in the general-use electron beam evaporators.

After photolithographically patterning the wafer, but prior to metalization, the wafers are cleaned in a light oxygen plasma at 150 Watts for 30 s to remove any trace organics that may be left behind from the resist. This descumming process is essential for good film adhesion. Wafers are loaded into the vacuum space of the evaporator and after a sufficient pressure is achieved, a thin ($\sim 1-2$ nm) film of titanium is deposited using electron beam evaporation. During the titanium deposition, it is important to not allow for the formation of a continuous film as titanium is superconducting at low temperatures, however, the film must be thick enough to provide sufficient adhesion for the palladium. Depositing at $1-2 \text{ \AA/s}$ allows sufficient control over film thickness to reliably deposit $\sim 1-2$ nm thick films. Without breaking vacuum, 20 nm of palladium is deposited onto the titanium adhesion layer at 2 \AA/s . Once the deposition is complete the wafers are removed from the evaporator and the resist layer is dissolved in an agitated bath of remover 1165 heated to 80° C until the wafer is free of the metal/resist layer. The ARC and other organics are ashed away in an oxygen plasma at 250 W for 3 minutes.

5.3.2 SQUID washer and counterelectrode

The photolithographic recipe described above is repeated for the first superconducting layer of the SQUID, the SQUID washer and the counterelectrode. The superconducting properties of thin aluminum films are very sensitive to the film quality, which can be degraded if the film is deposited in the presence of impurities. Therefore it

is important to deposit the film in a high vacuum, contamination free deposition chamber. For this reason, aluminum depositions are performed in our own custom electron beam evaporator at Syracuse University. Our evaporator is dedicated for aluminum deposition, therefore contamination from resistive or magnetic materials is not a problem. The deposition chamber can achieve a base pressure 3 orders of magnitude lower than the general-use evaporators at the CNF. This allows us to produce high quality superconducting films.

After patterning the groundplane layer with photolithography and developing the pattern, the wafers are brought back to Syracuse University where aluminum is deposited at $\sim 10 \text{ \AA/s}$ to a film thickness of 80 nm. The aluminium/resist layer is lifted off in an acetone bath heated to 75° C until the wafer is free of the metal/resist layer. Brief sonication can be used hasten the process, or aid in the removal of resist/metal from small features. Once removed from the acetone bath, the wafer are be submerged in, or drenched with isopropanol to inhibit the acetone/resist mixture from drying on the wafer. The wafer is then dried with nitrogen gas. Failure to properly drench the wafer with isopropanol will result in metal and resist being redeposited on the wafer that cannot be removed. As a final step in the process the wafer is ashed as described above to remove the DSK and other remaining organics.

5.3.3 Dielectric deposition

With the palladium shunt resistors and aluminum SQUID washer now on the wafer, a dielectric layer is deposited to provide electrical isolation between the SQUID washer and subsequent metallic layers. Silicon dioxide (SiO_2) was chosen due to ease of deposition and etching. The SiO_2 is deposited using plasma enhanced chemical vapor deposition (PECVD). In this process two or more gases are combined in the presence of an ionizing rf field. The ionized gases recombine on the surface of the RF electrode. A wafer is placed on the electrode during the deposition, and the deposition rate is set by the flow rate of the gas the rf power and the temperature of the electrode.

The recipe we use to deposit SiO_2 films uses a combination silane gas with nitrous oxide ($\text{SiH}_4 + \text{N}_2\text{O}$). In the presence of an rf field the gases ionize and recombine on the wafer as SiO_2 . In order to reduce the stress of the film, the wafer is heated to 200°C . The nominal SiO_2 thickness for our MSAs is 150 nm, which is usually deposited in about 45 seconds. After a film has been deposited on the wafer, the wafer is patterned with negative-tone photolithography. The film is then etched in an Oxford-80 reactive-ion etcher at the CNF. The areas that were exposed and SiO_2 remains in areas that were not exposed. The etching is performed in a plasma of CF_4 for about 5 minutes. After etching, the resist is stripped in remover 1165 and subsequently ashed as in previous steps.

As a final photolithographic step, the input coil is patterned on top of the dielectric layer, and aluminum is deposited in an identical way to the steps above. Once the metal/resist layer is lifted off and the remaining organics are removed by ashing, the wafer is ready for patterning of the Josephson junctions that are patterned with electron-beam lithography.

5.4 Electron beam lithography

Electron beam lithography is used to pattern the Josephson junctions since the minimum feature size of the junctions are smaller than the available wavelength of light for conventional photolithographic techniques. Electron beam lithography is similar to photolithography in the sense that it relies on the chemistry of a polymer solution changing upon exposure energy (photons, or electrons). The resists we used for electron beam lithography are conventional plastics, polymethyl methacrylate (PMMA) and methyl methacrylate (MMA-MAA copolymer). When exposed to a high energy electron beam, the polymers of the resist become de-cross-linked and can be selectively removed with a developer solution.

In addition to increased resolution, electron beam lithography poses another ad-

vantage over photolithography. With photolithography the entire pattern is transferred from the photomask to the resist in a single ‘flash’ so an entire die is patterned at once, and the pattern is usually identical for each die on the wafer. In electron beam lithography a 2 nm diameter electron beam is raster scanned over the pattern area, and this is repeated for each die on the wafer. Due to this, several different patterns can be written on the same wafer without incurring the cost of additional photomasks, making e-beam lithography an effective prototyping tool. One disadvantage of electron beam lithography is it can be time consuming if the pattern area is large. For example, to expose the entire area of a 100 mm wafer (which would be an *extraordinary* waste of time and money) with a 2 nm spot size and a 50 MHz shutter speed, it would take more than 1.5 years. The same exposure is routinely performed with photolithography in a single exposure.

5.4.1 Shadow evaporation

In the simplest terms, a Josephson junction is a superconducting trace interrupted by a small dielectric barrier. The tunnel barrier that provides this interruption should be sufficiently thin to allow tunneling across the barrier, hence the wavefunctions on either side of the tunnel barrier should overlap. There are many realizations of Josephson junctions, for our devices a superconductor-insulator-superconductor geometry is used. Both of the superconducting electrodes are aluminum and the tunnel barrier is aluminum oxide forming a small, thin barrier parallel plate capacitor-like geometry. The junction is formed by depositing the bottom aluminum electrode and subsequently exposing it to a mixture of argon and oxygen at a well controlled pressure and duration. The top electrode is then deposited forming the junction.

Double angle evaporation is used to form the junctions [108]. The resist mask for a junction contains an airbridge, a small bridge of resist suspended over an open channel. In the absence of the airbridge, a metal deposition would yield only a straight metallic trace. If we were to deposit metal into a resist mask with an airbridge and the

deposition angle normal to the resist surface, a broken superconducting trace would result. Neither of the scenarios would result in a useful tunnel junction. The tunnel junction is formed by evaporating at two angles symmetric about the direction normal to the resist with an oxidation step between the evaporations. This technique, known as double angle evaporation, is commonly used to form sub-micron Josephson tunnel junctions. Lithography is, in most cases, a binary process. Resist is either exposed

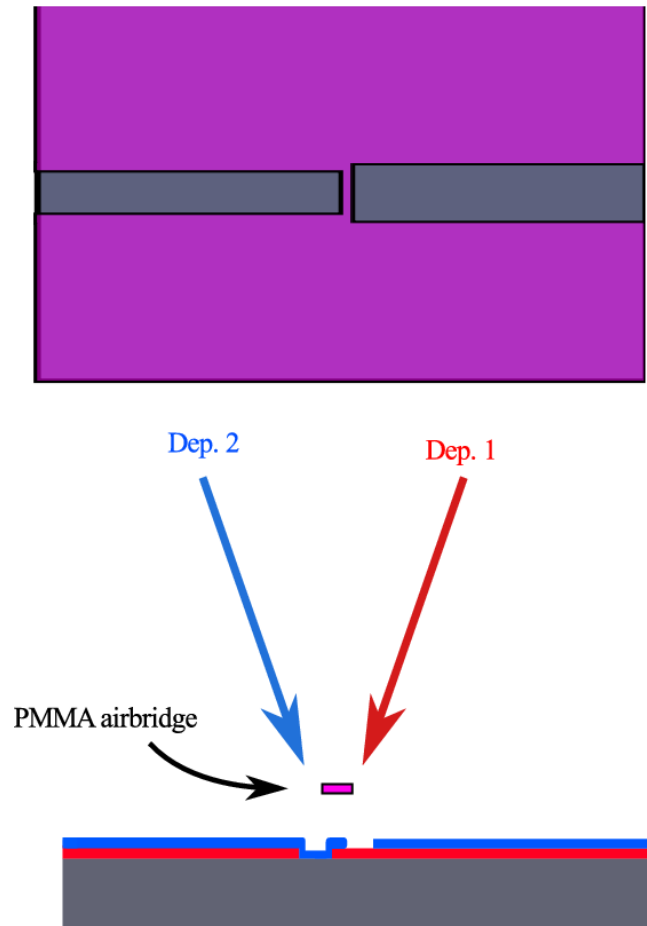


Figure 5.1: (a) Top-view schematic of resist mask after development of exposed electron beam resist. Magenta layer represents the resist mask and dark grey areas represent areas where the substrate is exposed. (b) Cross-sectional view of the same resist mask illustrating the airbridge. Deposition angles are illustrated by red and blue arrows. The tunnel junction is formed below the airbridge where red and blue layers overlap.

and removed, or unexposed and remains on the wafer, therefore special techniques

need to be used to form the air-bridge structure that leave a narrow section of resist suspended, while exposing the resist beneath it. To achieve this, two layers of resist are used. The first layer is 700 nm of MMA-MAA copolymer that is spun onto the wafer at 2500 RPM and baked at 170° C for 10 minutes. A layer of PMMA is then spun at 3000 rpm and baked at 170° for another 10 minutes. The sensitivity of the MMA is much higher than PMMA, therefore it takes greater dose to expose the PMMA versus the MMA. The dose used to expose the pattern is sufficient to clear the PMMA layer where exposed, and overexpose the MMA layer. Since the MMA is overexposed, the MMA under the air-bridge is exposed, while the PMMA air-bridge itself is not exposed. If we were to look at a cross section of the pattern we would see the MMA was over exposed it and it created a ‘undercut’ below the PMMA. The utility of the undercut is twofold: it increases the effectiveness of liftoff, allowing solvent to penetrate beneath the PMMA layer, and it also forms the air-bridge. After development, double angle evaporation is performed used to form the tunnel junction.

The tunnel junction is produced by a shadow evaporation process [108] illustrated in Fig. 5.1. Prior to evaporation, an *in-situ* argon ion milling is performed at a beam voltage of 500 V and current of 30 mA to remove the native aluminum oxide that would prevent good electrical contact between the junction and the SQUID washer/counter electrode. Without breaking vacuum, the first aluminum deposition is performed at an angle of 11.5° with respect to the normal, forming the bottom electrode of the junction. The air-bridge in the resists masks a small area of the substrate, leaving a gap in bottom electrode of the junction. After deposition of the bottom electrode is complete, a carefully controlled amount of argon/oxygen mixture (95:5) is introduced into the chamber and then evacuated after a certain amount of time, typically 45 s. The oxygen in the gas mixture oxidizes the bottom electrode of the junction and the argon in the mixture serves as a buffer gas. The critical current of the junction is determined by the thickness of the oxide layer.

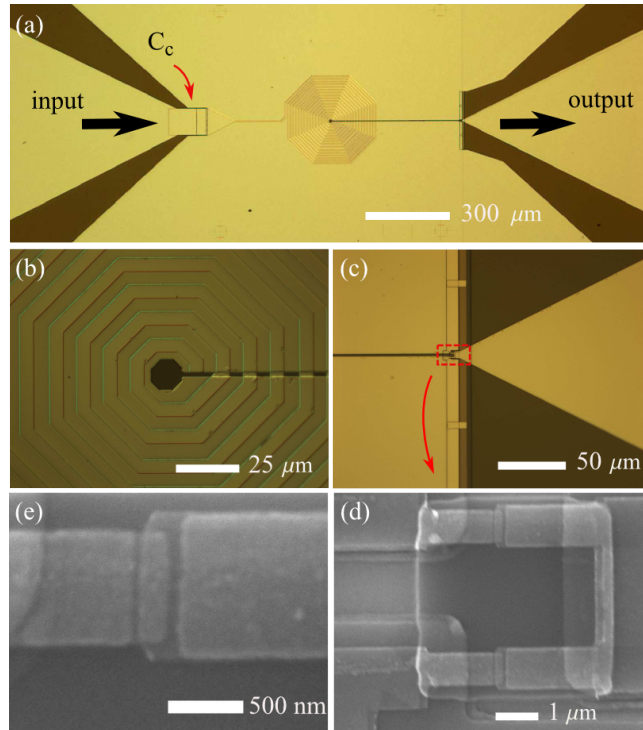


Figure 5.2: Early generation MSA operating at 1.55 GHz. (a) Optical micrograph of washer showing coil, input and output ports, and input coupling capacitor. (b) Closeup of input coil. (c) Closeup of junction and shunt region. (d) Scanning electron micrograph of junctions. (e) Closeup of single junction [109].

The oxide barrier thickness is controlled by varying the pressure of argon/oxygen mixture in the chamber during the oxidation as well as the time of the exposure to argon/oxygen mixture. The dependence of junction critical current on junction exposure time and pressure has been studied extensively [110]. The critical current density of several junctions were measured as function of their exposure to oxygen. When the critical current density was plotted as a function of the product of exposure time and pressure (Pa s) two distinct regimes were identified (low and high exposure). The critical current density dependence in each regime was found to obey a power law with different exponent. In general, the higher the exposure the thicker the oxide barrier will be, hence a smaller critical current will result. Once the bottom electrode of the junction has been oxidized, a second layer of aluminum is deposited on top of

the bottom electrode. The deposition is performed at an angle of -11.5° with respect to the normal, forming the top electrode of the junction. After deposition, the resist mask is dissolved in heated acetone and the fabrication procedure is now complete. The simplicity (single vacuum cycle) and versatility of shadow evaporation make it an attractive alternative to multilayer techniques more commonly used [111] [112] to fabricate larger junctions from other metals besides aluminum. An early generation of completed devices at several levels of magnification is illustrated in Fig. 5.2.

Additional fabrication details and recipes are provided in Appendix A.

Chapter 6

Measurements at 1.55 GHz

6.1 Introduction

This chapter will address measurement techniques used to characterize MSAs. Before cryogenic measurements are conducted, room temperature dc characterization is performed to ensure the device parameters are suitable for low temperature measurement. Once a suitable sample is produced it is cooled to cryogenic temperatures, typically ~ 300 mK in a ^3He refrigerator and dc characteristics or microwave scattering parameters are measured.

6.2 MSAs with small area junctions

Microstrip SQUID amplifiers have been demonstrated to be a promising candidate for cryogenic amplification of small signals in the gigahertz frequency range. In chapter 4 the gain of an MSA was shown to be proportional to $M_i^2 V_\Phi^2$ where M_i is the mutual inductance between the input coil and the SQUID washer and $V_\Phi \equiv \partial V / \partial \Phi$ is the maximum flux-to-voltage transfer function of the SQUID. Pushing the operating frequency f_0 higher requires shorter coils, which necessarily reduces M_i , although this reduction in gain can be somewhat mitigated by modifying the SQUID loop and coil

layout from the conventional washer design. Nonetheless, the gain G will decrease as f_0 is increased unless one can simultaneously compensate by increasing V_Φ . The peak-to-peak voltage modulation of a SQUID is limited by the I_0R product of each junction where I_0 is the junction critical current and R is the shunt resistance. Nonhysteretic device operation requires a junction damping parameter $\beta_c \equiv (2\pi I_0 R^2 C / \Phi_0) \leq 1$, thus placing an upper limit on R , where C is the junction self-capacitance. For Josephson junctions fabricated with conventional photolithography with an area of a few square micrometers, C is typically a few hundred femtofarads. The other standard for SQUID optimization, $\beta_L \equiv 2LI_0/\Phi_0 \approx 1$ [62] constrains the product of the SQUID self inductance L and I_0 . Taking a typical set of SQUID parameters, $L = 350$ pH, $I_0 = 3$ μ A, $C = 200$ fF, the maximum R that maintains nonhysteretic operation is 23 Ω . This then results in a maximum flux-to-voltage transfer coefficient $V_\Phi \approx R/L = 140$ μ V/ Φ_0 [62]. To enhance V_Φ , one can reduce L somewhat, but it then becomes difficult to avoid loss of gain due to the resulting reduction in M_i .

Large values of V_Φ can be achieved by increasing R ; however, C must be reduced in order to avoid hysteretic behavior. We have developed a scheme to enhance the gain of MSAs by using submicron Josephson junctions. The small area of these junctions reduces the junction capacitance C allowing larger values of shunt resistance R to be used while maintaining nonhysteretic operation. This enhancement of gain mitigates the loss of gain at higher frequencies that results from the reduced M_i of shorter input coils.

6.3 Room temperature characterization

Although Josephson junctions only exhibit Cooper pair tunneling below the superconducting transition temperature, it is important to characterize the devices at room temperature to be certain they have characteristics suitable for low temperature measurement. Typically, it takes ~ 24 hours to cool devices to 300 mK, the base temper-

ature of the cryostat, and ~ 24 hours to warm up from 300 mK to room temperature. The ability to characterize devices at room temperature prevents cooling down non-ideal devices.

Two parameters that determine the properties of our devices are the critical current of the junctions and the resistance of the palladium shunts. Although the critical current of a Josephson junction cannot be directly measured at room temperature, the normal state resistance of the junction can. The normal state resistance of the junction is related to the critical current through the Ambegaokar-Baratoff relation [113]

$$I_0 = \frac{\pi}{4} \frac{2\Delta}{eR_n} \quad (6.1)$$

where I_0 is the junction critical current, Δ is the superconducting energy gap, e is the electron charge and R_n is the measured normal state resistance. The junction resistance is measured using a lock-in amplifier to drive current through the junction at a low frequency and the magnitude and phase of the voltage developed across the junction is measured differentially at the same frequency. There is a risk of ‘blowing out’ a junction through electrostatic discharge (ESD) or if too much current is driven through the junction so precautions are taken to reduce the chance of ESD and the drive current is usually limited to 100 nA. It is essential to use a lock-in amplifier to measure the voltage corresponding to this small current. To avoid electrostatic discharge, a low resistance path is kept in parallel with the junction until the measurement is performed.

The resistance of normal metal films is of course temperature dependent and it is crucial to know the value of the shunt resistance at low temperature. This low temperature resistance can be estimated by measuring the device at room temperature, but first the residual-resistivity ratio (RRR) of the film must be determined. The RRR is determined by measuring the resistance of a film at room temperature, then measuring the resistance again at cryogenic temperatures, for instance in a liquid helium bath. The RRR is the ratio of these resistances. The RRR of a film is dependent

on the material properties, the purity of the film, and the film geometry. Therefore it is essential to keep these properties constant from wafer to wafer. For our fabrication technique we are able to produce ~ 20 nm thick palladium films with consistent $RRR = 2.2$ from wafer to wafer, therefore only room-temperature measurement of our shunt resistance is required to estimate the low temperature resistance of the film. The room-temperature resistance of our shunt resistors is also measured with a lock-in amplifier in a four-wire measurement configuration. To perform this measurement as accurately as possible, a chip identical to the chip being measured is prepared. The evaporation, however, is done at a single angle thus there is no conducting path through the junctions and all current flows through the shunt resistors.

6.4 Cryogenic measurement

6.4.1 Cryostat

Cryogenic measurements are performed on a Janis ^3He refrigerator at a base temperature between 300-350 mK. The base temperature of the cryostat varies with the heat load on the cold stage which can change from cooldown to cooldown. Due to the low superconducting transition temperature ($T_c = 1.17$ K) of aluminum, using a pumped ^4He bath is not possible. The vacuum space of the refrigerator is separated from the ^4He bath by a copper can. The ^4He bath serves to cool the cryostat from room temperature to the boiling point of liquid ^4He , about 4.2 K, as well as supply liquid helium to a small pumped helium vessel (1 K pot) in the vacuum space of the cryostat. The steady state operating temperature of the 1 K pot is about 1.7 K, which is cold enough to allow ^3He gas, stored in a vessel on top of the cryostat, to condense in the refrigerator. The ^3He condenses and drips in to a vessel located below the 1 K pot to form a small bath. A cold charcoal adsorber is used to pump the ^3He bath, cooling the ^3He to a temperature of about 250 mK with no heat load on the ^3He vessel. An Oxygen-free Copper cold finger is mounted on the bottom of

the ^3He vessel on which samples and other hardware are mounted. The practical base temperature of the refrigerator with a sample on the cold stage and with requisite measurement circuitry attached is between 300-350 mK. This temperature is limited by heat conducted through wires in contact with warmer stages of the cryostat. Great care is taken when routing wires between stages of different temperature to minimize these heat leaks to the cold-stage of the cryostat.

6.4.2 Device packaging

Devices must be packaged in a way that is appropriate to the measurement and in a way that provides some degree of shielding from the background electromagnetic environment. For measurements of devices at lower frequency (dc - 2 GHz), the sample was mounted on a custom circuit board that provided a means to solder in chip components, such as the coupling capacitor for the input coil and resistors for the current and flux bias circuit. Although this architecture is convenient for fast prototyping, for example, changing the coupling capacitor without fabricating a new device, it does not provide an idea $50\ \Omega$ environment required for measuring devices at higher frequency. The circuit board used to measure dc properties and scattering parameters of early devices is depicted in Fig. 6.1. A schematic of the circuit is depicted in Fig. 6.2. Improvements were made to this measurement scheme for devices that operate at higher frequency and these will be discussed in subsequent chapters.

6.4.3 Low-frequency measurement at cryogenic temperature

SQUID based devices are first characterized at low-frequency at cryogenic temperatures. The current-voltage characteristic and the flux-to-voltage transfer function V_Φ are directly measured. To measure low-frequency properties, devices are configured for a 4-wire measurement where the voltage across the device is measured differentially and the ground is defined explicitly as the shield of the coaxial cable carrying

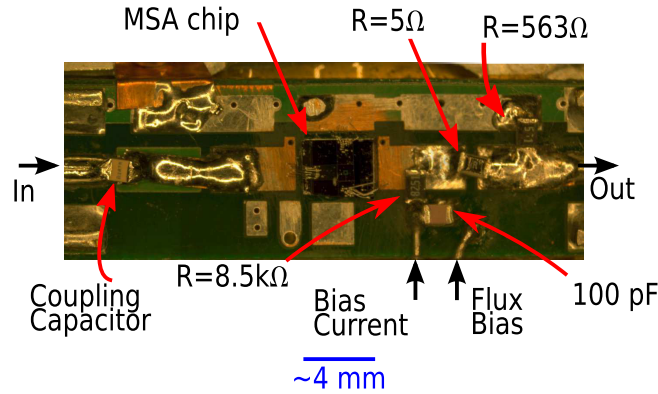


Figure 6.1: Custom circuit board for measuring dc and scattering parameters of the MSA. The board also includes support circuitry for current and flux biasing the MSA.

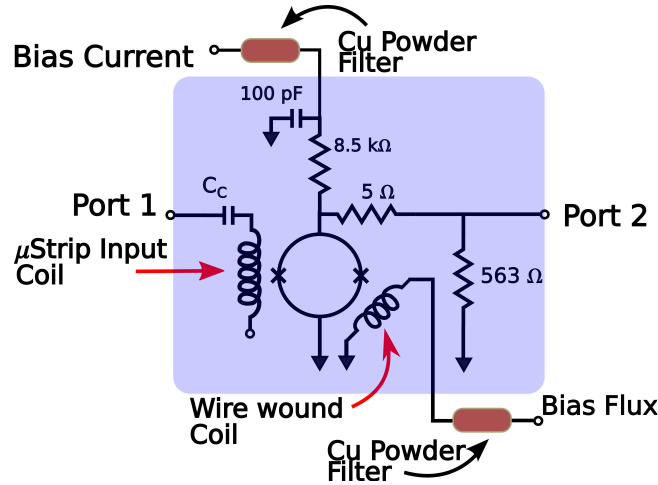


Figure 6.2: Schematic diagram of the on board circuitry used to measure the MSA, as well as filters for dc lines.

signals to the cryostat. Many considerations have to be made when conducting sensitive measurements at dc in order to reduce noise. Common sources of noise that may interfere with measurements near dc are: 60 Hz noise from power mains, general electromagnetic noise that may be inductively picked up by measurement wiring, and ground loops that may cause unwanted currents to flow through parts of the circuit that should be at the same potential.

It is essential to reduce the contribution of each of these sources of noise and we have taken many precautions to do so. To reduce the contribution of currents due to

ground loops, a good low impedance path to ground is required. The cryostat was itself grounded to an earth ground through a large gauge braided copper wire. The chassis of each instrument required to perform the measurement was then grounded to the cryostat through its own braided metal grounding strap to ensure no ground loops were formed between instruments. To prevent cables and wire carrying signals to and from the SQUID from picking up noise through their own inductance, coaxial cables were used to carry signals to and from the cryostat. Within the cryostat, signals were carried by noninductively wound pairs of wires, and coaxial cables. Each wire was filtered with a low-pass π filter at 4 K and a custom-made copper powder filter at 1.7 K.

Noise in the microwave frequency band is inescapable. Even in the sub-basement there are several sources of microwave radiation including: transmissions to and from cellular phones, wireless Internet transmitters and receivers, wireless land-line telephones and Bluetooth electronics. This noise is detrimental to SQUID measurements as dc lines running to and from the SQUID act as antennas and pick up this radiation. This noise, in the worst case, can suppress macroscopic quantum interference. In addition to this, blackbody radiation from ‘hot’ components in the measurement circuitry can also contribute to washing out the SQUID. It is therefore essential to incorporate high-loss cryogenic microwave frequency filters into dc lines when conducting SQUID measurements. The lack of commercial electronic filters that operate at cryogenic temperatures motivated the design of metal powder filters which are commonly used in cryogenic system [114]. Cu powder was mixed with a two part, low-temperature epoxy (Stycast 1266), drawn through small diameter (1/16”) teflon tubing and allowed time to cure. Once hardened, the epoxy/Cu powder cylinder was removed from the teflon tube and formvar-clad Copper wire was wound around the cylinder to form a solenoid approximately 3 inches long. This solenoid was then placed in a cylindrical cavity in an Oxygen-free copper block and held in place by filling the cavity with epoxy/Cu powder mix. Although dc currents can flow freely through

the filter, high frequency signals couple to lossy eddy currents in the copper particles, filtering the signal (with a roll-off of a few hundred MHz) as it passes through the solenoid. The Copper powder filters also served to thermalize wires carrying signals to and from the coldstage of the cryostat.

Electrical and thermal conductivity are intimately related and while it is important to get electrical signals from room temperature to the cold stage of the cryostat, it is equally important to prevent heat from room temperature from being transferred to the cold stage through cables and wires. The heat carried by these cables and wires can easily overwhelm the cooling power of the refrigerator and increase the operating temperature substantially. In order to prevent this from happening, twisted pairs were thermally anchored to the cryostat at 4 K, the 1 K pot stage, and on the ^3He pot stage. Thermal anchoring was performed by winding the twisted pair around a copper bobbin and holding it in place with GE varnish, an electrically insulating material that can withstand thermal cycling and provides decent thermal conduction. The bobbins were in good mechanical contact with thermal baths, for instance, the 1 K pot and the ^3He pot. In order to prevent thermally shorting different temperature stages of the cryostat materials with high resistivity were used. Manganin wire, which has a high resistivity and low temperature coefficient of resistance was used to carry dc signals between stages of the cryostat at different temperature. For microwave signals, coaxial cables made from lossy materials such as stainless steel or a copper-nickel alloy were used to limit conduction of heat from warmer stages of the cryostat. Coaxial cables were also thermally anchored to various temperature stages through copper foil segments soldered to the outer conductor of the cable. In addition to this the drive line was heavily attenuated to reduce the contribution of room temperature noise on the signal. Attenuators were also thermally anchored with copper foil segments at several stages in the cryostat [115].

SQUIDS are known for their ability to detect extremely weak magnetic fields so good magnetic shielding is essential to screen sources of magnetic field noise present in

the laboratory environment. To shield the SQUID from magnetic noise the dewar was situated in a open-top high magnetic permeability material (Mu-metal) cylinder and an additional cryogenic Mu-metal shield surrounded the cryostat's vacuum can in the He bath. The high permeability of the Mu-metal provided a low reluctance path for dc and low frequency magnetic flux, thus shielding the interior of a volume enclosed by the Mu-metal from magnetic noise. To provide further magnetic shielding, the sample was placed in an aluminum box wrapped in Pb foil. At the base temperature of the cryostat, the superconducting lead and aluminum shield the sample from magnetic noise.

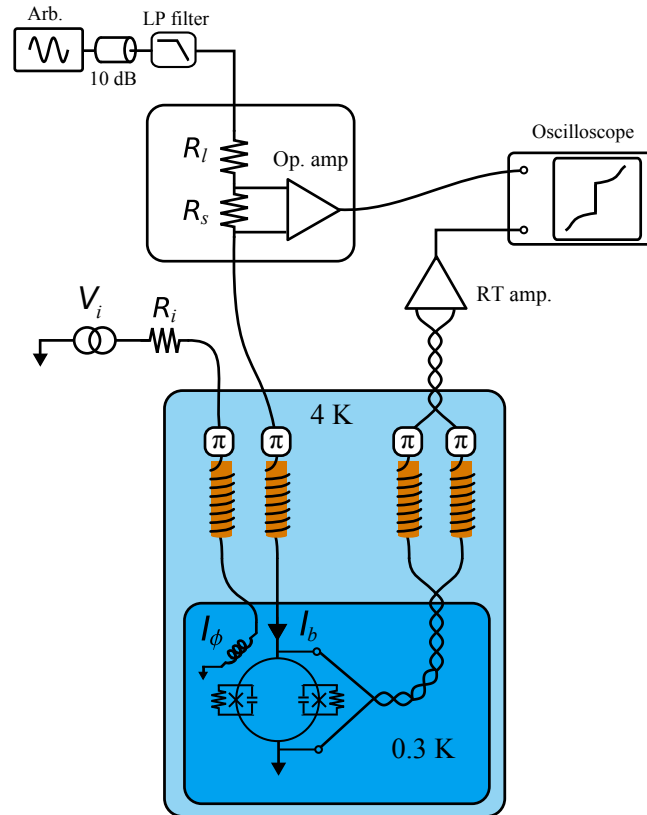


Figure 6.3: Schematic of the circuit for measuring the low-frequency current-voltage and flux-voltage characteristics of the SQUID. In this depiction the circuit is configured to measure the current-voltage characteristic, however the flux-voltage characteristic can also be measured by swapping the circuits used to supply the bias current I_b and bias flux I_ϕ .

Low frequency current-voltage and flux-voltage characteristics were measured at the base temperature of the cryostat. To perform this measurement, a low frequency triangle waveform was produced with an arbitrary waveform generator. The signal was attenuated by 10 dB and filtered with a low-pass filter with a 5 MHz rolloff. This voltage signal was then dropped across a load resistor R_l to produce a current. The value of current was measured by detecting the voltage drop across a standard sense resistor R_s with an operational amplifier. The signal from the operational amplifier was connected to one port of an oscilloscope. The current produced by the load resistor was filtered at 4 K with a π filter and a copper-powder filter and was used to drive the SQUID. A static flux bias was produced with by dropping the voltage produced by a battery across a load resistor. This signal was also filtered at 4 K in the same way as the current bias. This flux bias current was then driven through a wire wound coil inductively coupled to the SQUID. The voltage across the SQUID was measured differentially and carried to room temperature by a non-inductively wound pair of wires filtered at 4 K with copper-powder and π filters. The signal was amplified by an SR-560 differential pre-amplifier. The amplified voltage signal was sent to the second port of an oscilloscope. The oscilloscope was operated in $x - y$ mode displaying the current-voltage characteristic of the SQUID [Fig. 6.4(a)]. The flux bias was adjusted providing the current-voltage characteristic for several flux bias points. To measure the flux-voltage characteristic, V_Φ , the arbitrary wave form generator and support circuitry was used to drive the flux signal of the SQUID, while the bias current was supplied with the battery/resistor combination. The flux-voltage characteristic was measured in the same way as the current-voltage characteristic for several values of bias current [Fig. 6.4(b)]. The maximum-gain bias points for the SQUID correspond to the steepest portion of the magenta curve in Fig. 6.4.

The maximum critical current of this device, $2I_0$, is about $8 \mu\text{A}$. Figure 6.4 shows the dependence of the voltage across the MSA as a function of applied flux for different values of bias current. The magenta curve, which shows the deepest modulation

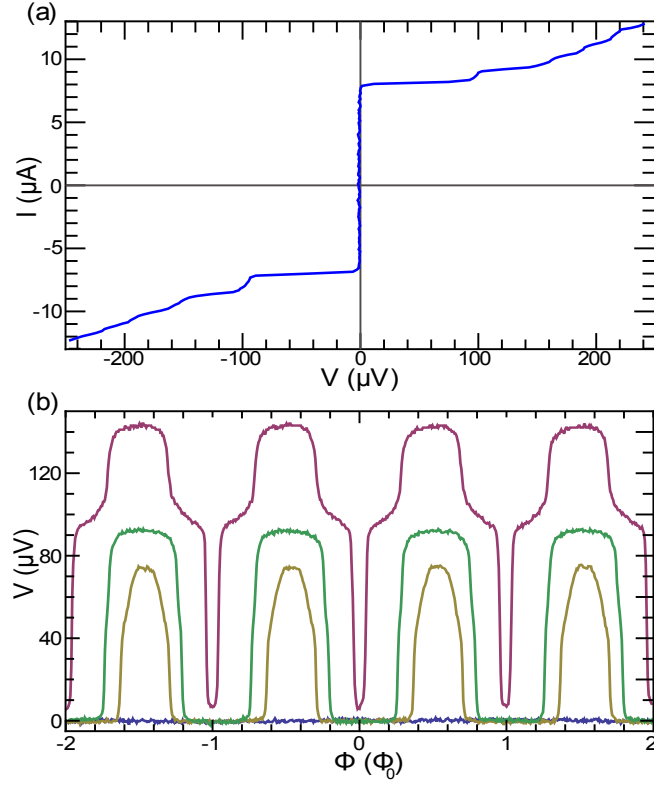


Figure 6.4: (a) Low-frequency current-voltage characteristic at 310 mK for flux bias $\Phi = n\Phi_0$. (b) Flux modulation of voltage across SQUID for different bias current values.

(largest ΔV), represents the value of bias current that provides maximum gain of the MSA. The gain of this device when operated as an amplifier is proportional to the value of $\partial V/\partial\Phi$.

6.4.4 Device parameters

Our SQUID loop consists of a large Al washer on an oxidized Si substrate with a $12\ \mu\text{m}$ wide octagonal hole in the center and a $2\ \mu\text{m}$ wide slit of length $466\ \mu\text{m}$ extending to one side. The standard washer-SQUID expressions can be used to estimate the inductance of the SQUID [116]. The total inductance for our SQUID washer will have two contributions, the inductance of the SQUID slit L_s and the SQUID hole L_h , $L = L_s + L_h$. For a SQUID washer, the inductance of the SQUID slit is estimated to be

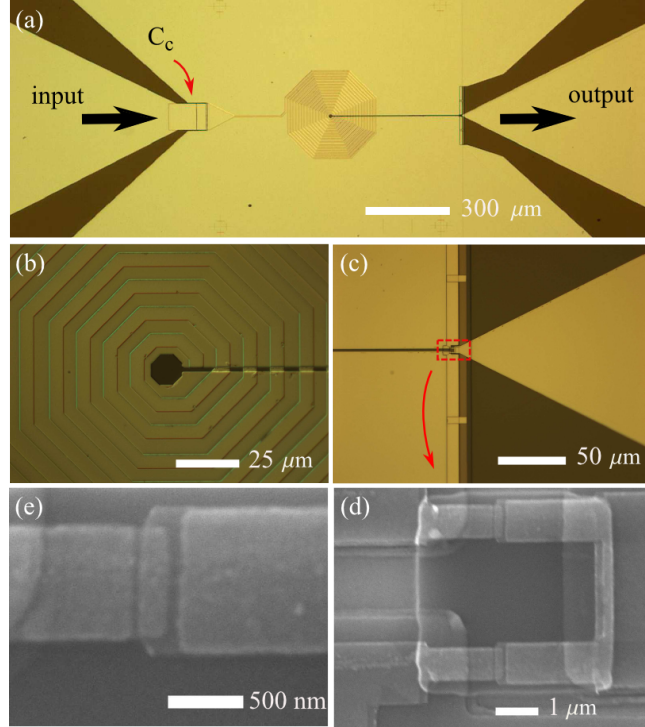


Figure 6.5: (a) Optical micrograph of washer showing coil, input and output ports, and input coupling capacitor. (b) Closeup of input coil. (c) Closeup of junction and shunt region. (d) Scanning electron micrograph of the junctions. (e) A single junction.

$L_s \approx 0.3 \text{ pH}/\mu\text{m} \approx 140\text{pH}$, and for an octagonal SQUID hole $L_H \approx 1.05\mu_0 d \approx 15 \text{ pH}$ where $\mu_0 = 4\pi \times 10^{-7} \text{ Vs/A m}$ and $d = 12 \mu\text{m}$ is the diameter of the hole, yielding a total SQUID inductance of $L \approx 160 \text{ pH}$. The Al washer has an outer-width of 6.5 mm at its midpoint and also serves as the ground plane when the SQUID is operated as a microstrip SQUID amplifier, with cutouts allowing the input and outputs traces to be coupled in a coplanar-waveguide geometry [Fig. 6.5(a)]. The dielectric layer on top of the washer is formed from a 150 nm thick SiO_2 film deposited by plasma-enhanced chemical vapor deposition. The Al input coil has a $5 \mu\text{m}$ linewidth and follows an octagonal path around the washer hole with a length of 8.3 mm and a number of turns $n = 16$ [Fig. 6.5(b)]. This design does not have a connection to the center turn of the coil, thus a direct dc measurement of the mutual inductance, M_i , is not possible. Nonetheless, for our geometry we can estimate M_i . The mutual inductance between

the input coil and SQUID washer is $M_i \approx n\alpha L$ where n is the number of turns of the coil and, L is the SQUID inductance calculated above and α is the fraction of the total slit length enclosed by the center turn of the input coil [116]. For our input coil and SQUID washer geometry we estimate the $M_i \approx 1$ nH. Between the input pad and the coil, we fabricated an on-chip input coupling capacitor that we estimate to be $C_c \approx 4$ pF using the same dielectric layer as on the washer to reduce the loading from the 50Ω environment on the microstrip resonance.

While the initial four layers of the SQUID are patterned photolithographically, the junctions are patterned in a final electron-beam lithography step and are formed with a double-angle shadow-evaporation process [108]. An *in situ* Ar ion mill step ensures superconducting contacts between junction layer and SQUID washer. The junctions are 730×180 nm² [Figs. 6.5(d) and 6.5(e)], from which we estimate the capacitance to be roughly 15 fF, although this estimate could have a substantial uncertainty, particularly when one considers possible stray capacitance in our junction geometry. A detailed recipe for fabricating these devices is given in Appendix A.

6.4.5 Gain

The gain of our microstrip SQUID amplifiers is determined by measuring scattering parameters of the device at microwave frequencies (Fig. 6.6). Scattering parameters are measured using a vector network analyzer. The network analyzer consists of four ports, each with signal generator, a signal receiver, and a directional coupler which discriminates between incoming and outgoing signals. The directional coupler enables an individual port to be used simultaneously as a transmitter and receiver. Signals are carried to and from the network analyzer through coaxial cables. The elements of S are the ratio of the signal measured by a given receiver and the signal produced by a given generator. For the case of a two port device (one input, one output), the scattering parameters compose a 2×2 scattering matrix of complex elements $S_{11}, S_{12}, S_{21}, S_{22}$. Each scattering parameter corresponds to a measurement of

either reflections off of the device or transmission through the device. For instance, if port one is connected to the input of the device, S_{11} is the ratio of the signal reflected from the input of the device to the signal incident on the input of the device. Likewise, S_{21} is the ratio of power transmitted through the device detected at port 2 and the power incident on the device from port 1. Although the full scattering matrix is accessible, we are most interested in the power transmitted through the device S_{21} , which is proportional to the gain of the MSA.

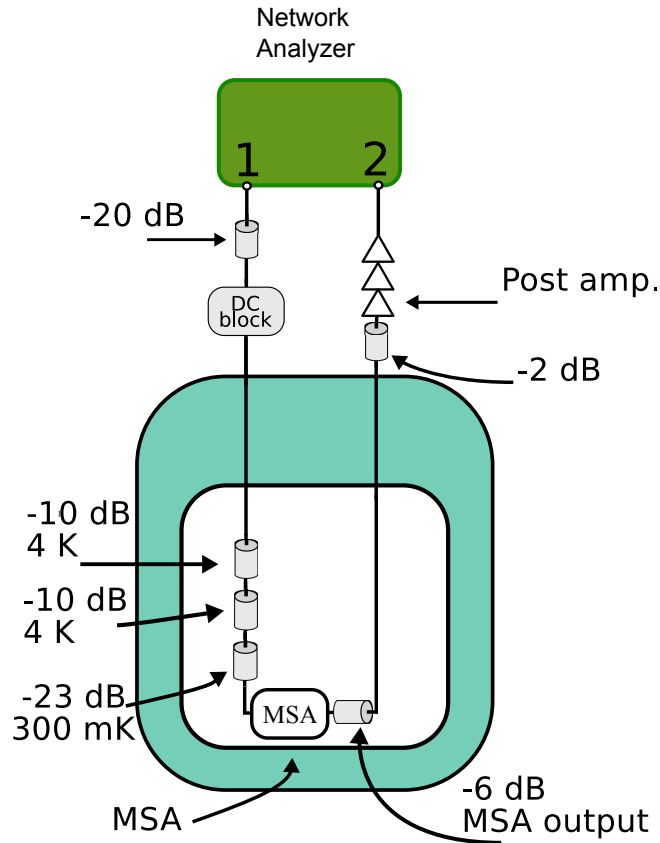


Figure 6.6: Schematic representation of the scattering parameter measurement setup.

In order to carry out an accurate measurement of the device gain, a careful calibration of the loss of additional circuitry must be performed at cryogenic temperature. The refrigerator was prepared by replacing the MSA with a short piece of low-loss coax. The refrigerator was then cooled to 300 mK. The scattering parameter S_{21}

was measured in conditions that were nominally identical to when the MSA gain was measured. The measurement provided a calibration of the total loss (due to lossy coax and attenuators) and gain (from HEMT and room temperature amplifiers) of the circuit. The baseline transmission measurement allows us to calculate the gain of the MSA independent of the rest of the measurement circuit. The gain of the MSA was calculated by subtracting the baseline S_{21} from the S_{21} data acquired when measuring the MSA.

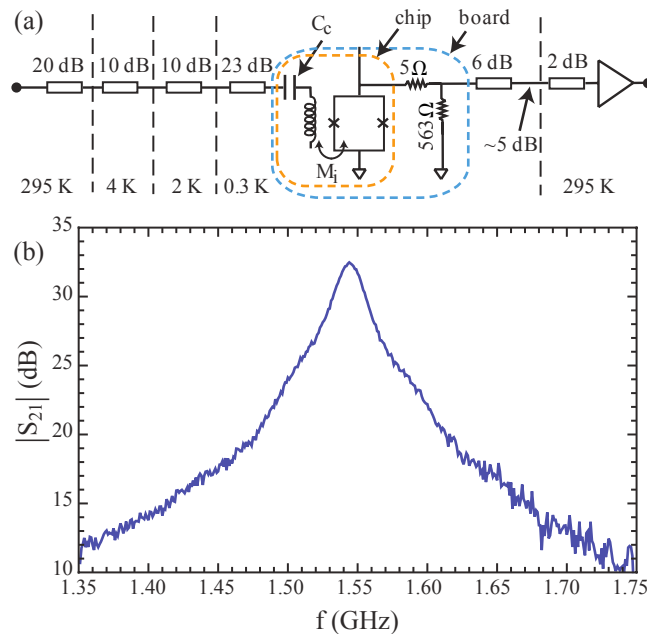


Figure 6.7: (a) Schematic for gain measurement. (b) Gain measurement for optimum bias conditions

We measured the gain of the SQUID amplifier using a network analyzer to supply a weak power to the input of the MSA, ~ -120 dBm. For the optimum bias current and bias flux values, we measured a maximum gain of 32 dB at 1.55 GHz [Fig. 6.7(b)] with a bandwidth of 30 MHz. The bandwidth is defined by the difference in frequency at which the signal is 3 dB less than its maximum value. Upon tuning to the optimum point, the gain was stable and there was no evidence for self-oscillation that is sometimes present for microstrip SQUID amplifiers under certain biasing and input

conditions [105]. A measurement of the noise temperature was not practical with the present configuration due to the substantial contribution from the room-temperature post-amplifier. In the following chapter, we present results for an updated MSA design in a modified measurement configuration using a cryogenic HEMT amplifier and replacing lossy coaxial cables between the output of the MSA and the input of the HEMT with a superconducting coaxial cable. This improved setup reduces the contribution of the post amplifier to the system noise making a noise temperature measurement possible.

It was shown in chapter 2 that the noise of a SQUID is dominated by Johnson-Nyquist noise produced by the shunt resistors. When power is dissipated in a small normal metal volume at low temperatures, electrons can be driven far out of equilibrium with the phonon bath, thus leading to elevated electron temperatures [117]. This is known as the hot-electron effect. One potential concern with increasing the shunt resistance is the possibility for the hot-electron effects to lead to an elevated temperature for the shunts [118]. This effect can be addressed to some extent with metallic cooling fins added to the shunts [119]. Moreover, following the analysis of Hilbert and Clarke [56], the noise temperature of a noise-matched, tuned SQUID amplifier will scale as the ratio of the electron temperature in the shunts to the power gain. For this reason, the enhanced gain resulting from the larger shunt should at least partially compensate any excess noise due to hot-electron effects. In addition to modifying the device design and measurement to optimize performance at higher operating frequencies (discussed in the next two chapters), the next generation of devices also incorporate metallic cooling fins to reduce the temperature of hot electrons. In a further iteration of our design we optimize the cooling fin geometry to further reduce the contribution of these hot electrons which we suspect sets the limit on the noise temperature of our MSAs.

Chapter 7

Measurement of MSAs near 4 GHz

Our first generation of MSAs using submicron area junctions were not well optimized for high frequency low-noise amplification. The design of devices presented in the previous chapter were iterated upon to produce a second generation of microstrip SQUID amplifier. The geometry of the shunt resistors, ground plane, and input coil were optimized for higher frequency, and low-noise operation. Numerous improvements to the measurement scheme were also made, including a more suitable microwave board, current biasing circuit, measurement cables, and the addition of a cryogenic HEMT amplifier at 4 K.

7.1 Second generation devices

In the previous chapter we demonstrated a microwave amplifier with 32 dB of gain at 1.5 GHz. However, the routing of microwave signals in our measurement setup was not appropriate for higher frequency operation. In addition to this, the room temperature post-amplifier and lossy cable at the output of the MSA made an accurate system noise temperature measurement impossible. At higher frequencies, reactive elements in a circuit have a larger effect on the impedance of the circuit. Our goal of producing a microwave amplifier that works at several GHz required a careful redesign of the

device and measurement circuitry. Second generation devices are depicted in Fig. 7.1.

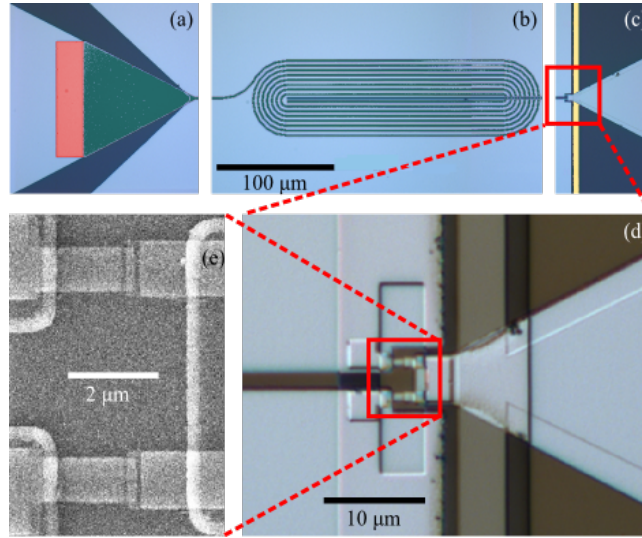


Figure 7.1: (a) False-color optical micrograph of coupling capacitor (red), (b) input coil (green), and (c) Pd shunt resistors (yellow) at scale specified in (b). (d) Closeup optical micrograph of junction and shunt region. (e) Scanning electron micrograph of Josephson junctions.

7.1.1 Microwave board

The second generation MSAs were designed to interface with a custom microwave board (Fig. 7.2). The board consists of three copper layers with dielectric layers sandwiched in between. The top and bottom copper layers, connected to each other through vias, serve as the ground of the board and the center conducting layer forms a broadband microstrip transmission line with ground planes on either side. Microwave signals from the input and output coaxial cables are carried to and from the board through SMA connectors that are in good electrical contact with both the ground and signal layers of the board. This measurement setup has also been used in measurement of other devices over the past several years, including: SQUID oscillators, superconducting coplanar waveguide resonators, and superconducting qubits coupled to cavities. Samples are mounted in a window at the center of the board and

connected to both the ground plane of the board and the center conductor with Al wirebonds. An impedance mismatch between our coaxial cables and the board, or the board and our chip results in reflection of some amount of the input signal, so the board was designed to preserve a 50Ω impedance across the frequency band of our devices. The sample is enclosed by an aluminum box which is affixed to the top and bottom of the microwave board to screen magnetic noise at cryogenic temperatures.

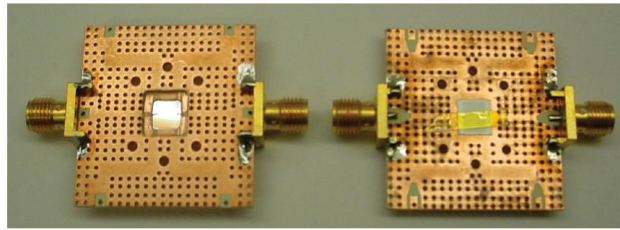


Figure 7.2: Photograph of the custom microwave board with input and output SMA connectors, and a chip mounted at the center.

7.1.2 Input circuit

Signals are carried from the microwave board to the input coil through a tapered coplanar waveguide transmission line. The CPW tapers from a $750\ \mu\text{m}$ to $\sim 100\ \mu\text{m}$ preserving a $50\ \Omega$ impedance. The wide end of the CPW serves as a contact pad which is connected to the microwave board with wirebonds, and the smaller end of the CPW constitutes the bottom plate of the input coil coupling capacitor. The transition from CPW transmission line to microstrip line resonator occurs at the capacitor that couples these two microwave structures. This transition (Fig. 7.3) was carefully engineered to minimize stray capacitance between the input coil and the ground plane [94].

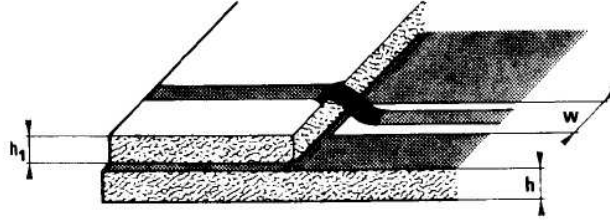


Figure 7.3: Schematic of the coplanar waveguide to microstrip line transition [94]. h_1 is the distance between the signal trace of the microstrip line and ground plane and w is the distance between the ground planes for the coplanar waveguide. (From Gupta, *et al.*, 1996, p.435)

7.1.3 Input coil and ground plane

As discussed in chapter 4, the operating frequency of microstrip SQUID amplifiers is determined by the length of the input coil. To achieve a higher operating frequency, the coil must be shortened. The gain of an MSA is proportional to the mutual inductance between the input coil and SQUID washer $G \propto M_i^2 V_\Phi^2$, where M_i is the mutual inductance. Shortening the coil comes at the expense of gain as it reduces the mutual inductance between the input coil and the SQUID washer. The standard expression for the mutual inductance of typical SQUID washer geometries is given by

$$M_i = n(L_h + \alpha L_t) \quad (7.1)$$

where n is the number of turns in the coil, L_h is the inductance of the hole at the center of the SQUID washer, L_t is the inductance of the slit and α depends on the geometry of the device [120]. The hole at the center of the SQUID slit was eliminated from the ground plane in the second generation design of the MSA because it contributed only a small amount to the total mutual inductance and its presence deforms the path of microwave circulating currents.

The value of the parameter α is determined by that percent of the total SQUID slit the coil couples to and can be estimated by dividing the diameter of the center turn of the coil by the total SQUID slit length. Our earlier MSAs used a spiral input coil centered around a hole in the ground plane at the end of the SQUID slit.

The coil only coupled inductively to a small fraction of the total SQUID slit length, although it had many turns. For MSAs that operate at higher frequency, the total coil length is reduced, therefore the input coil was designed in a geometry resembling a racetrack to provide greater mutual inductance for a given length of coil as compared to a spiral input coil. Although a spiral input coil will have more turns, each turn of the racetrack coil will couple to more of the SQUID slit, thus enhancing the mutual inductance. The second generation of devices employ this racetrack coil with $L_h = 0$, $n = 8$, $\alpha = 202/310$, and $L_t = 90$ pH, yielding an estimated mutual inductance of $M_i \approx 0.5$ nH.

7.1.4 Measurement circuitry

Bias circuitry

The Second generation MSAs are flux biased in a similar way to the first generation, with a wire-wound superconducting coil inside the aluminum box enclosing the MSA. The bias current, which was originally supplied with circuitry mounted to the measurement board is now supplied with a bias-T (HP 11612A) connected to the output of the device. The bias-T provides a means to couple a dc signal to a coaxial cable without loading the microwave properties of the line. A small attenuator between the output of the MSA board and the bias-T matches the impedance of the output of the MSA to 50Ω and protects the MSA from electrostatic discharge by providing a low resistance path to ground.

Output circuitry

The lossy coax that carried the signal at the output of the MSA to the input of the room temperature amplifier in earlier measurements was replaced with superconducting niobium coax. Although this should not have an effect on gain measurements of the device as they are relative to a calibrated baseline, lossless coax is essential

for conducting meaningful system noise temperature measurements as described in the subsequent chapter. In order to reduce the system noise temperature further, the post amplification chain was also improved. Instead of a room-temperature microwave amplifier, a low-noise cryogenic HEMT amplifier was used as the first stage of amplification. The high gain and low-noise of the HEMT amplifier reduces the overall system noise temperature compared to using a room-temperature amplifier as the first stage of amplification. Details of the scheme are discussed in the next chapter. The schematic of the improved gain measurement setup is shown in Fig. 7.4.

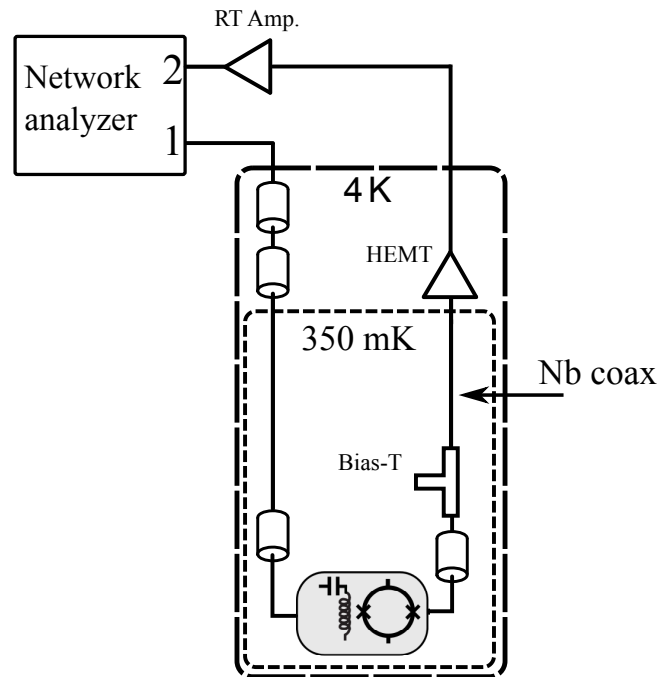


Figure 7.4: A schematic diagram of the gain measurement setup for second generation devices.

7.2 Gain measurement

Gain measurements were conducted at a base temperature of 350 mK on the cold stage of our Janis ^3He refrigerator. Prior to measurement a baseline measurement

was conducted where the MSA was replaced with a piece of low-loss coaxial cable. The baseline measurement provided a calibration of the net losses and gains in the measurement circuit due to cable loss, attenuation, and gain of the post-amplifiers. Once baseline data was acquired, the MSA was installed in place of the short piece of low-loss coax and measured in the next cooldown. The transmission coefficient of the scattering matrix S_{21} was measured as a function of frequency with an Agilent vector network analyzer (N5230A) and gain was determined by subtracting the baseline data from this measured data (Fig. 7.5).

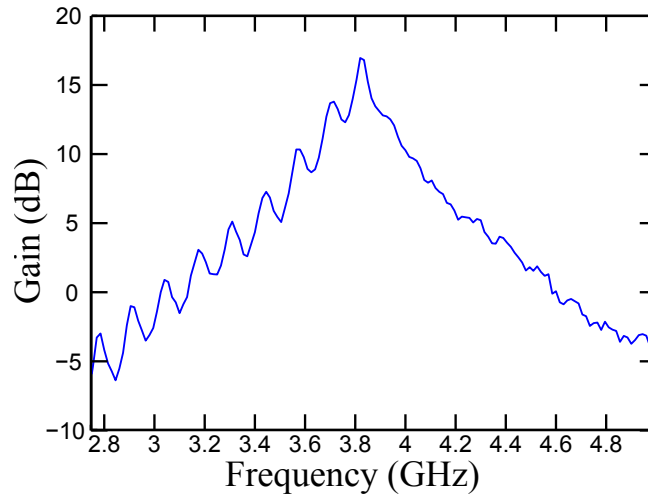


Figure 7.5: Gain as a function of frequency for a second generation device.

The maximum gain of the device was determined to be 17 dB at a frequency of 3.85 GHz in a bandwidth of ~ 150 MHz. The gain and bandwidth of the device are sufficient for amplifying small microwave signals in the band of the amplifier, but there are additional criteria that must be satisfied for the amplifier to be useful. We must investigate the power handling capabilities and the noise properties of the MSA.

The power dependence of the device gain was determined by measuring the gain of the MSA for several input drive powers. For larger input signals, where the highly nonlinear regions of the flux-to-voltage transfer function were accessed by the input flux, the output signal was compressed due to the smaller average voltage across the SQUID. This resulted in a reduction of the gain of the amplifier for larger input

signals. In general, the point where power gain of an amplifier is reduced by 1 dB is a useful figure of merit to describe an power handling of an amplifier. The 1 dB

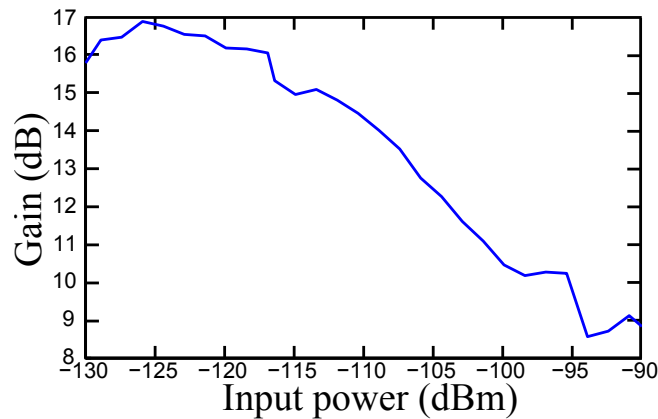


Figure 7.6: The maximum gain of the MSA at 3.85 GHz plotted as a function of drive power relative to the input of the MSA. The gain is compressed by 1 dB at an input power of ~ -115 dBm

compression point of our MSA is ~ -115 dBm and is sufficient to amplify signals of superconducting circuits typical to quantum information science. The noise properties of the amplifier will be discussed in the following chapter.

Chapter 8

Noise

8.1 Introduction

Amplification is often necessary to boost the amplitude of a signal to a detectable level. Noise is ubiquitous in physical systems and every signal is accompanied by some intrinsic noise N_I . The amplifier boosts both the signal, and the noise accompanying the signal by the gain of the amplifier G . In addition to this, the amplifier will add its own noise onto the signal, N_A , which degrades the signal-to-noise ratio. A *good amplifier* is one which adds less noise to the amplified signal than the intrinsic system noise ($N_A < N_I$). Therefore, an amplifier cannot be characterized by its gain alone, the noise the amplifier contributes to the signal must also be taken into account.

8.2 Noise temperature

A useful metric for quantifying the noise properties of any amplifier is the noise temperature T_N . Noise temperature relates the noise added to a signal during amplification to the Johnson-Nyquist noise of a resistor at the input of the amplifier thermalized at temperature T_N . A short description of noise temperature was outlined in chapter 2, we will revisit that discussion here. Consider a system composed

of an amplifier of gain G with a resistor R at temperature T connected to its input [Fig. 8.1(a)], we will refer to this as ‘system A’. The noise power measured at the output of the amplifier has two contributions: the Johnson-Nyquist noise of the resistor amplified by G , and the noise the amplifier adds to the signal. As the temperature T of the resistor R is varied, the voltage noise corresponding to the Johnson-Nyquist noise produced by the resistor will change according to $v_n = \sqrt{4k_B T R \Delta f}$ where k_B is Boltzmann’s constant and Δf is the measurement bandwidth. As the temperature of the resistor is reduced, the total noise at the output of the amplifier will become smaller and at zero temperature only the amplifier will contribute to the total system noise. Now consider an identical copy of this system, ‘system B’, but with the amplifier replaced with an ideal noiseless amplifier with gain G that contributes no noise to the measurement [Fig. 8.1 (b)] but is otherwise identical to the amplifier in system A. The noise temperature of the amplifier is the temperature T_n of the resistor in system B such that the system noise power for system B is equal to system A with the resistor at zero temperature.

Although most elements of a SQUID amplifier are superconducting, and therefore do not produce dissipation, SQUID amplifiers also rely on resistive shunts to keep the flux-to-voltage transfer function single-valued. These dissipative elements are essential to operating a SQUID as a linear amplifier, and the Johnson-Nyquist noise contributed to the amplified signal by the shunts is thus unavoidable. As described in chapter 2, this noise manifests itself as a voltage noise across the SQUID S_V , a circulating current noise around the SQUID loop, S_J , and a voltage-current correlated noise resulting from the nonlinearity of the SQUID, S_{VJ} . At microwave frequency, these three sources of noise constitute the primary noise contributed to an amplified signal by the SQUID.

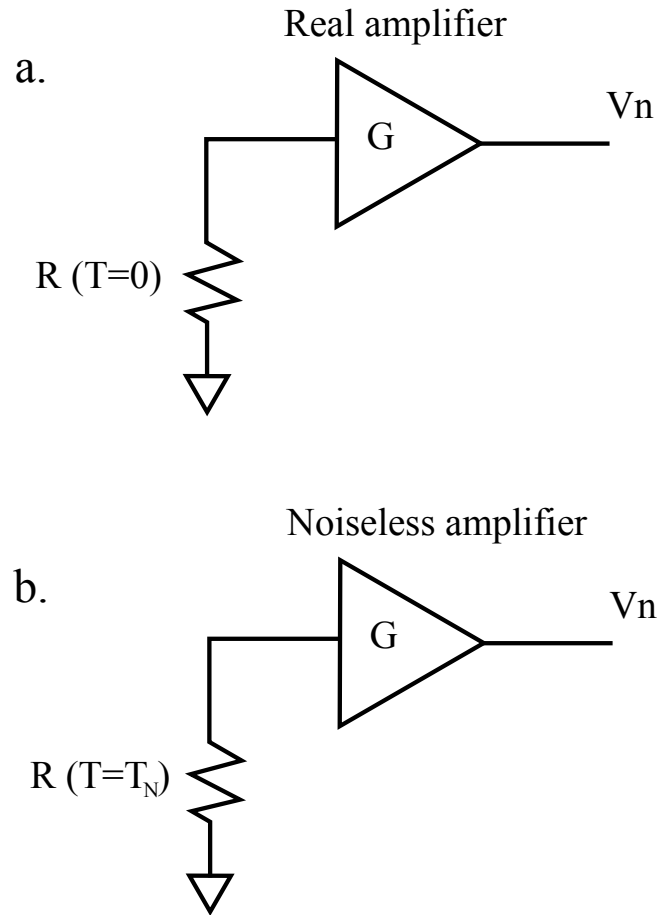


Figure 8.1: Noise temperature schematic. (a) A real amplifier that adds noise to the signal with a source resistance that can be cooled to $T=0$. (b) A noiseless, but otherwise identical amplifier to the amplifier in (a) connected to a source resistor thermalized at $T = T_N$.

8.3 Noise factor, Y-factor and noise temperature

8.3.1 Noise factor

A practical scheme to extract the noise temperature of an amplifier is presented below, however other important metrics for characterizing the noise properties of an amplifier will first be discussed, the noise factor F and the noise figure NF . The noise factor is defined as [93]

$$F \equiv \frac{SNR_i}{SNR_o}, \quad (8.1)$$

where SNR_i is the signal-to-noise ratio for a given signal incident on the amplifier and SNR_o is the signal-to-noise ratio at the output of the amplifier and is related to the noise figure by $NF = 10 \log_{10} F$. For an ideal amplifier which adds no noise to the amplified signal, $F = 1$, for an amplifier that contributes any amount of noise, $F > 1$. Despite its simple definition, noise factor is a difficult quantity to measure. One of the difficulties in measuring noise factor arises from the fact that the measurement depends on the physical temperature of the signal source. For instance, consider a noise factor measurement for an amplifier where the source is at a very low temperature. The output signal-to-noise ratio will be dominated by the amplifier noise and the system noise will make less of a contribution. If the source is sitting at a higher temperature for the same input signal, the input signal-to-noise ratio will be small, yielding a smaller noise factor compared to the previous case. To circumvent this issue, noise factor measurements are performed at a standard source temperature which, for historical reasons, is 290 K. Aside from the practical issue of having to control the source temperature, there are other practical considerations that make this measurement difficult to execute [93].

The noise at the output of the system will have two components: the noise contributed from the amplifier itself N_a , and the amplified source noise power

$$N_s = k_B T_0 B G \quad (8.2)$$

where $k_B = 1.38 \times 10^{-23}$ J/K is Boltzmann's constant, $T_0 = 290$ K, B is the noise bandwidth and G is the power gain of the amplifier [93]. The total noise power at the amplifier output is

$$N_o = k_B T_0 B G + N_a. \quad (8.3)$$

Writing the definition of noise figure more explicitly results in

$$F \equiv \frac{SNR_i}{SNR_o} = \frac{S_i/N_i}{S_o/N_o} \quad (8.4)$$

where $S_{i(o)}$ and $N_{i(o)}$ are the values of the input (output) signal and noise, respectively. The ratio of the output signal to the input signal $S_o/S_i = G$ is simply the gain of the amplifier, and the output noise N_o is defined above. The input noise power is $N_i = k_B T_0 B$, therefore

$$F = \frac{1}{G} \frac{N_o}{N_i} = \frac{k_B T_0 B G + N_a}{k_B T_0 B G}. \quad (8.5)$$

Noise factor, as expressed on the right hand side of Eq. (8.5) is the official Institute of Electrical and Electronics Engineers definition of noise figure and requires measurement of the noise, the device gain G and the noise bandwidth B , all at a standard temperature T_0 [93].

8.3.2 Y-factor

An alternative technique for measuring noise figure that does not require measurement of system parameters such as gain and noise bandwidth is known as the Y-factor measurement. A Y-factor measurement relies on comparing the ratio of noise measurement at two different source temperatures. As previously discussed, the total system noise has two components: the noise of the source impedance and the noise added by the amplifier. A hot source will contribute more to the total system noise than a cold noise source. The measurement now relies on noise power ratios that do not require absolute measurements of gain and bandwidth. A Y-factor measurement is typically performed by connecting a source R at temperature T_{hot} to the input of the amplifier and measuring the noise power at the output of the amplifier N_{hot} . The temperature of the source is then reduced to a lower temperature T_{cold} and the noise power N_{cold} is measured. For a linear amplifier, the noise power is expected to vary linearly with source temperature. By plotting the system noise power as a function of temperature and fitting a line to the data (Fig. 8.2), this measurement can be used to calculate the system noise figure.

At zero temperature the source should contribute no noise, therefore the y-intercept of the linear fit will correspond to the amplifier noise N_a . Rewriting the definition of

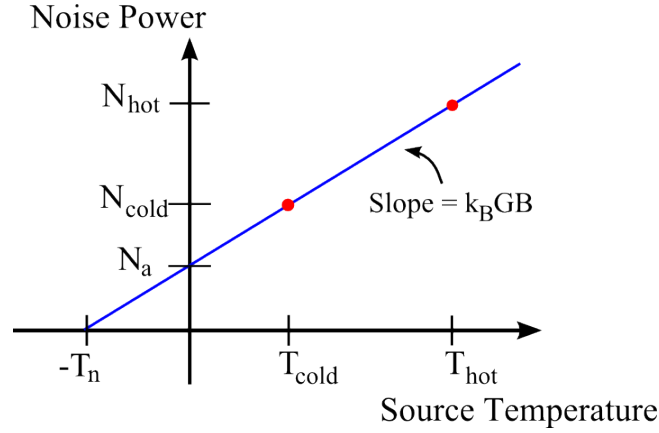


Figure 8.2: Schematic plot of the system noise as a function of source temperature with a linear fit.

noise factor in terms of values from Fig. 8.2, T_{cold} , the slope of the linear fit, and the intercept of the y-axis, the following expression is obtained

$$F = \frac{k_B T_{cold} B G + N_a}{k_B T_{cold} B G} = 1 + \frac{N_a}{k_B T_{cold} B G} = 1 + \frac{y - intercept}{(T_{cold})(Slope)}. \quad (8.6)$$

This type of measurement is known as a Y-factor measurement because the ratio, $Y \equiv N_{hot}/N_{cold}$, is known as the Y-factor. In terms of Y-factor, the noise factor can be expressed as

$$F = \frac{\frac{T_{hot} - T_{cold}}{T_{cold}}}{Y - 1}. \quad (8.7)$$

Measurement of the Y-factor—which only require measurement of the system noise at two different source temperatures—is an attractive alternative to a traditional noise factor measurement that requires simultaneous measurement of system noise power, G , and B at $T = 290$ K. Although only two temperature points are necessary to perform this analysis, including more temperatures in the measurement will provide a better fit to extract the slope and intercept. The larger the range of source temperatures, the more accurate the linear fit. Our measured data often covers several orders of magnitude in both source temperature and measured noise power. Although the data is linear it is convenient to plot it on a log-log scale due to the

range in temperature and power of the data. In the following figure our technique for extracting the noise temperature from a log-log plot is presented. The data in the plots is not measured, they are linear and are only for the purpose of schematically illustrating our technique (Fig. 8.3).

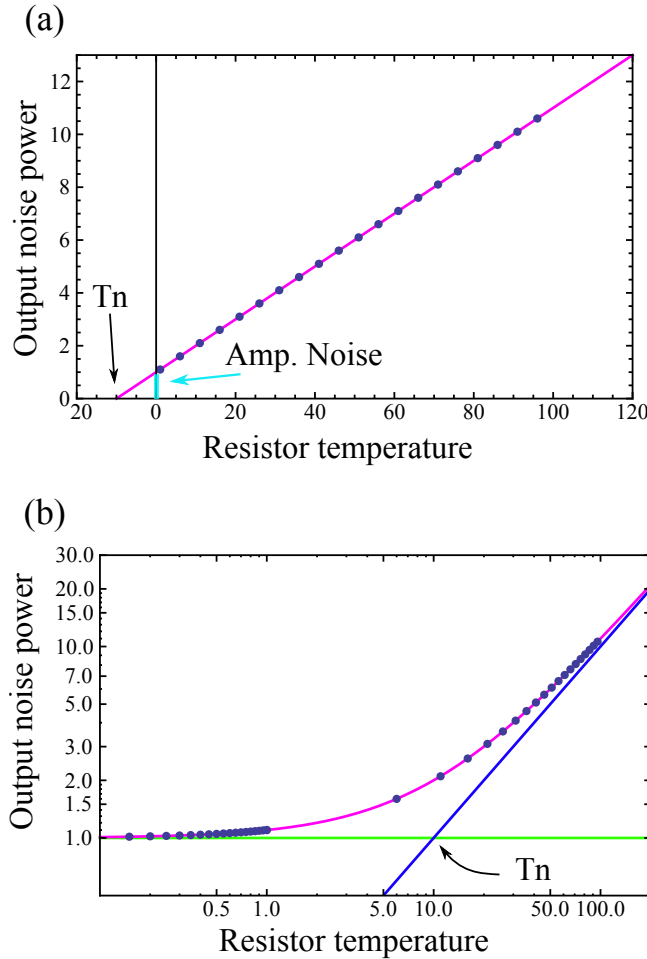


Figure 8.3: Schematic plot a Y-factor measurement plotted on (a) a linear scale and (b) a log-log scale.

In the schematic plot [Fig. 8.3(b)], additional data points are added at low temperature on the log-log plot to simulate a realistic data set. When plotted on a linear scale, the system noise temperature can be determined by fitting the data to a line and extracting the point where the line intersects the temperature axis. Although this occurs at a negative temperature, it can be shown through a geometrical ar-

gument that this point is equivalent to the system noise temperature. On the plot figure 8.3(a), the data is fit to a line (magenta) with an offset and a slope. In Fig. 8.3(b), the same linear fit is plotted with the data (magenta) in addition to the offset value of the linear fit (green) and the slope of the linear fit (blue). On a log-log scale, the system noise temperature occurs at the intersection of the slope and offset of the linear fit. In terms of noise figure F , the noise temperature can be expressed as [93]

$$T_n = (F - 1)T_{cold}. \quad (8.8)$$

8.3.3 Noise temperature measurements of low-noise amplifiers

Noise temperature of a cascaded system

Noise temperature is an important quantity for characterizing the performance of an amplifier. In the previous section the method for extracting the system noise temperature graphically from Y-factor measurement data was discussed. In this section we discuss some important considerations that need to be made when extracting the noise temperature of a chain of amplifiers. One technique to measure the noise temperature of an amplifier is to perform a Y-factor measurement at liquid nitrogen temperature and room temperature. The noise temperature of most room-temperature amplifiers is usually large enough to measure accurately without additional amplification (several hundred to several thousand Kelvin). However, for an amplifier with low added noise, it is often necessary to use additional amplification to be able to detect the small noise signal produced by the amplifier under investigation. For a cascaded system of amplifiers, each amplifier will add its own noise to the measurement. Therefore, it is important to understand how each amplifier contributes to the measured system noise temperature.

To understand this, let us consider a cascade system of three amplifiers (Fig. 8.4) with respective gains G_1, G_2, G_3 and noise temperatures T_{n1}, T_{n2}, T_{n3} with a source

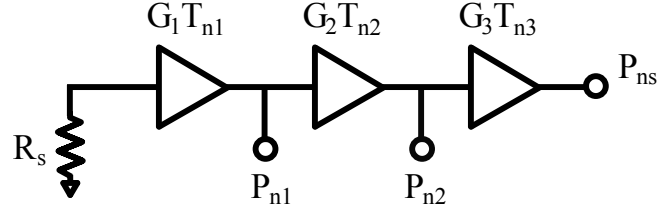


Figure 8.4: Schematic representation of three cascaded amplifiers with resistive source R_s at the input of the first stage of amplification.

resistance R_s at the input of the first amplifier thermalized at temperature T_s . This analysis assumes that the impedances of the amplifiers are well matched to each other as well as to the source impedance. In the absence of the second and third stages of amplification, the noise power at the output of amplifier 1, P_{n1} , will have two contributions, the amplified Johnson-Nyquist noise of the source, and the amplifier noise [93]

$$P_{n1} = k_B T_s B G_1 + k_B T_{n1} B G_1 = k_B (T_s + T_{n1}) B G_1. \quad (8.9)$$

The second stage will amplify the noise at the output of the first stage and add its own noise onto the signal

$$P_{n2} = k_B (T_s + T_{n1}) B G_1 G_2 + k_B T_{n2} B G_2. \quad (8.10)$$

Alternatively, amplifiers 1 and 2 can be considered a single stage with gain $G_1 G_2$ and noise temperature T_{n12} [93]. The noise power at the output of this two-amplifier system can equivalently be written as

$$P_{n2} = k_B (T_s + T_{n12}) B G_1 G_2. \quad (8.11)$$

By equating Eqs. (8.10) and (8.11) the noise temperature of the first two stages T_{n12} can be expressed as

$$T_{n12} = T_{n1} + \frac{T_{n2}}{G_1}. \quad (8.12)$$

Taking the third stage of amplification into account, the total system noise power is expressed as

$$P_{ns} = k_B (T_s + T_{n12}) B G_1 G_2 G_3 + k_B T_{n3} B G_3. \quad (8.13)$$

Again, considering the cascade of three amplifiers as a device with gain $G_{13} = G_1 G_2 G_3$ and noise temperature T_{n13} , the total noise power of the cascade is

$$P_{ns} = k_B(T_s + T_{n13})BG_{13}. \quad (8.14)$$

Combining Eqs. (8.13, 8.14, 8.12), T_{n13} can be expressed in terms of the noise temperatures and gains of individual elements

$$T_{n13} = T_{n1} + \frac{T_{n2}}{G_1} + \frac{T_{n3}}{G_1 G_2}. \quad (8.15)$$

From this result it is clear that for a system of cascaded amplifiers the primary contribution to the system noise temperature comes from the first stage of amplification, provided G_1 is large enough to reduce the contribution from elements further up the chain. Therefore, for our measurement of system noise temperature the first stage of amplification will make the dominant contribution.

Impedance matching

Impedance matching is the practice of designing the input impedance of an electrical circuit Z_i to maximize the power transfer from the source [65]. In the case of optimizing the gain of an amplifier, ideal impedance matching occurs when the source impedance Z_s is equal to the input impedance of the amplifier $Z_s = Z_i$. Under this condition, the entire input signal will be transmitted through the circuit and none of the signal will be reflected off of the circuit input impedance. For an amplifier, an impedance mismatch will cause reflections of the signal off of the input of the amplifier resulting in a loss of transmitted signal, and consequently a loss in gain [93]. In light of the result above for the noise temperature of a cascaded system of amplifiers, one is tempted to assume that ideal power matching of the amplifiers will result in a minimum system noise temperature, however this is not always the case. To optimize the noise performance of an amplifier, the noise impedance of the amplifier should be well matched to the source impedance [65]. The noise impedance Z_N is the ratio of

the voltage noise e_N to the current noise i_N

$$Z_N = \frac{e_N}{i_N}. \quad (8.16)$$

When the noise impedance of an amplifier is equal to the source impedance $Z_N = Z_s$ the amplifier is said to be noise matched. When the noise matching condition is satisfied, the noise added onto the signal by the amplifier when connected to that particular source is at its minimum value. Although it is desirable to have simultaneous power and noise matching, in general these conditions are not simultaneously satisfied. Recently, numerical simulations were performed to model a system similar to a SQUID amplifier. It was shown that it is not possible to satisfy ideal power and noise matching conditions simultaneously, however ideal power and noise matching conditions converge at higher frequencies [84].

8.4 Noise temperature measurement techniques

8.4.1 Signal-to-noise ratio comparison

Before performing a noise temperature measurement, a signal-to-noise ratio measurement is carried out for the system with, and without the MSA in the measurement chain. Comparing the values of the system SNR with and without the MSA provides a way to estimate the noise properties without performing a full system noise temperature measurement. Using this SNR ratio technique, the MSA amplifies the input signal by the gain G of the MSA, and also amplifies the noise accompanying the signal as well as add its own noise onto the signal in the process of amplification. Comparing the SNR before and after measurement provides an estimate of the system noise temperature. The net result of adding the MSA to the measurement circuit should be to increase the signal-to-noise ratio of the system—as the gain of the MSA will reduce the overall noise temperature of the circuit as described in the previous section—provided the MSA is a *good* amplifier. If a decrease in the signal-to-noise

ratio is observed when the MSA is included in the circuit, this means either the gain of the MSA is not large enough to reduce the noise contribution of the HEMT and room temperature amplifiers, or the noise temperature of the MSA is too large for it to be useful as an amplifier.

To measure the SNR, a single-tone microwave signal of power -145 dBm at the input of the MSA was incident on the measurement chain and noise spectra were acquired at the output of the chain. This marker tone was produced by mixing the output of a microwave generator with a calibrated noise source. For SNR measurements, the noise source was set at a value below the intrinsic system noise in order to avoid measuring an artificially low SNR. Noise spectra were acquired with a spectrum analyzer (HP 8563E). The signal was detected in a resolution bandwidth of 30 kHz over a span of 2.5 MHz and was measured in dBm. Averaging was performed on the spectrum analyzer and a single measurement constituted the average of 1000 spectra. The signal-to-noise ratio was determined by the difference in dB between the peak signal amplitude and the noise floor (Fig. 8.5). In addition to the marker tone signal visible at 3.811 GHz in Fig. 8.5, another peak occurred at a frequency of 3.810 GHz. This tone was a result of carrier leakage of the local oscillator used to drive the mixer and did not contribute a significant amount of power to the SNR measurement.

The SNR ratio measurement was performed in two cooldowns, one with the 3.8 GHz MSA discussed in the previous chapter in the measurement circuit and one without the MSA. This SNR-ratio technique is sensitive to any impedance mismatches between the MSA and the input and output circuitry, therefore it provides an upper bound on the noise temperature of our system. Comparing the SNR of these two measurements at 4 GHz yields a maximum SNR increase of 7.2 dB with the MSA in the circuit. Our measured HEMT noise temperature is 3.1 K (details of this measurement will be present later in this chapter) and the system noise temperature with the MSA can be estimated by scaling the noise temperature of the HEMT by the SNR improvement of 7.2 dB. This yields an estimated system noise temperature

of 0.59 K. We measured the SNR with the MSA included in the circuit over the full frequency span of the MSA, however the HEMT SNR was only measured at 4.0 GHz. Thus, for our analysis we assumed the gain and noise of the HEMT to be constant over the measured frequency span. The error bars on the SNR-ratio points were estimated from the small expected variation in these quantities based on the HEMT data sheet.

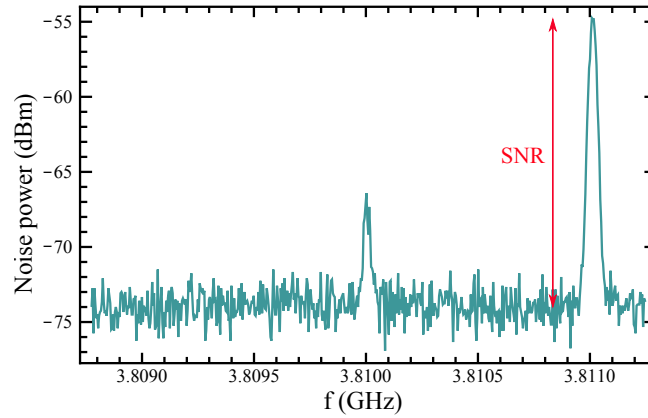


Figure 8.5: Measured signal-to-noise ratio data for the MSA.

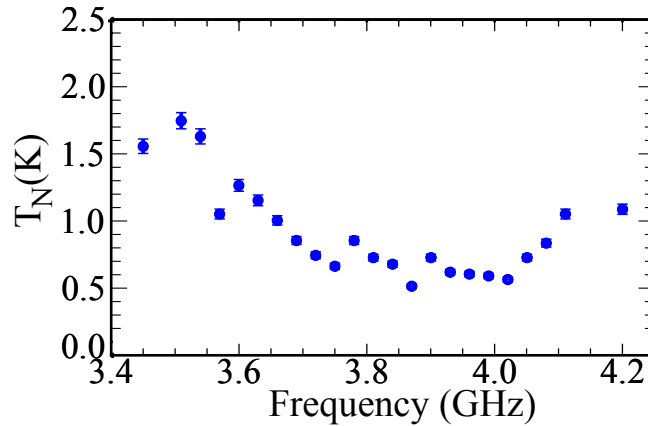


Figure 8.6: T_N measured over a 0.8 GHz span around the maximum gain of the MSA using the SNR-ratio technique. Determination of error bars as described in the text.

8.4.2 Modified Y-factor measurement

We performed an alternative investigation of the system noise using a modified narrowband Y-factor measurement. Although a conventional Y-factor measurement is, in principle, possible for a low-noise cryogenic amplifier, there are many subtleties which make it difficult to implement and achieve accurate results. Instead of using the Johnson-Nyquist noise of a temperature-controlled resistor as a signal source as in a conventional Y-factor measurement, amplified noise from a room-temperature impedance was used to drive the device. Broadband noise was produced by terminating the input of a room temperature amplifier with a $50\ \Omega$ load. The Johnson-Nyquist noise of the load was boosted by the voltage gain of the amplifier ($G_V = 2000$) and was low-pass filtered at 300 kHz. A variable attenuator (Vaunix Lab Brick LDA-602, 0-60 dB with 0.5 dB step) was used to adjust the noise power at room temperature. The noise power was measured at room temperature with a spectrum analyzer in the frequency band of the MSA for several different levels of attenuation to calibrate out cable and insertion losses. The signal from the output of the variable attenuator was carried through a coaxial cable to the top of the cryostat where it interfaced with a lossy semi-rigid coaxial cable that carries the signal to the 4 K plate. At the 4 K plate, the signal was attenuated by 10 dB to reduce the contribution of unwanted room temperature noise. This signal was attenuated further with attenuators thermalized at the ^4He plate (10 dB at 4.2 K) and the cold plate at the input of the MSA (30 dB at 350 mK). Including loss from cables, the total loss measured at room temperature from the top of the cryostat to the input of the MSA is ~ 46 dB in the frequency band of interest.

The signal noise power in a given resolution bandwidth can be related to the Johnson-Nyquist noise of a matched resistive load at a temperature T_{eff} . Varying the noise power at the input of the MSA is analogous to changing the temperature of a resistive load, the technique common to traditional Y-factor measurements, but difficult to implement for a cryogenic amplifier. A second microwave generator was

used to produce a calibration tone, displaced from the center frequency of the noise signal by 1 MHz, and this was combined with the noise signal through a directional coupler (Figs. 8.7, 8.8). At large enough noise power, the gain of the MSA can compress as discussed in the previous chapter and drift of the bias parameters can occur. The peak height of this tone was used to monitor the gain of the device during the measurement to ensure the gain of the MSA was not compressing and the bias values were not drifting. Although this technique presents many advantages to a traditional Y-factor measurement, it depends on the accuracy of the calibration of the total loss of the drive line. We estimate a systematic uncertainty of ± 1 dB on this calibration based on a variety of room-temperature and cryogenic measurements of individual microwave components. This systematic uncertainty is accounted for with error bars with upper and lower limits set by the calculated noise temperature for a given input T_{eff} with ± 1 dB of extra loss on the drive line.

As discussed earlier in this chapter, the primary contribution to the system noise temperature comes from the first stage of amplification, the MSA, however the second stage of amplification, the HEMT amplifier, also contributes. The room temperature amplifier, although it has a large noise temperature ($T_N = 315$ K), it is divided by the combined gain of the MSA and the HEMT, roughly 52 dB or a factor of almost 160,000. The HEMT amplifier is estimated to contribute a small amount to the system noise temperature, ~ 0.10 K, to the system noise temperature measurement. The contribution of the HEMT amplifier depends on the circuitry between the output of the MSA and the input of the HEMT.

Between the output of the MSA and the input of the HEMT there is a 2 dB attenuator, a bias-T and long segment of niobium coaxial cable. It is important to match the output impedance of the MSA to 50Ω , therefore a 2 dB attenuator is used on the output of the MSA for this purpose. The attenuator also provides a resistance to ground in series with the tunnel junctions to reduce the chance of destroying the junctions with electrostatic discharge when mounting the sample and connecting

circuitry. A bias-T was used in the output circuit to provide a dc path to current bias the MSA without loading the output circuitry. A lossless superconducting niobium coaxial cable connects the output of the bias-T, at 350 mK to our first stage of amplification, a HEMT amplifier at 4 K. The benefit of using superconducting coax at this stage of the circuit is twofold: it provides thermal isolation between stages at different temperatures when superconducting and, more importantly, the insertion loss of the coax is effectively zero. For the drive side of the circuit it is important to build in sources of loss to reduce the contribution of unwanted thermal noise therefore substantial attenuation and lossy coaxial cable is used. The output circuit, however, is a different story.

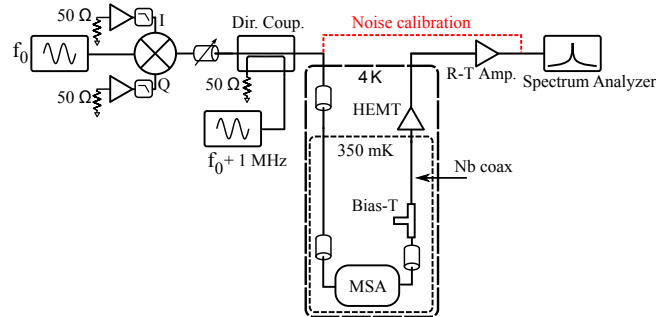


Figure 8.7: Schematic representation of the circuit used to measure the noise temperature of the system including room temperature electronics for preparing the narrowband noise.

As previously discussed, for a system of cascaded amplifiers much like the system under measurement the noise temperature of the second stage amplifier is reduced by the gain of the first stage of amplification and the noise temperature of the third amplifier is reduced by the product of the gain of the first two stages of amplification. Therefore, to reduce the noise contribution of other amplifiers to the system noise temperature measurement, the *net gain* of the MSA must be as large as possible. In addition to this, any loss between the MSA and HEMT at a temperature higher than the temperature of the MSA also adds its own thermal noise onto the system noise temperature. Even a small amount of attenuation at a slightly elevated temperature can make a significant contribution to the system noise temperature [95]. The net

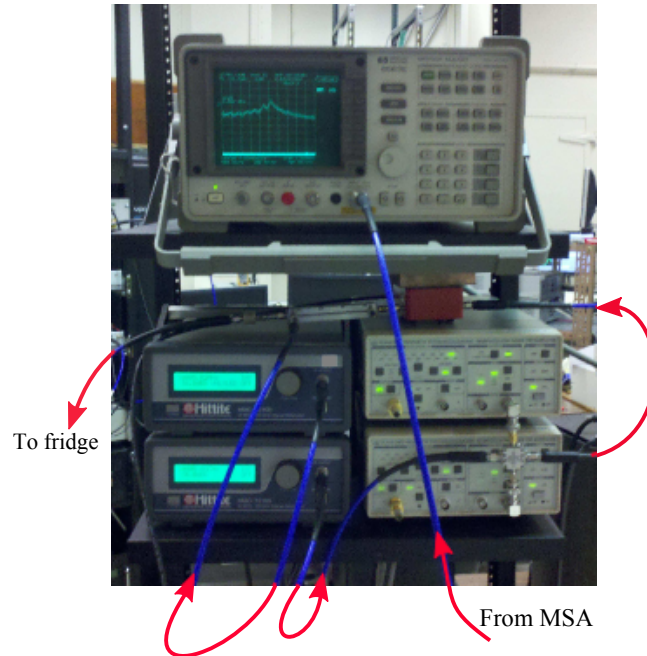


Figure 8.8: Picture of the room temperature electronics used to produce narrowband noise for T_n measurement, and to measure the system noise power.

gain of the MSA is the measured gain of the device, less any loss between the MSA and the first stage of amplification. Minimizing the loss between the MSA and the HEMT amplifier enhances the net gain and reduces the contribution of the HEMT and the room temperature amplifier noise to the total measured system noise. Using as small amount of attenuation as possible and replacing lossy coaxial cable between the MSA and the HEMT with superconducting coaxial cable minimizes the loss between the MSA and the HEMT amplifier, reducing the noise temperature contribution from the HEMT.

8.5 Results

The modified Y-factor measurement technique was implemented to perform a noise temperature measurement of a known quantity, our HEMT amplifier (with the MSA removed from the circuit), as a proof-of-principle demonstration. The various stages of

the measurement process are illustrated in Fig. 8.9. The acquired data is plotted on a log-log scale and the offset and slope of the data are fit and plotted independently. The system noise temperature occurs at the intersection of these two lines, as discussed earlier in this chapter. The offset and slope of the data are combined and plotted as a single line to fit the data. The result of this measurement [Fig. 8.9(c),(d)] yields a system noise temperature of 3.1 K at a frequency of 4 GHz, which was in agreement with the HEMT data sheet provided by the manufacturer. In a subsequent cooldown the system noise temperature was again measured, but now with the MSA in the measurement circuit. With the MSA biased for maximum gain, a minimum system noise temperature of $0.55 \text{ K} \pm 0.13 \text{ K}$ was observed at a frequency of $\sim 3.8 \text{ GHz}$ (Fig. 8.10).

8.5.1 Frequency dependence

By repeating the procedure for measuring noise temperature, but varying the signal frequency being mixed with the noise, the frequency dependence of the system noise temperature was measured (Fig. 8.11). Within the 150 MHz bandwidth of the MSA, the system noise temperature was consistently below 1 K. The system noise temperature increases outside of that band for two reasons: the gain of the MSA is reduced, thus enhancing the contribution to the system noise from the HEMT according to Eq. (8.15), and also the noise temperature of the MSA is itself frequency dependent and minimized in the vicinity of maximum gain.

8.5.2 Temperature dependence

The noise properties of SQUID amplifiers have been studied extensively with numerical simulations [57, 62, 76, 121]. For sufficiently high frequencies, the noise floor of a SQUID amplifier is dominated by Johnson-Nyquist noise of the resistive shunts, and thus scales with the electron temperature in the shunts. For a tuned SQUID amplifier operating at ω_0 with optimal noise matching to the source impedance, the noise

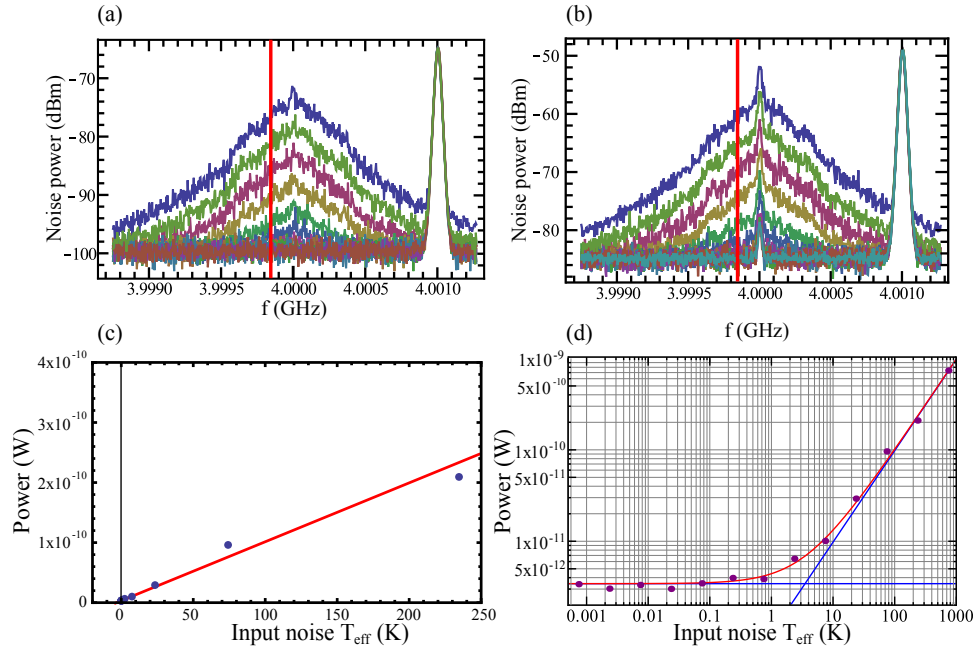


Figure 8.9: (a) Calibration measurement of narrowband noise signal with marker tone for several different noise powers. The vertical red line represents frequency slice used to produce plots (c) and (d). (b) Measurement of the system noise power when driven by calibrated noise signals in (a). (c) Linear plot of system noise power as a function of input effective temperature. x-axis points correspond to effective temperatures calculated from points along the red line in panel (a). y-axis points correspond to measured noise power along the red line in panel (b). The range of this plot has been reduced to show detail around $T_{eff} = 0$. (d) The full data set plotted on a log-log scale.

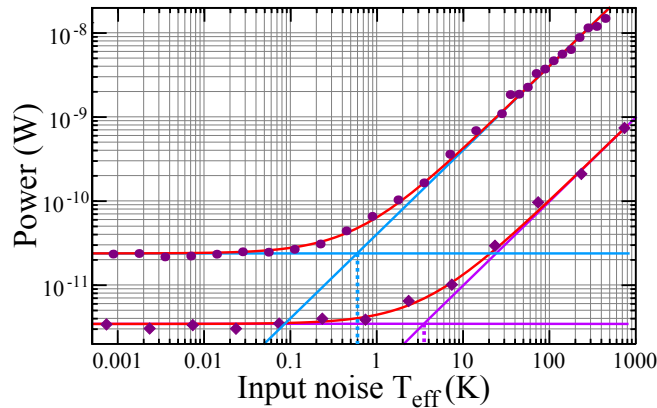


Figure 8.10: System noise power plotted as a function of T_{eff} without the MSA in the circuit (diamonds), and with the MSA in the circuit (circles).

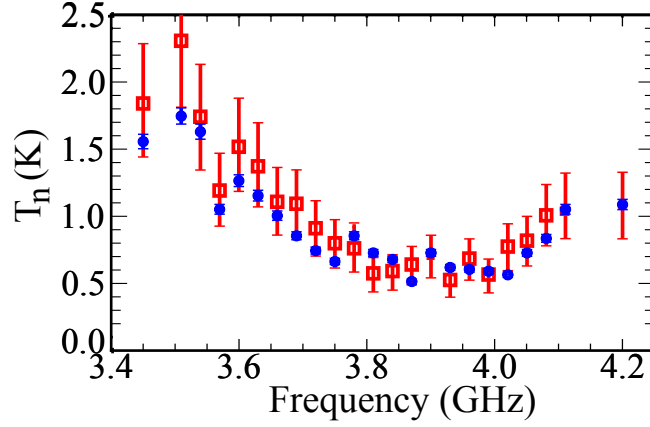


Figure 8.11: Noise temperature plotted as a function of frequency with the MSA in the measurement chain. The red open squares represent the noise temperature of the amplifier chain determined using the modified Y-factor technique. T_N measured using the SNR-ratio technique (Fig. 8.5) is also plotted (blue circles) for comparison.

temperature is expected to scale as $T_N^{opt} \propto (\omega_0/V_\Phi)T$. We studied the temperature dependence of the noise of our MSA at 3.85 GHz by varying the bath temperature over nearly a 200 mK range (Fig. 8.12). No significant variation of T_N was observed, suggesting that the electrons over this temperature range were not equilibrated to the bath temperature. This result conflicts with the expected variation of noise temperature with bath temperature, however we believe this conflict arises due to hot electrons in our shunt resistors. Although the MSA chip is thermalized with the bath, it is possible that electrons in the shunts are sitting at an elevated temperature.

8.5.3 Hot electrons

When sufficient power is dissipated in a thin resistive film at millikelvin temperatures, the electrons can be driven far out of equilibrium with the phonon bath [117]. For a resistor of volume Ω dissipating a power P , the temperature of the electrons is given by

$$T_e = \left(\frac{P}{\Sigma\Omega} + T_{ph}^5 \right)^{1/5} \quad (8.17)$$

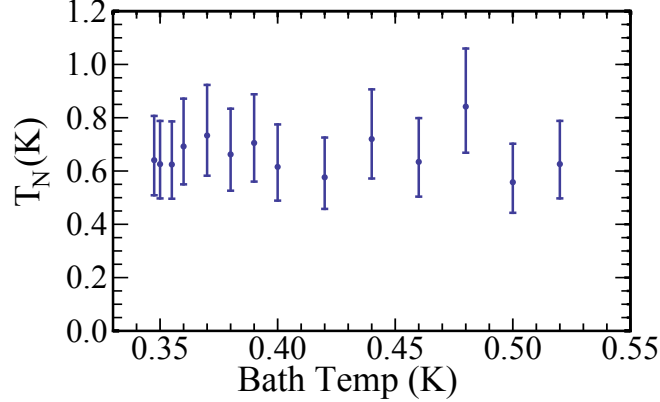


Figure 8.12: Noise temperature plotted as a function of cryostat bath temperature with the MSA in the measurement chain. Data was acquired using the modified Y-factor technique.

where $\Sigma = 1.2 \times 10^{-9} \text{ Wm}^{-3}\text{K}^{-5}$ is the electron-phonon coupling for Pd [122] and T_{ph} is the phonon temperature, taken to be the bath temperature $T_{ph} = 0.35 \text{ K}$. For a dissipated power of 1 nW, typical for the operating point of our SQUID amplifier, the electron temperature was calculated to be $T_e = 0.8 \text{ K}$ using Eqn. (8.17) and taking only the current-carrying volume of the shunt resistors into account. This estimation for the electron temperature in our shunt resistors, as well as the results of the temperature dependence of the system noise temperature, suggest that the electrons in our shunt resistors are not in equilibrium with the phonon bath. Thus, hot electrons in the shunts appear to be the dominant contribution to the system noise.

Equation (8.17) states that the electron temperature is inversely related to the volume of the shunt resistors, suggesting a route to reduce the temperature of the hot electrons, and hence the system noise temperature. Thin-film cooling fins with the same thickness as the shunt resistors ($\sim 20 \text{ nm}$) were integrated onto the device electrically connected to the end of the shunt resistors. The volume of the cooling fins was 30,000 times greater than the volume of the shunt resistors. The cooling fins provide a reservoir of cold electrons that thermalize hot electrons in the shunts. Recalculating the electron temperature for this much larger volume yields an electron

temperature $T_{e-fins} = 0.36$ K however a reduction in the system noise temperature was not measured.

There are two effects at work limiting the effectiveness of the cooling fins: the electron thermal relaxation length l_t [123], and the dimensionality of the phonon modes in the cooling fins [119]. The electron thermal relaxation length is given by

$$l_t = \sqrt{\frac{14\mathfrak{L}}{9\rho\Sigma T_R^3}} \quad (8.18)$$

where \mathfrak{L} is the Lorenz number taken to be $\mathfrak{L} = 2.45 \times 10^{-8}$ W Ω /K², ρ is the resistivity of the material, Σ is the electron-phonon coupling constant and T_R is the temperature of the resistor. The thermal relaxation length sets the scale on which hot electrons can exchange energy with the phonon bath, therefore any cooling fin structure that exceeds this length scale will not contribute to cooling hot electrons [119]. For parameters typical of our MSAs, the thermal relaxation length is estimated to be $l_t \approx 25\mu\text{m}$.

The effective volume of a cooling fin can also be estimated using the relation

$$\Omega_{CF} = \frac{3}{7}l_t A_{CF}. \quad (8.19)$$

For our 20 nm thick fins, $A_{CF} \approx 1 \mu\text{m}^2$ is the cross sectional area of the cooling fin, which gives an effective cooling fin volume of $\Omega_{CF} = 1 \mu\text{m}^3$. In light of this calculation, although our cooling fins are 30,000 times greater than the volume of our resistors, the effective volume of our cooling fin is $1 \mu\text{m}^3$, about 1/4 the volume of our $4.5 \mu\text{m}^3$ resistor. Recalculating our electron temperature Eqn. (8.17) with this additional volume yields a modest reduction in the estimated electron temperature, $T_e = 0.76\text{K}$.

Our cooling fins are deposited at the same time as our resistors, thus they have the same material properties and thickness. To achieve high resistivity films, which is desirable for our shunt resistors, the film must be thin, ~ 20 nm in the case of Pd. Although a thin film is desired for high resistivity, it enhances the temperature of

the electrons in the film because of the small effective volume of the cooling fin. In addition to this, the thickness of the film also reduces the dimension of the phonon bath [119]. The phonon wavelength can be calculated using

$$\lambda_{ph} = \frac{h\nu_s}{k_B T_{ph}} \quad (8.20)$$

where $\nu_s = 3070$ m/s is the speed of sound in palladium, and $T_{ph} = 0.35$ K is the temperature of the phonon bath, assumed to be the bath temperature of the cryostat. For a phonon bath temperature of 0.35 K, the phonon wavelength is $\lambda_{ph} \approx 0.4$ μm , which is much larger than the thickness of the film, therefore the hot electrons are only exchanging heat with a 2-dimensional phonon population. For effective cooling of the hot electrons, the cooling fins should have extents at least as large as λ_{ph} , the ideal geometry of a cooling fin will have extents at least as large as the electron thermal relaxation length, $l_t \approx 25$ μm as estimated for our shunt resistors.

Chapter 9

Application of near quantum-limited amplifiers in GHz range

The last several chapters have discussed our effort to increase the operating frequency of microstrip SQUID amplifier into the GHz frequency range with minimum added noise. In this final chapter we discuss one application of a near quantum-limited MSA, to perform time domain measurements of a non-linear oscillator. This device, the SQUID oscillator, is a bias dependent oscillator based on the plasma oscillations of a dc SQUID. A scheme to use this device to read out a flux qubit with an MSA as the first stage of amplification is discussed. Preliminary measurements of the SQUID oscillator using a HEMT amplifier indicate that this measurement scheme would benefit greatly from a near quantum limited amplifier such as our MSA.

9.1 The SQUID oscillator

Any dc SQUID has two modes of oscillation: an external mode, set by the capacitance of the junctions and couples to the bias current, and an internal mode, set by the

inductance and capacitance of the junction circuit, which couples to the bias flux [52]. The typical resonant frequency of these modes, which are determined by circuit parameters are large—on the order of 10's of GHz. By shunting the SQUID with a large parallel capacitance, the resonant frequency of the external mode is reduced to a range where plasma oscillations can be readout with an MSA. The SQUID oscillator

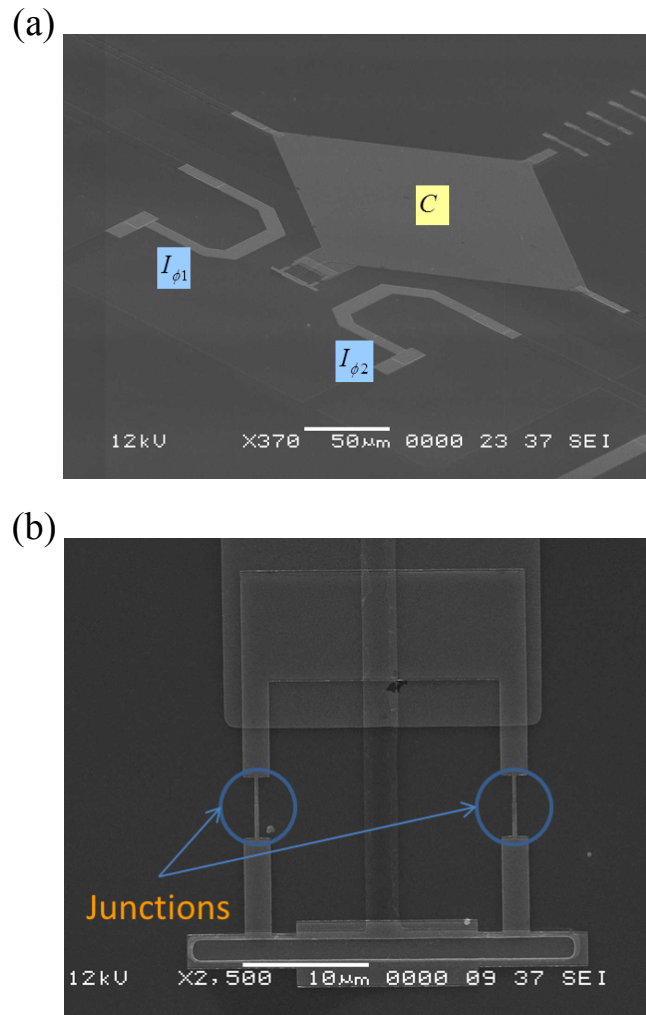


Figure 9.1: (a) Scanning electron micrograph of the SQUID oscillator with the parallel capacitor C and two flux bias lines $I_{\phi 1}$ and $I_{\phi 2}$ labeled. The SQUID loop is located at the bottom of the capacitor (diamond) between the two flux bias lines. (b) Scanning electron micrograph of the SQUID loop with the two junctions circled. The top of the SQUID connects to the top plate of the capacitor and the bottom of the SQUID loop connects, through a T-bar, to the bottom plate.

(Fig. 9.1) consists of an unshunted dc SQUID loop in parallel with a large parallel plate capacitor. The design was chosen to preserve the symmetry of the SQUID and also to minimize stray inductance. If the SQUID is considered to be a tunable inductance, then the combination of the SQUID in parallel with the capacitor forms a lumped element LC resonant circuit. A circuit consisting of a capacitor C in parallel with an inductor L will exhibit resonance behavior if driven at a frequency

$$\omega_0 = \frac{1}{\sqrt{LC}}. \quad (9.1)$$

If the inductor is replaced with a SQUID of inductance $L(I_b, \Phi_{ex})$, the resonance frequency of the oscillator $\omega_0 = 1/\sqrt{CL(\Phi_{ex}, I_b)}$ is now tunable with bias current I_b and bias flux Φ_{ex} . The expression for L_{SQ} in each of these cases is

$$L(\Phi_{ex} = 0, I_b) = \frac{\Phi_0}{4\pi I_0 \sqrt{1 - (\frac{I_b}{2I_0})^2}}, \quad (9.2)$$

and

$$L(\Phi_{ex}, I_b = 0) = \frac{\Phi_0}{4\pi I_0 \cos(\pi\Phi_{ex})}, \quad (9.3)$$

respectively, where I_0 is the critical current of one junction.

The dependence of the resonant frequency of this circuit on the state of the flux in the SQUID makes it a potentially useful tool for probing the state of a quantum bit (qubit) whose quantum mechanical degree of freedom is a flux. Such a readout scheme was proposed by Serban, Plourde and Wilhelm [124]. In this scheme, a flux qubit is inductively coupled to the SQUID loop. With the qubit prepared in a given flux state, a short bias current pulse is sent to the SQUID oscillator, coupling the qubit and oscillator for the duration of the pulse and imprinting the state of the qubit onto the oscillator. In the absence of a bias current pulse, the interaction between the SQUID and qubit is zero by symmetry. However, the bias current pulse breaks this symmetry, coupling the two systems for a brief duration. The state of the qubit can then be deduced by measuring the oscillations of the voltage across the SQUID in the time domain. The flux state of the qubit will impact the resonant dynamics of the

SQUID oscillator and the resulting difference in signal should be resolvable, allowing the state of the qubit to be inferred from this measurement of the SQUID oscillator (Fig. 9.2). Although the duration of the qubit-SQUID interaction is brief, it does not limit the measurement time. One has ample time, compared to the duration of the interaction, to readout the SQUID ringdown signal after the interaction has ceased without perturbing the state of the qubit.

A quantum nondeomition (QND) measurement is one which satisfies von Neumann's quantum measurement postulate [8, 125], projecting the system wave function onto an eigenstate of the observable. In the weak measurement regime, a QND measurement is achieved when the measured observable is a constant of free motion and commutes with the system-detector coupling Hamiltonian. In the proposed measurement, the system-detector interaction is arbitrarily strong but extremely short. Although the measured observable does not commute with the system-detector interaction Hamiltonian, it has been shown that this quasi-instantaneous measurement approximates a QND measurement [124] in the sense that it induces minimal decoherence of the state of the qubit. accordingly, it is deemed a quantum nondemolition-like measurement. The state of the qubit, however, is completely dephased as a result of the measurement. Although the original proposal employs a bias current pulse to toggle the qubit-SQUID coupling, for practical reasons it is more straightforward to excite the oscillator with a microwave burst. We expect this change in scheme preserves the QND-like behavior of the measurement.

The voltage oscillations measured across the SQUID oscillator are quite small in amplitude, therefore a good source of low noise amplification is necessary to perform the measurement. It was proposed to use an MSA as the first stage of amplification. In order to perform this type of measurement in a single shot (without averaging) an amplifier operating at the frequency of the oscillator with a 100 MHz bandwidth and a noise temperature of 200 mK is required [124]. We fabricated SQUID oscillators, appropriate for implementing this measurement scheme and characterized them in

both the frequency and time domain. Results will be discussed in detail in the following sections.

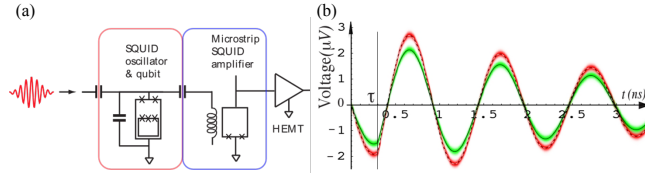


Figure 9.2: (a) A schematic of the circuit with a flux qubit inductively coupled to the SQUID oscillator. The MSA is used as a first stage of amplification of the SQUID oscillator circuit. A cryogenic HEMT amplifier is also used to further boost the signal. (b) Example voltage ringdown oscillations of the SQUID oscillator. Red and green traces correspond to different flux states of the qubit.

9.2 Measurement of SQUID oscillators

9.2.1 Frequency domain

Many of the experimental techniques used to study the SQUID oscillator are similar to those used to measure the MSA so they will not be discussed here in detail. The SQUID oscillator is capacitively coupled to a 50Ω feedline used to drive the device with a continuous microwave signal, or to ring-up the device with a microwave burst (Fig. 9.3). Devices were fabricated at the Cornell Nanoscale Science and Technology Facility and our own facilities at Syracuse University. The fabrication recipe is identical to the microstrip SQUID amplifiers as described in chapter 5 and devices can, in principle, be made side-by-side on the same wafer, or on separate wafers in the same fabrication run as we have done so far. Frequency domain measurements were conducted at a temperature of ~ 300 mK on our Janis ^3He refrigerator in a similar manner to measurements of the gain of our MSAs. The scattering parameter S_{21} of the device was measured using a network analyzer for several different bias current and bias flux points. The flux modulation of the resonance frequency is

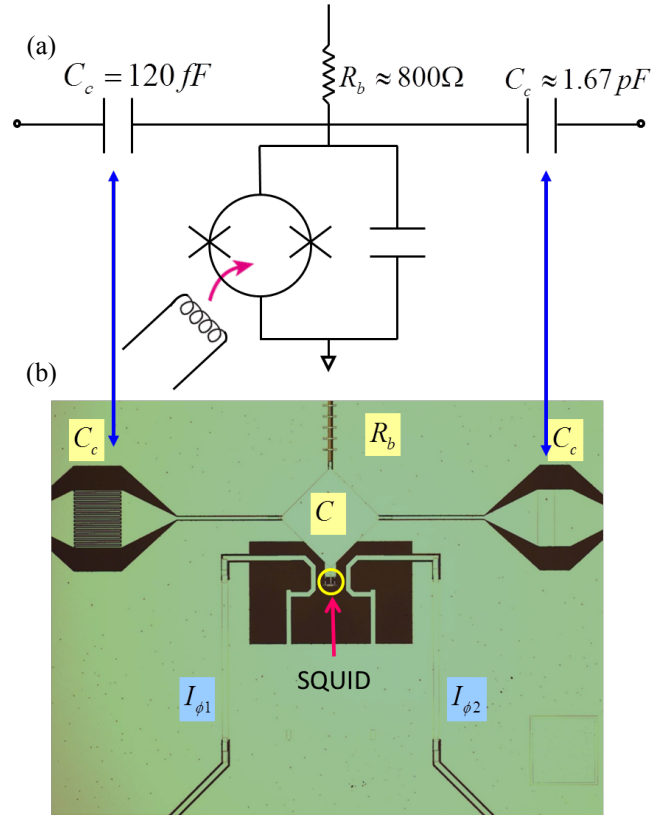


Figure 9.3: (a) Circuit schematic of the SQUID oscillator. (b) Optical micrograph of the SQUID oscillator illustrating the capacitors which couple the device to the feedline C_c , the parallel plate shunting capacitor $C = 10 \text{ pF}$, the SQUID loop (yellow circle) and the flux ($I_{\phi 1,2}$) and current bias line, R_b .

periodic in Φ_0 (Fig. 9.4). A bias current can also be used to modulate the resonance frequency down from its maximum value. The qubit measurement scheme requires time domain measurement of the freely evolving SQUID oscillator. In the next section, results of time domain measurements are reported for a SQUID oscillator in the absence of a qubit.

9.2.2 Transient dynamics

The transient dynamics of the SQUID oscillator were studied by sending short ~ 1 ns microwave pulses to the circuit through the drive line and measuring the voltage

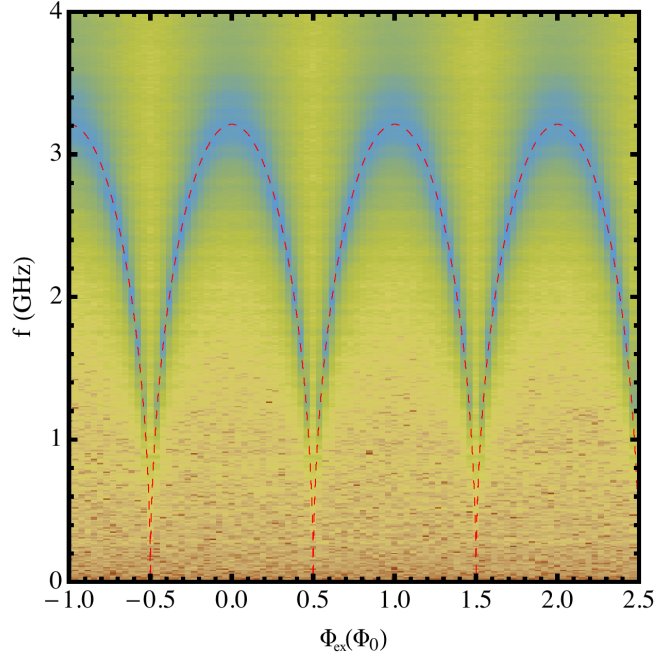


Figure 9.4: $|S_{21}|$ plotted as a function of frequency for several flux biases points. The red dashed-line indicates a fit to the data using the SQUID critical current $2I_0 = 0.76 \mu\text{A}$, capacitance $C = 10 \text{ pF}$ and stray inductance $L_{stray} = 29 \text{ pH}$ as fit parameters.

oscillations across the SQUID in the time domain. We were interested in studying both the ring up phase, where the phase particle is driven by the microwave burst, and the ringdown phase, where the phase particle is freely evolving. Pulses were generated using custom fast GHz digital-to-analog converter (DAC) hardware to gate a continuous microwave signal near the resonant frequency of the oscillator. Time domain measurement of the voltage oscillations of the SQUID were amplified with a cryogenic HEMT amplifier and a HEMT amplifier at room temperature. Substantial amplification is required to detect the small signal at the output of the SQUID oscillator, estimated to be $\sim 1 \mu\text{V}$. Since this signal is very small compared to the 5 K noise of the cryogenic HEMT amplifier over 4,000 averages were accumulated to achieve even a modest signal to noise ratio. Although the two HEMTs provide gain in excess of 70 dB, this particular measurement would benefit greatly from a microstrip SQUID amplifier due to its lower noise temperature. A schematic of the

measurement process is depicted in (Fig. 9.5).

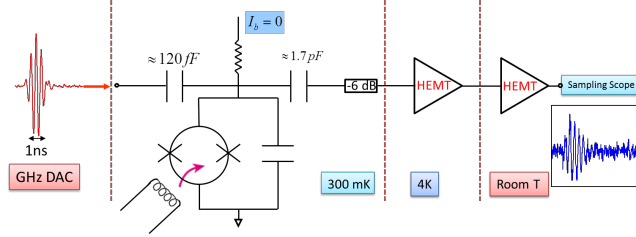


Figure 9.5: Schematic of the ringdown measurement setup.

To understand the dynamics of the oscillator, it is useful to consider the phase particle in the SQUID potential [52], as discussed previously in chapter 2. The phase particle is a fictitious object that resides in the SQUID potential (Eqn. 2.28). The position of the particle (x, y) corresponds to the sum $(x = (\delta_1 + \delta_2)/2)$ and difference $(y = (\delta_1 - \delta_2)/2)$ of the phases across the SQUID junctions. In this coordinate basis, the x coordinate couples to the bias current, and y couples to the bias flux, hence the shape of the SQUID potential can be altered by changing the value of the bias current and flux. For static bias points, and for bias current $I_b < I_0$, the phase particle will reside at a local potential minimum and undergo plasma oscillations at frequency

$$\omega_p = \frac{1}{\sqrt{L_J C_J}} = \sqrt{\frac{2eI_0}{\hbar C_J}}. \quad (9.4)$$

For an un-shunted SQUID with parameters similar to our SQUID oscillator, this plasma frequency will be in the range of ~ 100 's of GHz. However, the large capacitance in parallel with our SQUID reduces the plasma frequency to ~ 3 GHz. A static current or flux bias will cause the potential to tilt along the x - axis or shift the potential across the y - axis respectively. Exciting the oscillator by sending a resonant microwave signal into the drive line rocks the SQUID potential back and forth along the x - axis. As the potential is undergoing driven oscillations the phase particle will track the oscillations of the potential. When the microwave burst terminates, the phase particle will continue oscillating about the potential minimum due to its own momentum losing energy in each cycle until the amplitude of the oscillations decay.

To produce the microwave burst, a continuous microwave tone was generated and gated with a fast GHz DAC which, after filtering, produces a Gaussian envelope. The burst was sent to the feed line of the device down a highly attenuated coaxial cable and coupled to the SQUID oscillator through a coupling capacitor. The response of the SQUID was amplified by a cryogenic HEMT amplifier at 4 K and a room temperature HEMT. The amplified signal was detected using a Tektronix 11801c sampling oscilloscope with a minimum time resolution of 1 ps, which was triggered off of the same clock signal as the GHz DAC. The measurement sequence was repeated at a repetition rate of 7 kHz and the average of 4096 traces were recorded to enhance the signal-to-noise ratio. Figure 9.6(a) shows an example of a pulse sent into the cryostat used to ringup the oscillator. The response of the SQUID is shown in Fig. 9.6(b). During the first $\sim 2/3$ ns of the response signal, the SQUID oscillator is being driven by the microwave pulse. The ringdown signal after $\sim 2/3$ ns represents the free evolution of the SQUID oscillator.

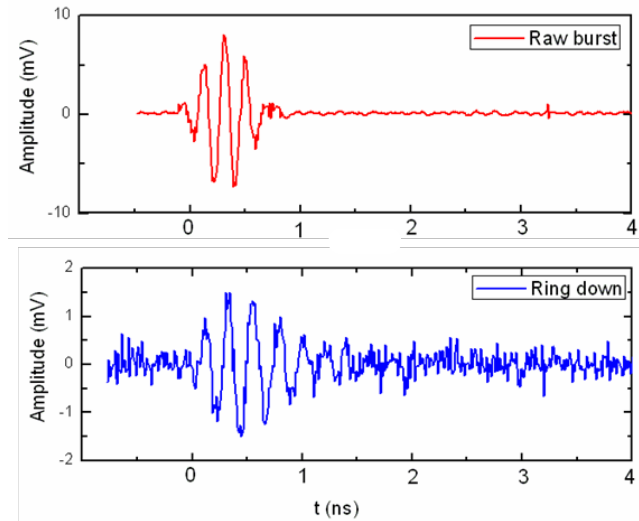


Figure 9.6: (a) Time traces of the raw burst used to ring up the SQUID oscillator. (b) Time trace of the ringdown voltage oscillations of the SQUID oscillator.

For a given pulse frequency and amplitude, the system response was measured as a function of bias flux Φ_{ex} (Fig. 9.7). The frequency of the microwave burst was set

to the maximum resonant frequency of the SQUID oscillator and the amplitude of the pulse was chosen such that it would not cause the SQUID to stochastically hop into a neighboring well in the potential. As the flux bias was increased, the plasma frequency of the SQUID oscillator, hence, the ringdown frequency was reduced. In addition to this, the resonant frequency of the SQUID oscillator became more detuned from the burst frequency. Hence, the oscillator was only driven on resonance for a flux bias near integer Φ_0 . These conditions are consistent with the observed response of the SQUID oscillator: the ‘fanning out’ of the ringdown signal in the density plot and the decrease of the signal amplitude in the vicinity of $\Phi_{ex} \approx \Phi_0/2$ [Fig. 9.7(b)].

There has been extensive work done on the unusual dynamics of continuously driven nonlinear oscillators [83, 126]. However, there is no work to date—either theoretically or experimentally—studying the transient dynamics of a pulsed nonlinear oscillator in the time domain, therefore this work is of both practical and fundamental importance. We are currently working with a theorist, Frank Wilhelm, to develop a model for this system and better understand its dynamics. Prof. Wilhelm and his research group are performing numerical simulations and the preliminary results are in good agreement with the measured behavior of this device. A manuscript is currently in preparation describing our experimental measurements of the SQUID oscillator ringdown and the numerical investigations of the transient dynamics of a pulsed nonlinear oscillator.

Once the SQUID oscillator is fully characterized in the time domain, a flux qubit will be incorporated into the circuit and the dependence of the oscillator on the qubit state will be studied. In addition, we plan to use a microstrip SQUID amplifier as the first stage of amplification for the SQUID oscillator circuit.

In a preliminary experiment, we measured a SQUID oscillator using an MSA as the first stage of amplification. We performed measurements of S_{21} as a function of frequency at several flux bias points of the SQUID oscillator (Fig. 9.8). The measurement was configured such that the SQUID oscillator and the MSA could be

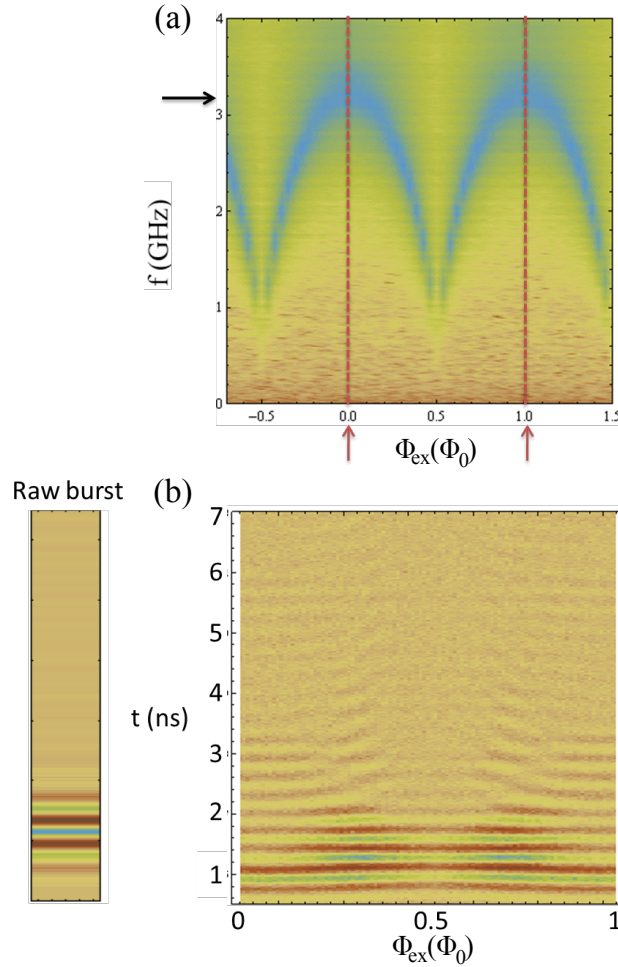


Figure 9.7: (a) S_{21} as a function of frequency plotted for several values of bias flux Φ_{ex} . Red arrows indicate the values of flux over which the ring down oscillations were measured. (b) Density plot of ringdown oscillations over range of bias flux values indicated by arrows in (a). A single vertical slice of the density plot is one ringdown oscillation measurement.

measured independently to ensure the MSA was biased for maximum gain. With the MSA optimally biased, we observed the frequency domain response of the SQUID oscillator. The measurement scheme, however, suffered from impedance mismatches in the circuit, causing large periodic standing waves to appear in the S_{21} measurements. In a future measurement, we intend to reduce the contribution of the the standing-waves by matching the impedance of elements in the circuit using cryogenic attenuators. Despite the standing-waves, this proof-of-principle measurement is con-

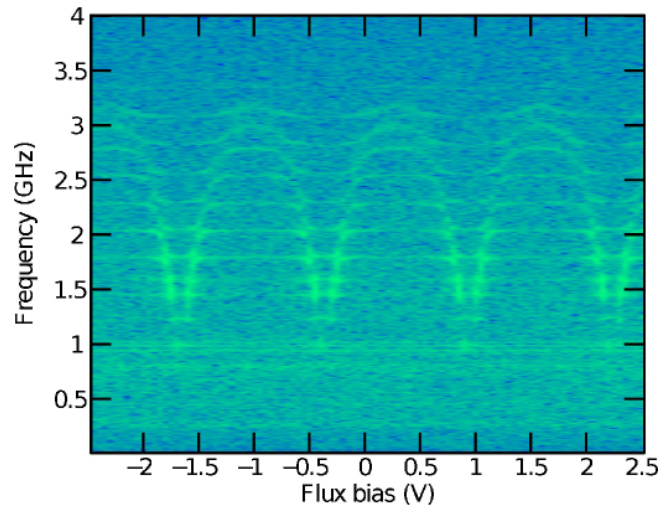


Figure 9.8: $|S_{21}|$ plotted as a function of frequency for several flux biases points using an MSA as the first stage of amplification. This measurement scheme suffered from impedance mismatches resulting in unintended standing waves resonances.

sidered a success in the regard that an MSA has been demonstrated as the first stage of amplification of a SQUID oscillator.

Chapter 10

Future work

10.1 Introduction

Microstrip SQUID amplifiers have great potential in the field of quantum information science. We have demonstrated a device operating in the 4 GHz range with sufficient bandwidth, and noise substantially lower than state-of-the-art HEMT amplifiers. Microstrip SQUID amplifiers pose many advantages when compared with other cryogenic low-noise amplifiers due to their gain, bandwidth and noise properties. Furthermore, there is a clear path to improving these devices.

10.2 Three-dimensional cooling fins

In light of the results presented at the end of chapter 8, evidence suggests that the noise performance of our SQUID amplifiers is limited by hot electrons in the resistive shunts of the SQUID. A scheme to reduce the temperature of these non-equilibrium electrons is in development. The results from chapter 8 suggest that using a cooling fin with dimensions that exceed the phonon wavelength, and that are on the scale of the electron thermal relaxation length, should provide more effective cooling of hot electrons.

Until recently, the thickness of our cooling fins has been limited to the thickness of our shunt resistors, ~ 20 nm. Working with collaborators at University of Wisconsin, Madison, we have developed a technique to produce metallic cooling fins that are of the order of $10 \mu\text{m}$ thick. To provide a sense of scale, that is $500 \times$ thicker than our shunt resistors. If our shunt resistors were the height of a 6 ft. tall person, the cooling fins would be as tall as the Burj Dubai, the tallest man-made free-standing structure in the world. The technique to fabricate a film with this aspect ratio is by no means trivial, nonetheless we developed such a technique and implemented cooling fins on devices. To form the cooling fins, copper was electroplated onto a palladium seed layer that was in electrical contact with the shunt resistors. The 3D cooling fins allow hot electrons to efficiently exchange heat with a 3-dimensional phonon population, providing more efficient cooling. Although the thickness of these cooling fins does not exceed the electron thermal relaxation length in all three dimensions, the extents in the x and y directions do. Referring back to the discussion at the end of chapter 8, according to Eq. (8.17), the estimated electron temperature for our resistors using a cooling fin of this geometry is $T_e = 0.36$ K, approximately the bath temperature. We expect that integrating these cooling fins into our MSA should result in substantially reduced system noise temperature.

Once 3D cooling fins have been demonstrated and the noise properties of the SQUID amplifier are no longer limited by hot electrons, devices can be measured at lower bath temperatures on either our dilution refrigerator ($T_p \approx 0.03\text{K}$) or our adiabatic demagnetization refrigerator ($T_p \approx 0.05\text{K}$). Since the SQUID noise is dominated by Johnson-Nyquist noise which scales with temperature, we expect lower system noise temperature at reduced bath temperatures. However, until the electron temperature becomes comparable to the temperature of the cryostat, reducing the bath temperature is not expected to result in a reduction of the system noise temperature. Even at arbitrarily low bath temperatures, the contribution of hot electrons will still dominate. A calculation of the electron temperature for a negligible bath

temperature shows that for the present 3D cooling fin geometry the electron temperature is limited to a minimum value of 0.21 K. At this point, redesigning the cooling fins with larger volumes could result in a lower electron temperature.

Preliminary measurements of the electron temperature in resistors cooled with 3D cooling fins, that we fabricated, were performed by collaborators at University of Wisconsin, Madison. Thin film Pd resistors were patterned on an oxidized Si wafer and 10 μm thick copper cooling fins were deposited on top of a portion of the resistors (Fig. 10.1). Using a chain of two dc SQUIDs configured to perform a current measurement, the temperature of the electrons in the resistors was measured using noise spectroscopy.

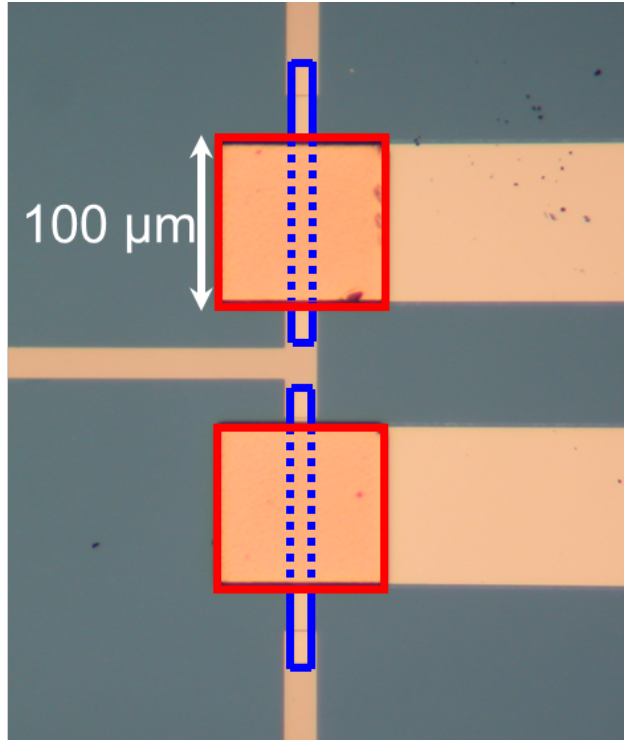


Figure 10.1: (a) Optical micrograph of the Pd resistors (blue outline) and Cu cooling fins (red outline) measured at U.W. Madison.

Results of the noise spectroscopy in figure 10.2 show a reduction in electron temperature of roughly a factor of 3 as compared to the model for electron temperature

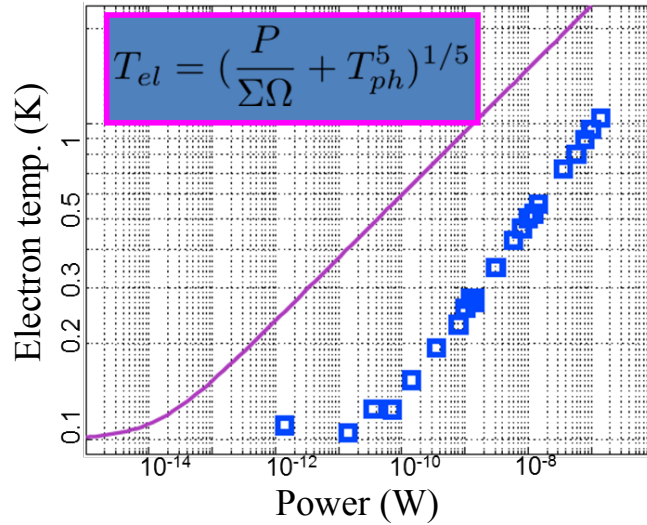


Figure 10.2: Electron temperature plotted vs dissipated power. Measured values for the structure in 10.1 plotted as open blue squares. For comparison, the expression for the electron temperature, equation 8.17, is plotted as a function of dissipated power (purple line).

for ~ 1 nW of dissipated power. These preliminary results provide encouraging evidence that incorporating 3D cooling fins in our MSA design will reduce the electron temperature in the shunts and reduce the noise temperature of our MSAs. We have fabricated a wafer of MSAs configured to incorporate 3D cooling fins and we are looking forward to performing noise measurements on these devices (Fig. 10.3).

10.3 Higher frequencies

In order to make MSAs practical for applications in quantum information science, the operating frequency must be increased further. We have demonstrated an amplifier that provides 17 dB of gain with a 150 MHz band and 0.5 K noise temperature that operates at near 4 GHz.

Although our amplifier at 4 GHz is suitable for some applications, such as amplifying the signal of our SQUID oscillator, recent superconducting qubit are coupled to cavities with frequencies between 6 GHz and 12 GHz. Therefore, the operating

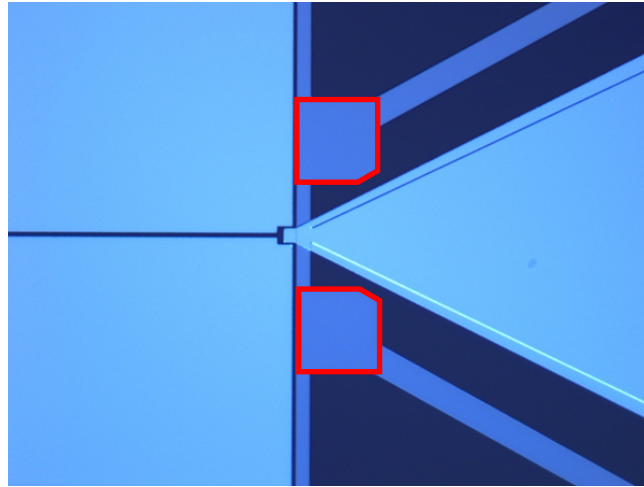


Figure 10.3: Optical micrograph of an MSA with a Pd seed layer on which 3D Cu cooling fins will be plated. Cooling fins will occupy the areas outlined in red.

frequency of our MSAs must be increased while preserving the gain, bandwidth and noise characteristics. As discussed in earlier chapters, the operating frequency of an MSA is determined by the length of its input coil. The shorter coils required for higher operating frequency have less mutual inductance, thus the device will have less gain for a given V_Φ . The most immediate hurdle is producing an amplifier that operates at high frequency, while preserving gain.

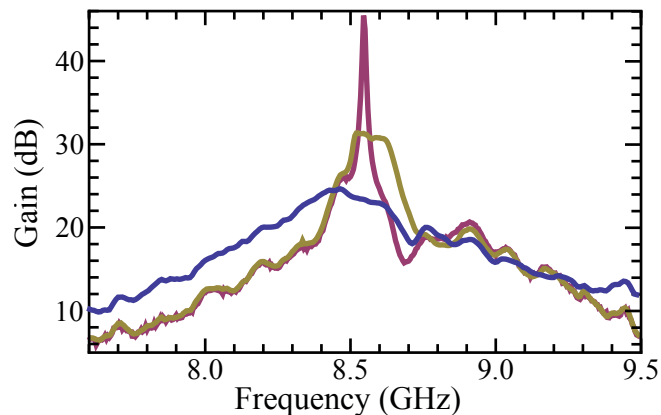


Figure 10.4: Gain vs. frequency for an MSA operating near 9 GHz. The three curves correspond to three different bias points

We have produced a microstrip SQUID amplifier that operates near 9 GHz with

20 dB of gain. The gain of this MSA was particularly bias dependent and under certain bias conditions exhibited gain in excess of 40 dB (Fig. 10.4). Although this MSA exhibited substantial gain, its noise properties made it impractical to use as an amplifier. In a preliminary measurement, the system noise temperature was measured to be in the vicinity of 5 K, similar to the noise temperature of our HEMT amplifier.

Although the device has substantial gain, its presence in the amplifier chain will degrade the signal-to-noise ratio as compared with the HEMT alone. The high gain of this device in combination with its high noise temperature leads us to believe it may be well power matched and poorly noise matched. Although this preliminary result is encouraging, the device must be further optimized for low-noise performance.

Appendix A

Fabrication recipes

Recipes for fabricating microstrip SQUID amplifier and SQUID oscillators.

A.1 Photolithography

A.1.1 Mask preparation

Step 1: Obtain a photomask appropriate for the stepper. Make sure the resist layer is free of defects. Remove dust from resist layer with dry nitrogen.

Step 2: Place mask in DWL2000.

Step 3: Expose mask with desired pattern.

Step 4: Develop mask in Hamatech automatic developer: Recipe 2.

Step 5: Etch chrome in Hamatech automatic developer: Recipe 1.

A.1.2 Wafer preparation

Step 1: Clean spin bowl with acetone.

Step 2: Place wafer on appropriate spin chuck and center the wafer.

Step 3: Dispense 1/2 pipette of UV210-0.6 resist into spin bowl but not on wafer.

Step 4: Spin wafer at 3000 rpm for 45 s to condition the spin bowl.

Step 5: Once conditioning is complete dispense a quarter-sized amount of DSK101-312 ARC onto wafer and spin for 45 s at 3000 rpm.

Step 6: Remove wafer from bowl and remove resist edge bead from back side of wafer with a swab and acetone.

Step 7: Bake on proximity hot plate at 185° C for 90 s.

Step 8: Place wafer in spin bowl and dispense UV210-0.6 onto wafer.

Step 7: Spin wafer at 3000 rpm for 45 s.

Step 9: Remove wafer from bowl and remove resist edge bead from back side of wafer with a swab and acetone.

Step 10: Bake on proximity hotplate at 135° for 60 s.

A.1.3 Exposure

Step 1: Load mask and wafer(s) into ASML-300c deep-UV stepper.

Step 2: Set exposure energy density to $25\mu\text{J}/\text{cm}^2$ and focus to $-0.2\ \mu\text{m}$.

Step 3: Expose wafer(s).

Step 4: Post-exposure-bake wafers on proximity hotplate at 135° C for 90 s.

Step 5: Develop in Hamatech automatic waver developer MIF 726 for 120 s double puddle.

Step 6: Examine pattern to determine if additional development is necessary.

Step 7: Descum wafer in the Glen 1000 in RIE mode with 150 W for 30s. Examine wafer.

A.2 Metalization — Shunts

Step 1: Load wafers into a liftoff chuck. Load a Ti source and a Pd source in a crucible into the evaporator hearth.

Step 2: Check crystal growth monitor. If greater than 5% used, replace.

Step 3: Make sure shutter is in ‘closed’ position.

Step 4: Evacuate chamber until pressure is $< 5 \times 10^{-6}$ Torr.

Step 5: Evaporate 1.5 nm of Ti at $\sim 1 \text{ \AA/s}$.

Step 6: Evaporate 20 nm of Pd at $\sim 2 \text{ \AA/s}$.

Step 7: Allow 5 minutes for source to cool before venting.

Step 8: Remove wafers and sources from the evaporator.

Step 9: Prepare a heated bath of remover 1165 at 80° C agitated with a spin bar.

Step 10: Perform liftoff in heated 1165 bath for ~ 1 hour, or until the wafer is free of the resist/metal layer.

Step 11: Remove DSK in Hamatech auto developer. MIF 726 for 120 s, double puddle.

Step 12: Remove remaining DSK in Glen 1000 for 180 s at 250 W. Examine wafer.

Step 13: Run a spin-rinse-dry cycle in SRD system.

A.3 Groundplane deposition

Step 1: Pattern the groundplane layer photolithographically with steps above.

Step 2: Descum resist layer.

Step 3: Return to Syracuse to perform deposition in dedicated Al evaporator.

Step 4: Load wafers into evaporator and pump until base pressure is $< 10^{-7}$ Torr.

Step 5: Deposit 80 nm of Al at a rate of 8-15 Å/s.

Step 6: Lift off in a covered acetone bath heated to 75° C.

Step 7: Once resist/metal layer is mostly removed, sonicate for 5 seconds.

Step 8: Remove wafer from bath and drench with isopropanol and immediately blow dry with dry nitrogen.

Step 9: Return to CNF and remove remaining DSK in the Glen 1000 at 250 W for 180 seconds.

Step 10: Run a spin-rinse-dry cycle in the SRD.

A.4 Dielectric deposition — GSI-PECVD

Step 1: Select undoped Oxide n=1.46 recipe.

Step 2: Change run time to 45 s.

Step 3: Change process temperature to 200° C.

Step 4: Load in dummy wafer and run an 'etch-autoclean' recipe for 10 min.

Step 5: Process one wafer at a time with a clean step in between.

Step 6: After wafers have been processed run a final 'etch-autoclean' recipe for 10 min.

Step 7: Measure film thickness on the Leitz interferometer (accounting for the 90 nm of thermal oxide).

A.5 Dielectric deposition — IPE-PECVD

Step 1: Inspect chamber, make sure it is free of particulates. Manually clean if necessary and replace shower head.

Step 2: Run ‘chamber clean’ recipe for 15 min at a temperature of 150° C.

Step 3: Once hotplate reaches process temperature place at most 3 wafers onto the hotplate.

Step 4: Select recipe ‘SiO₂ A’ and change process temperature to 150° C and process time to 3.4 minutes.

Step 5: Begin process.

Step 6: Once deposition is complete remove wafers from chamber and perform a manual cleaning of the chamber.

Step 7: Replace shower head.

Step 8: Clean used shower head.

Step 9: Run ‘chamber clean’ for ten minutes plus the process time.

Step 10: Repeat steps to perform photolithography to pattern oxide layer.

A.6 Etching

Step 1: Clean Oxford 80 by running process ‘Chamber Clean’ for 10 min.

Step 2: Load no more than 3 wafers into the chamber.

Step 3: Run recipe ‘CF₄etch’ for 4 min.

Step 4: Check etched film thickness on the Leitz interferometer. If not all of the PECVD SiO₂ has been etched, repeat etch step for another 1 minute.

Step 5: If desired amount of SiO₂ has been etched, remove wafers from chamber.

Step 6: Run ‘Chamber Clean’ recipe for 10 minutes plus process time.

Step 7: Strip wafers in heated 1165 bath as described above. DO NOT REMOVE DSK WITH BASIC DEVELOPER—THIS WILL RUIN WAFERS.

Step 8: Remove remaining DSK in Glen 1000 at 250 W for 180 s.

Step 9: Inspect wafers.

A.7 Input coil

Step 1: Pattern the input coil layer photolithographically with steps above.

Step 2: Desum resist mask in the Glen 1000.

Step 3: Return to Syracuse and deposit Al as described above.

Step 4: Strip wafers in acetone as described above.

Step 5: Return to CNF and remove remaining DSK in the Glen 1000 at 250 W for 180 seconds.

A.8 Electron beam lithography

Step 1: Run a spin-rinse-dry cycle on SRD tool.

Step 2: Load wafer into electron beam resist spin bowl and select a recipe that spins at 2500 rpm for 60 seconds.

Step 3: Spin wafer with bowl open and rinse with acetone and isopropanol simultaneously.

Step 4: Dispense 1 pipette of 11% MMA(8.5)MAA in ethyl lactate.

Step 5: Spin for 60 seconds at 2500 rpm.

Step 6: Bake for 10 minutes at 170° C.

Step 7: Return wafer to spin bowl and select recipe to spin at 3000 rpm for 60 seconds.

Step 8: Dispense 1 pipette of PMMA 950K 2.7% in anisol.

Step 9: Spin for 60 seconds at 3000 rpm.

Step 10: Bake at 170° C for 10 minutes.

Step 11: Load wafer into appropriate chuck.

Step 12: Perform prealignment in the prealignment scope, noting stage coordinates of P and Q mark.

Step 13: Load chuck in to JEOL 9300 and perform aligned exposure.

Step 14: After exposure, remove wafers from JEOL and return to Syracuse to perform junction deposition.

A.9 Junction deposition

Step 1: Dice wafer as desired.

Step 2: Develop exposed pattern in MIBK:IPA (1:3) for 60 seconds.

Step 3: Drench chip in IPA and blow dry with dry nitrogen gas.

Step 4: Load wafer into evaporator noting orientation of junctions.

Step 5: Evacuate chamber.

Step 6: Charge gas ballast to desired pressure (~ 7 Torr).

- Step 7: Clean sample with ion mill at 500 V accelerator voltage and 30 mA beam current for 10-12 seconds.
- Step 8: Orient chip at -11.5° with respect to the normal.
- Step 9: Deposit 35 nm of Al at a rate of 8-15 $\text{\AA}/\text{s}$.
- Step 10: Turn power down to 30 %.
- Step 11: Close gate valve between top and bottom chamber.
- Step 12: Open valve between gas ballast and top chamber, exposing the sample to Ar/O mixture.
- Step 13: Expose sample for 45-60 seconds.
- Step 14: Evacuate top chamber after oxidation with the roughing pump, then the turbo pump.
- Step 15: Open the gate valve between top and bottom chamber.
- Step 16: Deposit top junction layer at an angle of 11.5° with respect to the normal.
- Step 17: Vent chamber and remove sample.

Bibliography

- [1] M. C. Runyan, P. A. R. Ade, M. Amiri, S. Benton, R. Bihary, J. J. Bock, J. R. Bond, J. A. Bonetti, S. A. Bryan, H. C. Chiang, C. R. Contaldi, B. P. Crill, O. Dore, D. O’Dea, M. Farhang, J. P. Filippini, L. Fissel, N. Gandilo, S. R. Gollwala, J. E. Gudmundsson, M. Hasselfield, M. Halpern, G. Hilton, W. Holmes, V. V. Hristov, K. D. Irwin, W. C. Jones, C. L. Kuo, C. J. MacTavish, P. V. Mason, T. A. Morford, T. E. Montroy, C. B. Netterfield, A. S. Rahlin, C. D. Reintsema, J. E. Ruhl, M. A. Schenker, J. Shariff, J. D. Soler, A. Trangsrud, R. S. Tucker, C. E. Tucker, and A. Turner, “Design and performance of the SPIDER instrument,” in *Society of Photo-Optical Instrumentation Engineers (SPIE) Conference Series*, vol. 7741 of *Society of Photo-Optical Instrumentation Engineers (SPIE) Conference Series*, July 2010.
- [2] M. Hofheinz, E. M. Weig, M. Ansmann, R. C. Bialczak, E. Lucero, M. Neeley, A. D. O’Connell, H. Wang, J. M. Martinis, and A. N. Cleland, “Generation of Fock states in a superconducting quantum circuit,” *Nature*, vol. 454, pp. 310–314, July 2008.
- [3] A. Wallraff, D. I. Schuster, A. Blais, L. Frunzio, R.-S. Huang, J. Majer, S. Kumar, S. M. Girvin, and R. J. Schoelkopf, “Strong coupling of a single photon to a superconducting qubit using circuit quantum electrodynamics,” *Nature*, vol. 431, pp. 162–167, Sept. 2004.

- [4] S. J. Freedman and J. F. Clauser, “Experimental Test of Local Hidden-Variable Theories,” *Physical Review Letters*, vol. 28, pp. 938–941, Apr. 1972.
- [5] D. Boschi, S. Branca, F. de Martini, L. Hardy, and S. Popescu, “Experimental Realization of Teleporting an Unknown Pure Quantum State via Dual Classical and Einstein-Podolsky-Rosen Channels,” *Physical Review Letters*, vol. 80, pp. 1121–1125, Feb. 1998.
- [6] C. Monroe, D. M. Meekhof, B. E. King, W. M. Itano, and D. J. Wineland, “Demonstration of a fundamental quantum logic gate,” *Phys. Rev. Lett.*, vol. 75, pp. 4714–4717, Dec 1995.
- [7] S. Haroche and J.-M. Raimond, *Exploring the Quantum Atoms, Cavities and Photons*. Oxford, U.K.: Oxford University Press, 2006.
- [8] C. Cohen-Tannoudji, B. Diu, and F. Laloë, *Quantum Mechanics*. Weinheim: Wiley, 1992.
- [9] E. Jaynes and F. Cummings, “Comparison of quantum and semiclassical radiation theories with application to the beam maser,” *Proceedings of the IEEE*, vol. 51, pp. 89 – 109, jan. 1963.
- [10] C. Gerry and P. Knight, *Introductory Quantum Optics*. Cambridge, U.K.: Cambridge University Press, 2005.
- [11] D. Kielpinski, C. Monroe, and D. J. Wineland, “Architecture for a large-scale ion-trap quantum computer,” *Nature*, vol. 417, pp. 709–711, June 2002.
- [12] R. Raussendorf and H. J. Briegel, “A one-way quantum computer,” *Phys. Rev. Lett.*, vol. 86, pp. 5188–5191, May 2001.
- [13] L. Childress, J. M. Taylor, A. S. Sørensen, and M. D. Lukin, “Fault-tolerant quantum communication based on solid-state photon emitters,” *Phys. Rev. Lett.*, vol. 96, p. 070504, Feb 2006.

- [14] B. E. Cole, J. B. Williams, B. T. King, M. S. Sherwin, and C. R. Stanley, “Coherent manipulation of semiconductor quantum bits with terahertz radiation,” *Nature*, vol. 410, pp. 60–63, Mar. 2001.
- [15] B. E. Kane, “A silicon-based nuclear spin quantum computer,” *Nature*, vol. 393, pp. 133–137, May 1998.
- [16] J. Clarke and F. K. Wilhelm, “Superconducting quantum bits,” *Nature*, vol. 453, pp. 1031–1042, June 2008.
- [17] Y. Kubo, C. Grezes, A. Dewes, T. Umeda, J. Isoya, H. Sumiya, N. Morishita, H. Abe, S. Onoda, T. Ohshima, V. Jacques, A. Dréau, J.-F. Roch, I. Diniz, A. Auffeves, D. Vion, D. Esteve, and P. Bertet, “Hybrid quantum circuit with a superconducting qubit coupled to a spin ensemble,” *Phys. Rev. Lett.*, vol. 107, p. 220501, Nov 2011.
- [18] D. van Delft, “Little cup of helium, big science,” *Physics Today*, vol. 61, no. 3, p. 030000, 2008.
- [19] H. Onnes, “The resistance of pure mercury at helium temperatures,” *Comm. Leiden*, April 1911.
- [20] W. Meissner and R. Ochsenfeld, “Ein neuer effekt bei eintritt der supraleitfähigkeit,” *Naturwissenschaften*, vol. 21, pp. 787–788, 1933. 10.1007/BF01504252.
- [21] F. London and H. London, “The electromagnetic equations of the supraconductor,” *Proceedings of the Royal Society of London. Series A, Mathematical and Physical Sciences*, vol. 149, no. 866, pp. pp. 71–88, 1935.
- [22] V. Ginzburg and L. Landau *Zh. Eksp. Teor. Fiz.*, vol. 20, p. 1064, 1950.
- [23] J. Bardeen, L. N. Cooper, and J. R. Schrieffer, “Theory of Superconductivity,” *Physical Review*, vol. 108, pp. 1175–1204, Dec. 1957.

- [24] B. D. Josephson, “Possible new effects in superconductive tunnelling,” *Physics Letters*, vol. 1, pp. 251–253, July 1962.
- [25] P. W. Anderson and J. M. Rowell, “Probable Observation of the Josephson Superconducting Tunneling Effect,” *Physical Review Letters*, vol. 10, Issue 6, pp. 230–232, vol. 10, pp. 230–232, Mar. 1963.
- [26] M. H. Devoret, A. Wallraff, and J. M. Martinis, “Superconducting Qubits: A Short Review,” *eprint arXiv:cond-mat/0411174*, Nov. 2004.
- [27] M. Büttiker, “Zero-current persistent potential drop across small-capacitance Josephson junctions,” *Physical Review B*, vol. 36, pp. 3548–3555, Sept. 1987.
- [28] V. Bouchiat, D. Vion, P. Joyez, D. Esteve, and M. H. Devoret, “Quantum coherence with a single cooper pair,” *Physica Scripta*, vol. 1998, no. T76, p. 165, 1998.
- [29] Y. Nakamura, Y. A. Pashkin, and J. S. Tsai, “Coherent control of macroscopic quantum states in a single-Cooper-pair box,” *Nature*, vol. 398, pp. 786–788, Apr. 1999.
- [30] C. H. van der Wal, A. C. J. ter Haar, F. K. Wilhelm, R. N. Schouten, C. J. P. M. Harmans, T. P. Orlando, S. Lloyd, and J. E. Mooij, “Quantum Superposition of Macroscopic Persistent-Current States,” *Science*, vol. 290, pp. 773–777, Oct. 2000.
- [31] J. M. Martinis, S. Nam, J. Aumentado, and C. Urbina, “Rabi Oscillations in a Large Josephson-Junction Qubit,” *Physical Review Letters*, vol. 89, p. 117901, Aug. 2002.
- [32] D. Vion, A. Aassime, A. Cottet, P. Joyez, H. Pothier, C. Urbina, D. Esteve, and M. H. Devoret, “Manipulating the Quantum State of an Electrical Circuit,” *Science*, vol. 296, pp. 886–889, May 2002.

- [33] J. Koch, T. M. Yu, J. Gambetta, A. A. Houck, D. I. Schuster, J. Majer, A. Blais, M. H. Devoret, S. M. Girvin, and R. J. Schoelkopf, “Charge-insensitive qubit design derived from the Cooper pair box,” *Physical Review A*, vol. 76, p. 042319, Oct. 2007.
- [34] H. Paik, D. I. Schuster, L. S. Bishop, G. Kirchmair, G. Catelani, A. P. Sears, B. R. Johnson, M. J. Reagor, L. Frunzio, L. I. Glazman, S. M. Girvin, M. H. Devoret, and R. J. Schoelkopf, “Observation of high coherence in josephson junction qubits measured in a three-dimensional circuit qed architecture,” *Phys. Rev. Lett.*, vol. 107, p. 240501, Dec 2011.
- [35] C. Rigetti, S. Poletto, J. M. Gambetta, B. L. T. Plourde, J. M. Chow, A. D. Corcoles, J. A. Smolin, S. T. Merkel, J. R. Rozen, G. A. Keefe, M. B. Rothwell, M. B. Ketchen, and M. Steffen, “Superconducting qubit in waveguide cavity with coherence time approaching 0.1ms,” *ArXiv e-prints*, Feb. 2012.
- [36] M. Hofheinz, H. Wang, M. Ansmann, R. C. Bialczak, E. Lucero, M. Neeley, A. D. O’Connell, D. Sank, J. Wenner, J. M. Martinis, and A. N. Cleland, “Synthesizing arbitrary quantum states in a superconducting resonator,” *Nature*, vol. 459, pp. 546–549, May 2009.
- [37] T. Yamamoto, M. Neeley, E. Lucero, R. C. Bialczak, J. Kelly, M. Lenander, M. Mariantoni, A. D. O’Connell, D. Sank, H. Wang, M. Weides, J. Wenner, Y. Yin, A. N. Cleland, and J. M. Martinis, “Quantum process tomography of two-qubit controlled-z and controlled-not gates using superconducting phase qubits,” *Phys. Rev. B*, vol. 82, p. 184515, Nov 2010.
- [38] R. Vijay, C. Macklin, D. H. Slichter, S. J. Weber, K. W. Murch, R. Naik, A. N. Korotkov, and I. Siddiqi, “Quantum feedback control of a superconducting qubit: Persistent Rabi oscillations,” *ArXiv e-prints*, May 2012.

- [39] C. M. Caves, “Quantum limits on noise in linear amplifiers,” *Physical Review D*, vol. 26, pp. 1817–1839, Oct. 1982.
- [40] L. N. Cooper, “Bound Electron Pairs in a Degenerate Fermi Gas,” *Physical Review*, vol. 104, pp. 1189–1190, Nov. 1956.
- [41] M. Tinkham, *Introduction to Superconductivity, Second Edition*. New York, USA: McGraw-Hill, Inc., 1996.
- [42] V. M. Agranovich and A. Maradudin, *Mesoscopic Phenomena in Solids*. Amsterdam: North-Holland, 1991.
- [43] T. Van Duzer and C. Turner, *Principles of Superconductive Devices and Circuits*. Upper Saddle River, NJ, USA: Prentice Hall PTR, 1999.
- [44] P. G. de Gennes, “Boundary Effects in Superconductors,” *Reviews of Modern Physics*, vol. 36, pp. 225–237, Jan. 1964.
- [45] J. Seto and T. van Duzer, “Supercurrent Tunneling Junctions with Tellurium Barriers,” *Applied Physics Letters*, vol. 19, pp. 488–491, Dec. 1971.
- [46] D. Dimos, P. Chaudhari, J. Mannhart, and F. K. LeGoues, “Orientation dependence of grain-boundary critical currents in $\text{Yb}_2\text{Cu}_3\text{O}_{7-\delta}$ bicrystals,” *Phys. Rev. Lett.*, vol. 61, pp. 219–222, Jul 1988.
- [47] K. K. Likharev, “Superconducting weak links,” *Rev. Mod. Phys.*, vol. 51, pp. 101–159, Jan 1979.
- [48] Y. Soutome and Y. Okabe, “Magnetic field modulation of critical currents in ybacuo co-planar josephson junctions using focused ion beam,” *Applied Superconductivity, IEEE Transactions on*, vol. 7, pp. 2311–2314, jun 1997.
- [49] J. Clarke and A. Braginski, *The SQUID Handbook Vol. 1*. Weinheim, Germany: Wiley-VCH, 2004.

- [50] W. C. Stewart, “Current-Voltage Characteristics of Josephson Junctions,” *Applied Physics Letters*, vol. 12, pp. 277–280, Apr. 1968.
- [51] D. E. McCumber, “Effect of ac Impedance on dc Voltage-Current Characteristics of Superconductor Weak-Link Junctions,” *Journal of Applied Physics*, Vol. 39, p.3113-3118, vol. 39, pp. 3113–3118, June 1968.
- [52] V. Lefevre-Seguin, E. Turlot, C. Urbina, D. Esteve, and M. H. Devoret, “Thermal activation of a hysteretic dc superconducting quantum interference device from its different zero-voltage states,” *Physical Review B*, vol. 46, pp. 5507–5522, Sept. 1992.
- [53] J. M. Lockhart, “SQUID readout and ultra-low magnetic fields for Gravity Probe-B (GP-B),” in *Society of Photo-Optical Instrumentation Engineers (SPIE) Conference Series* (R. K. Melugin, ed.), vol. 619 of *Society of Photo-Optical Instrumentation Engineers (SPIE) Conference Series*, pp. 148–156, Jan. 1986.
- [54] D. Cohen, “Magnetoencephalography: Detection of the brain’s electrical activity with a superconducting magnetometer,” *Science*, vol. 175, no. 4022, pp. 664–666, 1972. Cited By (since 1996): 122.
- [55] S. Comani, S. Conforto, D. Di Nuzzo, M. Basile, S. Di Luzio, S. N. Ern, and G. L. Romani, “Non-invasive detection of gastric myoelectrical activity: Comparison between results of magnetogastrography and electrogastrography in normal subjects,” *Physica Medica*, vol. 12, no. 1, pp. 25–32, 1996. Cited By (since 1996): 3.
- [56] C. Hilbert and J. Clarke, “DC SQUIDS as radiofrequency amplifiers,” *Journal of Low Temperature Physics*, vol. 61, pp. 263–280, Nov. 1985.
- [57] J. M. Martinis and J. Clarke, “Signal and noise theory for a dc SQUID amplifier,” *Journal of Low Temperature Physics*, vol. 61, pp. 227–236, Nov. 1985.

- [58] C. Hilbert and J. Clarke, "Measurements of the dynamic input impedance of a dc SQUID," *Journal of Low Temperature Physics*, vol. 61, pp. 237–262, Nov. 1985.
- [59] E. Ben-Jacob, E. Mottola, and G. Schoen, "Quantum shot noise in tunnel junctions," *Physical Review Letters*, vol. 51, pp. 2064–2067, Nov. 1983.
- [60] Y. M. Ivanchenko and L. A. Zil'berman, "Destruction of Josephson Current by Fluctuations," *Soviet Journal of Experimental and Theoretical Physics Letters*, vol. 8, p. 113, Aug. 1968.
- [61] P. Dutta and P. M. Horn, "Low-frequency fluctuations in solids: 1f noise," *Reviews of Modern Physics*, vol. 53, pp. 497–516, July 1981.
- [62] C. D. Tesche and J. Clarke, "dc SQUID: Noise and optimization," *Journal of Low Temperature Physics*, vol. 29, pp. 301–331, Nov. 1977.
- [63] C. T. Rogers and R. A. Buhrman, "Composition of 1f Noise in Metal-Insulator-Metal Tunnel Junctions," *Physical Review Letters*, vol. 53, pp. 1272–1275, Sept. 1984.
- [64] S. Sendelbach, D. Hover, M. Mück, and R. McDermott, "Complex Inductance, Excess Noise, and Surface Magnetism in dc SQUIDS," *Physical Review Letters*, vol. 103, p. 117001, Sept. 2009.
- [65] P. Horowitz and W. Hill, *The Art of Electronics*. Cambridge, United Kingdom: Cambridge University Press, 1989.
- [66] C. D. Tesche and J. Clarket, "dc SQUID: Current noise," *Journal of Low Temperature Physics*, vol. 37, pp. 397–403, Nov. 1979.
- [67] R. H. Koch, D. J. van Harlingen, and J. Clarke, "Quantum noise theory for the dc SQUID," *Applied Physics Letters*, vol. 38, pp. 380–382, Mar. 1981.

- [68] W. Weitschies, R. Ktitz, L. Trahms, and D. Cordini, “Gastrointestinal transit of a magnetically marked capsule monitored using a 37-channel squid-magnetometer,” *Journal De Physique.IV : JP*, vol. 7, no. 1, pp. C1–667–C1–668, 1997.
- [69] J. P. Wikswo Jr. and J. P. Barach, “Possible sources of new information in the magnetocardiogram,” *Journal of theoretical biology*, vol. 95, no. 4, pp. 721–729, 1982. Cited By (since 1996): 33.
- [70] K. Schlenga, R. McDermott, J. Clarke, R. E. de Souza, A. Wong-Foy, and A. Pines, “Low-field magnetic resonance imaging with a high- T_c dc superconducting quantum interference device,” *Applied Physics Letters*, vol. 75, p. 3695, Dec. 1999.
- [71] S. Gaffet, Y. Guglielmi, J. Virieux, G. Waysand, A. Chwala, R. Stolz, C. Emblanch, M. Auguste, D. Boyer, and A. Cavaillou, “Simultaneous seismic and magnetic measurements in the low-noise underground laboratory (lsbb) of rustrel, france, during the 2001 january 26 indian earthquake,” *Geophysical Journal International*, vol. 155, no. 3, pp. 981–990, 2003. Cited By (since 1996): 17.
- [72] R. Kleiner, D. Koelle, F. Ludwig, and J. Clarke, “Superconducting quantum interference devices: State of the art and applications,” *Proceedings of the IEEE*, vol. 92, pp. 1534 – 1548, oct. 2004.
- [73] M. Mck, “Squids: Microscopes and nondestructive evaluation,” in *Physica Status Solidi C: Conferences*, vol. 2, pp. 1510–1523, 2005. Cited By (since 1996): 1.
- [74] M. Muck, C. Welzel, A. Farr, F. Schloz, and W. Singer, “Nondestructive testing of niobium sheets for superconducting resonators,” *Applied Superconductivity, IEEE Transactions on*, vol. 13, pp. 239 – 244, june 2003.

- [75] B. L. Plourde, D. J. van Harlingen, N. Saha, R. Besseling, M. B. Hesselberth, and P. H. Kes, “Vortex distributions near surface steps observed by scanning SQUID microscopy,” *Physical Review B*, vol. 66, p. 054529, Aug. 2002.
- [76] C. Hilbert and J. Clarke, “Radio-frequency amplified based on a dc superconducting quantum interference device,” *Applied Physics Letters*, vol. 43, pp. 694–696, Oct. 1983.
- [77] M. Pospieszalski, S. Weinreb, R. Norrod, and R. Harris, “Fets and hemts at cryogenic temperatures-their properties and use in low-noise amplifiers,” *Microwave Theory and Techniques, IEEE Transactions on*, vol. 36, pp. 552–560, march 1988.
- [78] S. Weinreb, M. W. Pospieszalski, and R. Norrod, “Cryogenic, HEMT, Low-Noise Receivers for 1.3 to 43 GHz Range,” in *IEEE MTT-S International Microwave Symposium Digest, 2, 945-948*, pp. 945–948, 1988.
- [79] M. A. Castellanos-Beltran, K. D. Irwin, G. C. Hilton, L. R. Vale, and K. W. Lehnert, “Amplification and squeezing of quantum noise with a tunable Josephson metamaterial,” *Nature Physics*, vol. 4, pp. 929–931, Dec. 2008.
- [80] M. Castellanos-Beltran, K. Irwin, L. Vale, G. Hilton, and K. Lehnert, “Bandwidth and dynamic range of a widely tunable josephson parametric amplifier,” *Applied Superconductivity, IEEE Transactions on*, vol. 19, pp. 944–947, june 2009.
- [81] B. H. Eom, P. K. Day, H. G. Leduc, and J. Zmuidzinas, “A Wideband, Low-Noise Superconducting Amplifier with High Dynamic Range,” *ArXiv e-prints*, Jan. 2012.
- [82] N. Roch, E. Flurin, F. Nguyen, P. Morfin, P. Campagne-Ibarcq, M. H. Devoret, and B. Huard, “Widely Tunable, Nondegenerate Three-Wave Mixing Microwave

- Device Operating near the Quantum Limit,” *Physical Review Letters*, vol. 108, p. 147701, Apr. 2012.
- [83] R. Vijay, M. H. Devoret, and I. Siddiqi, “Invited Review Article: The Josephson bifurcation amplifier,” *Review of Scientific Instruments*, vol. 80, p. 111101, Nov. 2009.
- [84] G. J. Ribeill, D. Hover, Y.-F. Chen, S. Zhu, and R. McDermott, “Superconducting low-inductance undulatory galvanometer microwave amplifier: Theory,” *Journal of Applied Physics*, vol. 110, p. 103901, Nov. 2011.
- [85] D. Hover, Y.-F. Chen, G. J. Ribeill, S. Zhu, S. Sendelbach, and R. McDermott, “Superconducting low-inductance undulatory galvanometer microwave amplifier,” *Applied Physics Letters*, vol. 100, p. 063503, Feb. 2012.
- [86] M. Mück, M.-O. André, J. Clarke, J. Gail, and C. Heiden, “Radio-frequency amplifier based on a niobium dc superconducting quantum interference device with microstrip input coupling,” *Applied Physics Letters*, vol. 72, p. 2885, June 1998.
- [87] M. Tarasov, V. Belitsky, and G. Prokopenko, “Dc squid rf amplifiers,” *Applied Superconductivity, IEEE Transactions on*, vol. 2, pp. 79–83, jun 1992.
- [88] M. Tarasov, G. Prokopenko, V. Koshelets, I. Lapitskaya, and L. Filippenko, “Integrated rf amplifier based on dc squid,” *Applied Superconductivity, IEEE Transactions on*, vol. 5, pp. 3226–3229, jun 1995.
- [89] G. Prokopenko, S. Shitov, V. Koshelets, D. Balashov, and J. Mygind, “A dc squid based low-noise 4 ghz amplifier,” *Applied Superconductivity, IEEE Transactions on*, vol. 7, pp. 3496–3499, jun 1997.
- [90] A. D. Hibbs, M. A. Krupka, L. R. Kunstmanas, D. K. Lathrop, C. Say,

- W. Zheng, and M. S. DiIorio, "New amplifier configuration based on the circulating current state of a dc squid," *Physica C*, vol. 368, pp. 146–152, 2002.
- [91] M. Mück and R. McDermott, "TOPICAL REVIEW: Radio-frequency amplifiers based on dc SQUIDS," *Superconductor Science Technology*, vol. 23, p. 093001, Sept. 2010.
- [92] L. Spietz, K. Irwin, and J. Aumentado, "Superconducting quantum interference device amplifiers with over 27 GHz of gain-bandwidth product operated in the 4-8 GHz frequency range," *Applied Physics Letters*, vol. 95, p. 092505, Aug. 2009.
- [93] T. H. Lee, *Planar Microwave Engineering*. Cambridge, United Kingdom: Cambridge University Press, 2004.
- [94] K. Gupta, R. Garg, I. Bahl, and P. Bhartia, *Microstrip Lines and Striplines*. Boston, London: Artech House, Inc., 1996.
- [95] D. M. Pozar, *Microwave Engineering*. Hoboken, NJ: John Wiley and Sons, Inc., 2005.
- [96] D. Kinion and J. Clarke, "Microstrip superconducting quantum interference device radio-frequency amplifier: Scattering parameters and input coupling," *Applied Physics Letters*, vol. 92, p. 172503, Apr. 2008.
- [97] M. Mück, C. Welzel, and J. Clarke, "Superconducting quantum interference device amplifiers at gigahertz frequencies," *Applied Physics Letters*, vol. 82, p. 3266, May 2003.
- [98] T. Takami, T. Noguchi, and K. Hamanaka, "A dc squid amplifier with a novel tuning circuit," *Magnetics, IEEE Transactions on*, vol. 25, pp. 1030–1033, mar 1989.

- [99] G. Prokopenko, D. Balashov, S. Shitov, V. Koshelets, and J. Mygind, “Two-stage s-band dc squid amplifier,” *Applied Superconductivity, IEEE Transactions on*, vol. 9, pp. 2902–2905, jun 1999.
- [100] M.-O. André, M. Mück, J. Clarke, J. Gail, and C. Heiden, “Radio-frequency amplifier with tenth-kelvin noise temperature based on a microstrip direct current superconducting quantum interference device,” *Applied Physics Letters*, vol. 75, p. 698, Aug. 1999.
- [101] M. Mück, J. B. Kycia, and J. Clarke, “Superconducting quantum interference device as a near-quantum-limited amplifier at 0.5 GHz,” *Applied Physics Letters*, vol. 78, p. 967, Feb. 2001.
- [102] D. Kinion and J. Clarke, “Superconducting quantum interference device as a near-quantum-limited amplifier for the axion dark-matter experiment,” *APPLIED PHYSICS LETTERS*, vol. 98, MAY 16 2011.
- [103] M. Mück, D. Hover, S. Sendelbach, and R. McDermott, “Microstrip superconducting quantum interference device radio-frequency amplifier: Effects of negative feedback on input impedance,” *Applied Physics Letters*, vol. 94, p. 132509, Mar. 2009.
- [104] M. Mück and J. Clarke, “The superconducting quantum interference device microstrip amplifier: Computer models,” *Journal of Applied Physics*, vol. 88, pp. 6910–6918, Dec. 2000.
- [105] D. Kinion and J. Clarke, “Microstrip superconducting quantum interference device amplifier: Conditional stability,” *Applied Physics Letters*, vol. 96, p. 172501, Apr. 2010.
- [106] M. Mück, M.-O. André, J. Clarke, J. Gail, and C. Heiden, “Microstrip superconducting quantum interference device radio-frequency amplifier: Tuning and cascading,” *Applied Physics Letters*, vol. 75, p. 3545, Nov. 1999.

- [107] S. Wolf and R. Tauber, *Silicon Processing for the VLSI Era, Volume 1*. Lattice Press, Sunset Beach, CA: Cambridge University Press, 1986.
- [108] G. J. Dolan, "Offset masks for lift-off photoprocessing," *Applied Physics Letters*, vol. 31, p. 337, Sept. 1977.
- [109] M. P. Defeo, P. Bhupathi, K. Yu, T. W. Heitmann, C. Song, R. McDermott, and B. L. T. Plourde, "Microstrip superconducting quantum interference device amplifiers with submicron Josephson junctions: Enhanced gain at gigahertz frequencies," *Applied Physics Letters*, vol. 97, p. 092507, Aug. 2010.
- [110] W. Mallison, R. Miller, and A. Kleinsasser, "Effect of growth conditions on the electrical properties of nb/al-oxide/nb tunnel junctions," *IEEE Transactions on Applied Superconductivity*, vol. 5, no. 2 pt 3, pp. 2330–2333, 1995. cited By (since 1996) 5.
- [111] M. Gurvitch, M. A. Washington, and H. A. Huggins, "High quality refractory Josephson tunnel junctions utilizing thin aluminum layers," *Applied Physics Letters*, vol. 42, pp. 472–474, Mar. 1983.
- [112] R. Dolata, H. Scherer, A. B. Zorin, and J. Niemeyer, "Single-charge devices with ultrasmall Nb/AlO_x/Nb trilayer Josephson junctions," *Journal of Applied Physics*, vol. 97, p. 054501, Mar. 2005.
- [113] V. Ambegaokar and A. Baratoff, "Tunneling Between Superconductors," *Physical Review Letters*, vol. 10, pp. 486–489, June 1963.
- [114] J. M. Martinis, M. H. Devoret, and J. Clarke, "Experimental tests for the quantum behavior of a macroscopic degree of freedom: The phase difference across a Josephson junction," *Physical Review B*, vol. 35, pp. 4682–4698, Apr. 1987.

- [115] F. Pobell, *Matter and Methods at Low Temperatures*. Berlin, Germany: Springer, 1996.
- [116] M. B. Ketchen and J. M. Jaycox, “Ultra-low-noise tunnel junction dc SQUID with a tightly coupled planar input coil,” *Applied Physics Letters*, vol. 40, pp. 736–738, Apr. 1982.
- [117] F. C. Wellstood, C. Urbina, and J. Clarke, “Hot-electron effects in metals,” *Physical Review B*, vol. 49, pp. 5942–5955, Mar. 1994.
- [118] F. C. Wellstood, C. Urbina, and J. Clarke, “Hot-electron limitation to the sensitivity of the dc superconducting quantum interference device,” *Applied Physics Letters*, vol. 54, pp. 2599–2601, June 1989.
- [119] J. Pleikies, O. Usenko, R. Stolz, L. Fritsch, G. Frossati, and J. Flokstra, “Hot-electron effect in PdAu thin-film resistors with attached cooling fins,” *Superconductor Science Technology*, vol. 22, p. 114007, Nov. 2009.
- [120] M. B. Ketchen, K. G. Stawiasz, D. J. Pearson, T. A. Brunner, C.-K. Hu, M. A. Jaso, M. P. Manny, A. A. Parsons, and K. J. Stein, “Sub-micron linewidth input coils for low T_c integrated thin-film dc superconducting quantum interference devices,” *Applied Physics Letters*, vol. 61, pp. 336–338, July 1992.
- [121] J. Clarke, C. D. Tesche, and R. P. Giffard, “Optimization of dc SQUID voltmeter and magnetometer circuits,” *Journal of Low Temperature Physics*, vol. 37, pp. 405–420, Nov. 1979.
- [122] A. Vinante, P. Falferi, R. Mezzena, and M. Mück, “Hot-electron effect in palladium thin films,” *Physical Review B*, vol. 75, p. 104303, Mar. 2007.
- [123] P. M. Echternach, M. R. Thoman, C. M. Gould, and H. M. Bozler, “Electron-phonon scattering rates in disordered metallic films below 1 K,” *Physical Review B*, vol. 46, pp. 10339–10344, Oct. 1992.

- [124] I. Serban, B. L. T. Plourde, and F. K. Wilhelm, “Quantum nondemolition-like fast measurement scheme for a superconducting qubit,” *Physical Review B*, vol. 78, p. 054507, Aug. 2008.
- [125] J. von Neumann, *Mathematical Foundations of Quantum Mechanics*. Princeton, NJ: Princeton University Press, 1955.
- [126] M. Dykman and M. Krivoglaz, “Fluctuations in nonlinear systems near bifurcations corresponding to the appearance of new stable states,” *Physica A: Statistical Mechanics and its Applications*, vol. 104, no. 3, pp. 480 – 494, 1980.

VITA

NAME OF AUTHOR: Michael P. DeFeo

PLACE OF BIRTH: Mount Kisco, New York

DATE OF BIRTH: February 8, 1983

GRADUATE AND UNDERGRADUATE SCHOOLS ATTENDED:

Syracuse University, Syracuse, New York (2005-2012)

Syracuse University, Syracuse, New York (2001-2005)

DEGREES AWARDED:

Syracuse University

Bachelor of Science in Engineering Physics, 2005

PROFESSIONAL EXPERIENCE:

Undergraduate Research Assistant, Syracuse University, 2002-2005

Teaching Assistant, Syracuse University, 2005-2008

Research Assistant, Syracuse University, 2005-Present